Event-by-event fluctuations of mean transverse momentum, $\langle p_{\mathrm{T}} \rangle$, in pp, Xe–Xe and Pb–Pb collisions with ALICE at the LHC

A Thesis
Submitted in partial fulfillment of
the requirements for the degree of
Doctor of Philosophy
by

Tulika Tripathy
(Roll No. 174120008)

Supervisor:
Prof. Sadhana Dash

Department of Physics
Indian Institute of Technology Bombay
Mumbai 400076 (India)

29 February 2024

Dedicated To My Family, Friends And Teachers

Acceptance Certificate

Department of Physics

Indian Institute of Technology, Bombay

The thesis entitled "Event-by-event fluctuations of mean transverse momentum, $\langle p_T \rangle$, in pp, Xe–Xe and Pb–Pb collisions with ALICE at the LHC" submitted by Tulika Tripathy (Roll No. 174120008) may be accepted for being evaluated.

Sadhana Dash

Date: 29 February 2024

Prof. Sadhana Dash

Approval Sheet

This thesis entitled "Event-by-event fluctuations of mean transverse momentum, $\langle p_T \rangle$, in pp, Xe-Xe and Pb-Pb collisions with ALICE at the LHC" by Tulika Tripathy is approved for the degree of Doctor of Philosophy.

P. K. Behera

Examiners

Supervisor (s)

Chairman

Date: 29/02/2024

Place: Department of Physics, IIT Bombay

Declaration

I declare that this written submission represents my ideas in my own words and where others' ideas or words have been included, I have adequately cited and referenced the original sources. I declare that I have properly and accurately acknowledged all sources used in the production of this report. I also declare that I have adhered to all principles of academic honesty and integrity and have not misrepresented or fabricated or falsified any idea/data/fact/source in my submission. I understand that any violation of the above will be a cause for disciplinary action by the Institute and can also evoke penal action from the sources which have thus not been properly cited or from whom proper permission has not been taken when needed.

Tulika Tripathy

Tulika Tripathy

(Roll No. 174120008)

Date: 29 February 2024

Abstract

In heavy-ion collisions, event-by-event measurements play a crucial role in understanding the high-energy nuclear interaction dynamics and the quark-gluon plasma (QGP) properties. Studies of event-by-event fluctuations of observables measured in heavy-ion collisions are of great interest given they probe the phase transition from QGP to hadron gas (HG). Of particular interest are event-by-event fluctuations of the average transverse momentum ($\langle p_{\mathrm{T}} \rangle$) of charged particles measured in a specific kinematic range. These fluctuations are expected to be sensitive to energy fluctuations, and arguably, temperature variations of the produced matter in these collisions. Fluctuations in the average transverse momentum act as a proxy to the fluctuation in the temperature of the system. The temperature fluctuations are predicted to sharply increase in the vicinity of the critical point and in this part of the QCD phase diagram, a rapid change in the heat capacity of the medium near the phase transition is expected. $\langle p_{\mathrm{T}} \rangle$ fluctuations are also highly sensitive to the presence of collective effects and the onset of thermalization in mesoscopic systems. Measurements of $\langle p_{\mathrm{T}} \rangle$ fluctuations are thus an essential tool to achieve a better understanding of the hot and dense matter produced in heavy-ion collisions. To measure the non-statistical average p_{T} fluctuations, the analysis is carried out using the two-particle transverse-momentum correlator, $\sqrt{\langle \Delta p_{\mathrm{T},1} \Delta p_{\mathrm{T},2} \rangle} / \langle \langle p_{\mathrm{T}} \rangle \rangle$. This observable is designed to nullify scenarios exhibiting purely statistical fluctuations. Any non-zero signal detected signifies particle correlations in momentum space, contributing to dynamic average p_{T}.

This thesis comprises the analysis of the event-by-event mean transverse-momentum fluctuations in proton–proton (pp), xenon-xenon (Xe–Xe), and lead–lead (Pb–Pb) collisions in the centre-of-mass energies of 5.02 TeV for pp and Pb-Pb collisions and 5.44 TeV for Xe-Xe collisions. The analysis is performed for charged particles with transverse momenta in the range

of 0.15 GeV/c < p_{T} < 2 GeV/c. The chosen pseudorapidity acceptance of $|\eta| < 0.8$ plays a crucial role in ensuring uniform acceptance and efficient track detection within the ALICE Time Projection Chamber, a key detector of this study.

The data analysis in this investigation is divided into two main components. Initially, the analysis focuses on studying event-by-event fluctuations in the average transverse momentum, $\langle p_{\mathrm{T}} \rangle$, of charged particles produced in Pb–Pb, Xe–Xe, and pp collisions. In this part, the study reports a system and energy scan of event-by-event $\langle p_{\mathrm{T}} \rangle$ fluctuations as a function of the charged particle pseudorapidity density. The observed $\sqrt{\langle \Delta p_{\mathrm{T},1} \Delta p_{\mathrm{T},2} \rangle}/\langle\langle p_{\mathrm{T}} \rangle\rangle$ exhibits a non-vanishing strength and demonstrated an approximate power-law dependence on the produced charged particle density. These findings validate and support previous observations of non-Poissonian fluctuations in AA collisions. In the system size scan, the magnitude of the correlator is observed to decrease by more than one order of magnitude with respect to the produced particle multiplicity density measured in pp, Xe–Xe, and Pb–Pb collisions as the multiplicity increases from low to high values. The measured evolution of the two-particle correlator with $\langle \mathrm{dN_{ch}}/\mathrm{d}\eta \rangle$ for Pb–Pb and Xe–Xe collisions is compared with calculations based on the HIJING and AMPT model using the default mode and the mode with string melting. The magnitude of the two-particle correlator computed with HIJING exhibits a simple power law behavior. This power law dependence and exponent value are consistent with the behaviour expected for a system consisting of a simple superposition of nucleon-nucleon collisions without re-scattering of the secondaries as modelled by HIJING. However, one observes that while the evolution of the correlator measured in both Pb–Pb and Xe–Xe approximately follows the HIJING power-law fit in the range $10 < \langle \mathrm{d}N_{\mathrm{ch}}/\mathrm{d}\eta \rangle < 50$, it clearly deviates from this simple trend at $\langle \mathrm{d}N_{\mathrm{ch}}/\mathrm{d}\eta \rangle > 50$. This indicates that the final state particle production in Xe–Xe and Pb–Pb collisions cannot be described by a mere superposition of independent particle-emitting sources. The observed deviation is likely a result of radial flow, yet exploring the potential for increased correlations stemming from fluctuations linked to jet production is an intriguing factor. The aim is to discern whether fluctuations in the number of jets compared to the "baseline" regime (those devoid of jets) might amplify fluctuations, potentially influencing the magnitude of the correlator.

This curiosity led to explore how the strength of the correlator varies in pp collisions, ranging from jet-like to isotropic events, constituting the second part of the analysis. Hence, the evolution of $\sqrt{\langle \Delta p_{\mathrm{T},1} \Delta p_{\mathrm{T},2} \rangle} / \langle \langle p_{\mathrm{T}} \rangle \rangle$ with $\langle \mathrm{d}N_{\mathrm{ch}}/\mathrm{d}\eta \rangle$ in pp collisions at $\sqrt{s}$ = 5.02 TeV for different spherocity classes is studied in this thesis. Events characterized by the presence of jets exhibits more significant mean transverse momentum fluctuations compared to isotropic events. In high-multiplicity collisions, the presence of jets increases the correlator's strength by around 20%. This enhancement primarily stems from particles emitted within a "narrow" cone by jets, showing a higher average correlation among themselves compared to other particles. Consequently, the existence of jets notably increases the correlator's strength within these events.

Observing an increase in the correlator strength for events with jet-like characteristics relative to spherocity-integrated pp collisions suggests that the outcomes witnessed in A–A collisions might not be solely due to jet suppression. Hence, the presence of jets in central A–A collisions isn't expected to significantly contribute to the strength of the correlator.

Table of Contents

List of Figures

Chapter 1

Introduction

The vastness of space and time within the Universe has always held a profound fascination for humanity. As inherently curious beings, humans possess a natural inclination to seek about our surroundings, including fundamental questions about our existence. This curiosity often leads to explore the origin of the Universe. Scientists often grapple with a series of fundamental inquiries about the Universe: How expansive is it? What path does it traverse? How did our Universe come into being? What governs its behaviour today, and what lies ahead in its future? These inquiries have opened up exciting new avenues of research and technological advancements, enabling us to probe not only the farthest reaches of the cosmos but also the behaviour of matter and energy at the quark level.

The birth of a miniature Universe is simulated within a laboratory setting by recreating conditions by establishing what one might aptly term a "mini big bang". Scientists are currently endeavouring to piece together the sequence of events that gave rise to our Universe in its earliest moments. Such efforts hold the promise of enhancing our understanding of the universe and offer solutions to some of the most pressing contemporary questions.

1.1 The expanding Universe and the Big Bang

One of the most significant discoveries in the realm of science is the observation of the expanding universe by Edwin Hubble [1]. While observing far-off galaxies in the early 1920s,

Edwin Hubble, discovered that the lights from those galaxies had a redshift. The wavelength of the light is stretched while an object is moving away from the viewer. It shifts towards the red portion of the spectrum, thus the name "redshift". This phenomenon is called Doppler shift 1.1.

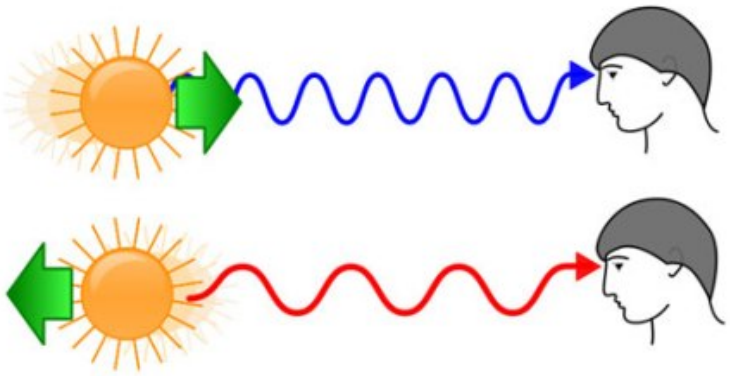

Figure 1.1: Doppler effect in light

The Doppler shift for an observer moving away from the source is given by:

$$\lambda' = \lambda \sqrt{\frac{1 + v/c}{1 - v/c}} \tag{1.1}$$

where λ' → Observed wavelength by the observer

λ → Source wavelength

c → Speed of the light

v → Velocity of the observer

From the above equation, one can see that $\lambda' > \lambda$, which shows that the wavelength is stretched, towards the red part of the visible spectrum. This implies that the galaxies are moving away from Earth, i.e. the universe is expanding. Therefore, if one travels through time, the universe must have been at a point with an infinite energy density, which is when one assumes the Big Bang happened.

Hubble's Law is depicted in Figure 1.2, showing a linear correlation between a galaxy's velocity (v) and its distance (d) given by:

$$v = H_0 \times d \tag{1.2}$$

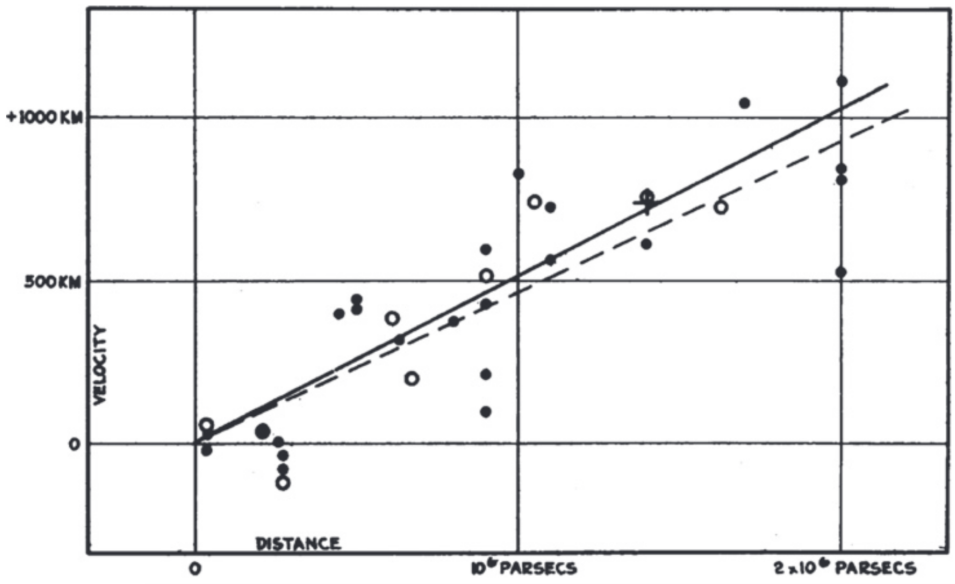

Figure 1.2: Relationship between velocity and distance for extragalactic nebulae [1]

This graphical representation depicts the essence of Hubble's Law, an elegantly simple yet profound principle. It states that a galaxy's velocity (v) is directly proportional to its distance (d) from us. The Hubble Law, along with its visual counterpart, the Hubble Diagram, describes an important concept: the universe is continuously expanding. Much like a rising loaf of bread, galaxies, akin to raisins within the dough, continually move away from each other at a uniform rate per unit of distance. Consequently, galaxies that reside farther from us recede at greater speeds than those situated nearby. This fundamental relationship, known as the Hubble Law, has been reproduced in the world of astronomy and is frequently featured in textbooks.

Although the expansion rate remains uniform in all directions at any given moment, it evolves throughout the Universe's existence. When expressed as a function of cosmic time, denoted as H(t), it becomes the Hubble Parameter. At present, the expansion rate, represented by H_0, is approximately 70 kilometres per second per megaparsec (where 1 megaparsec equals 3.26 million light-years).

The reciprocal of the Hubble Constant yields the Hubble Time, denoted as t_H, which measures the time since the beginning of the linear cosmic expansion. Consequently, it is linked to the age of the Universe, spanning from the moment of the Big Bang to the present day. For the aforementioned value of H_0, $t_H = 1/H_0$, is approximately 14 billion years.

1.1.1 The Dark matter

Our understanding of the Universe reveals that approximately 27% of its total energy content is composed of a mysterious form of matter known as dark matter (DM). This dark matter is fundamentally distinct from normal matter, which contributes to only about 5% of the Universe's energy [2, 3]. The rest of about 68% of the Universe's total energy is constituted by the dark energy [4]. The evidence supporting the existence of dark matter is compelling and consistent across various scales, ranging from galactic to cosmological phenomena [3]. It is important to note that dark matter has not been directly observed as of yet. All existing evidence for dark matter relies solely on its gravitational effects. However, there are several compelling reasons to investigate dark matter in laboratory settings:

- The prevailing "Weakly Interacting Massive Particle" (WIMP) paradigm suggests that dark matter is composed of particles known as WIMPs, which have extremely weak interactions with normal matter. These particles are expected to have energies accessible at or near the electroweak scale, a range crucial for explaining the observed relic density of particles resulting from the freeze-out of thermal equilibrium in the early Universe [5–7]. This electroweak energy scale is effectively probed by powerful experiments like the Large Hadron Collider (LHC) at CERN, located near Geneva, Switzerland [8].

- Additionally, numerous "beyond the standard model" (BSM) theories in high-energy physics require the existence of new particles at the electroweak scale. Some of these particles may serve as viable candidates for dark matter or interact with dark matter particles. A notable example of such a theory that bridges astrophysical and theoretical motivations is supersymmetry (SUSY). Supersymmetry not only addresses several known issues with the standard model, such as the hierarchy problem but also offers a compelling candidate for dark matter [9–11].

- In collider experiments, the primary experimental signature of dark matter is the presence of "missing transverse energy". This phenomenon arises because the particle responsible

for dark matter typically escapes the detector without being detected, leaving behind an imbalance in energy and momentum.

In summary, the quest to understand dark matter is driven by its significant contribution to the Universe's energy content and its profound gravitational effects. Laboratory investigations are motivated by the desire to explore the nature of dark matter, test theoretical models, and potentially uncover new physics phenomena through experiments that can detect the elusive particles associated with dark matter.

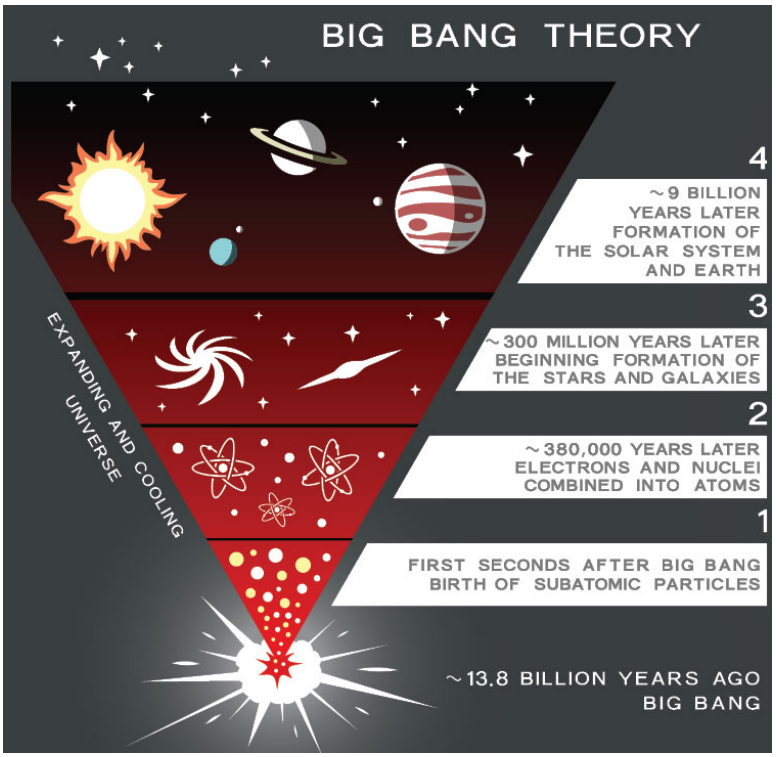

Figure 1.3: The Big Bang theory

Understanding the fundamental structure and principles of nature, from the biggest dimensions of the universe (such as galaxies, stars, etc.) all the way down to the smallest dimensions of quarks, is the goal of high-energy nuclear and particle physics. The study of ultra-relativistic heavy-ion collisions is one of the thriving research fields today, both from an experimental and theoretical standpoint. One can learn more about matter created under extreme conditions, such as high temperature and high energy density, by studying heavy-ion collisions.

According to Quantum Chromodynamics (QCD), which describes strong interactions, nuclear matter would undergo a phase transition under these extreme conditions to a deconfined state of quarks and gluons known as Quark Gluon Plasma (QGP). With experiments like AGS at BNL, SPS at CERN, the Relativistic Heavy Ion Collider (RHIC) at BNL, and the present Large Hadron Collider (LHC) at CERN, where the centre of mass collision energy may reach up to 13.6 TeV, the study of ultra-relativistic heavy-ion collisions has a history of around 35 years. The QCD theory is briefly introduced in this chapter along with a few examples of relevant ALICE measurements in order to explain the scientific motivation behind the experiment.

In the next section, a brief discussion on the standard model, quantum chromodynamics (QCD), ultra-relativistic heavy ion collisions, and the phase transition followed by the discussions on possible signatures of QGP has been done.

1.2 Standard Model

After the discovery of electrons by J. J. Thompson in the late 19^{th} century, several experiments and theories resulted in remarkable triumphs in the basic building block of matter. Later, several new particles were proposed theoretically and successfully discovered experimentally. However, till 1961, no classification of a huge number of particles was available. Inspired by Mendeleev's way of classification of elements, in the early 1970s, Gell-Mann introduced the eight-fold way to classify the hadrons for the first time. This classification was based on the electric charge and net strangeness. In 1970, Zweig and Gell-Mann proposed the quark model independently which stated that hadrons are composed of quarks [12]. This superseded the eight-fold way.

In 1970, Glashow, Salam and Wienberg proposed the Standard Model, a theory that describes three of the four known fundamental forces of nature (strong, weak and electromagnetic), which is successful in explaining experimental results of elementary particles with high precision [13–15]. The Standard model was postulated to be a quantum field theory (QFT) based on the gauge symmetry $SU(3)_C \times SU(2)_L \times U(1)_Y$. In the standard model, the elementary particles are characterized by quantum numbers such as the spin (S), baryon (B) and lepton (L)

numbers and electric charge (Q). The schematic representation of the standard model is depicted in Fig. 1.4.

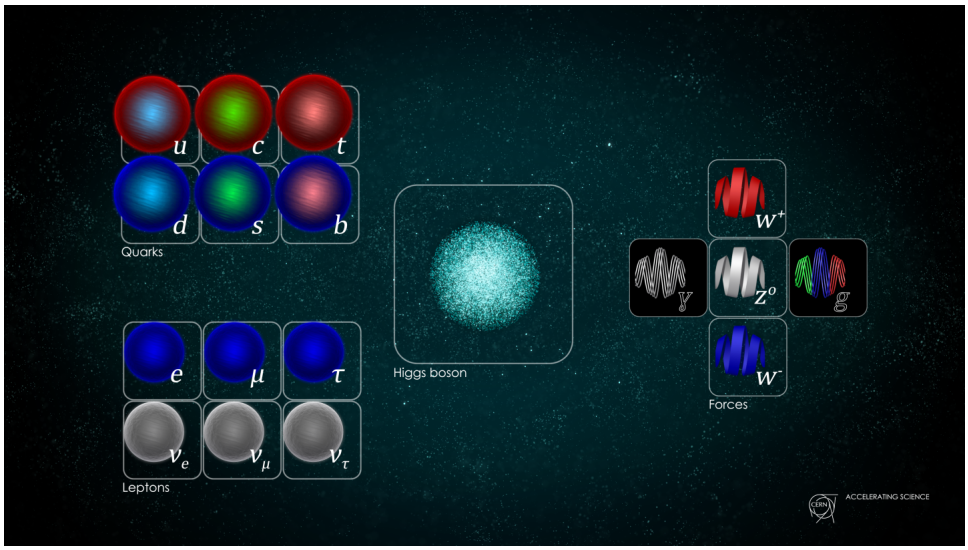

Figure 1.4: A representation of the standard model. The figure is taken from [16].

As per the standard model, the Universe is constituted by the elementary particles that make up the visible matter. They are classified into quarks, leptons, gauge and Higgs bosons. The quarks are distinguished by six flavors of quarks namely up (u), down (d), strange (s), charm (c), top (t) and bottom (b). The first generation of quarks are most stable and they are the lightest. The second and third generations consist of less stable particles and they are heavier in nature. Similar to quarks, there are also 6 types of leptons, *i.e.,* electron (e), electron-neutrino (ν_e), muons (μ), muon-neutrino (ν_μ), tau (τ) and tau-neutrino (ν_τ). Both quarks and leptons are fermions and are spin-1/2 particles. Quarks combine together to form hadrons which can further be classified into baryons and mesons. Hadron consisting of a quark-antiquark pair is called a meson while three quarks(or anti-quarks) are combined to form baryons. However, baryons like Δ are made up of three up-or-down quarks. As the three quarks inside a baryon cannot be identical due to Pauli's exclusion principle, a new quantum number, the color charge was introduced. Every quark carries a color charge (red, blue or green) and they have a fractional electric charge.

The carriers of the fundamental forces are called gauge bosons. There are four fundamental forces namely, the strong force, the weak force, the electromagnetic force and the gravitational force. Strong and weak forces have short range and they are effective only at sub-atomic levels, while electromagnetic and gravitational forces have infinite range. The gluons (g) are the mediator of the strong force and they also carry the color charge. The weak force is mediated by the $W^{\pm}$ and Z bosons. The photons (γ) are the carriers of electromagnetic force. The prescribed form of the standard model stands complete after the recent discovery of the Higgs boson at the Large Hadron Collider (LHC), CERN, Geneva. Higgs boson is responsible for the mass of elementary particles.

The field theory which governs the electromagnetic interaction is called Quantum electrodynamics (QED). The unified electromagnetic and weak force is governed by the Electroweak theory. The strong interaction is governed by Quantum Chromodynamics (QCD), which is briefly discussed in the next section.

1.3 Quantum Chromodynamics (QCD)

QCD, the field theory which governs the strong interaction, is responsible for the confinement of nucleons inside nuclei and quarks inside hadrons [17, 18]. QCD derives its name from the Greek word "chromos" meaning "colour".This field theory, akin to Quantum Electrodynamics (QED) governing electromagnetic interactions, shares similarities, yet presents distinct differences. Unlike the single electric charge and its anti-charge in QED, QCD introduces three color charge states and their corresponding anti-states. Both theories employ massless gauge bosons for interactions. However, unlike photons, gluons that carry color charge, can interact with each other.

In QCD, the color charge is conserved in strong interactions and follows a SU(3) symmetry, where ‘SU’ stands for the special unitary group which is the group of unitary matrices whose determinant is equal to unity. Unlike quarks, which can combine to form color-neutral particles (such as mesons and baryons), gluons, due to their own color charges, cannot exist in a color-neutral state. As a result, eight distinct types of gluons exist, reflecting the richness of

the strong interaction described by QCD's SU(3) symmetry. This is a fundamental property of QCD. The quarks interacting through gluons in QCD are similar to the QED coupling of photons and fermions. Unlike photons, gluons can interact among themselves enabling complex QCD processes. The effective potential ($V(r)$) between partons governed by QCD is given as,

$$V(r) = -\frac{4}{3}\frac{\alpha_S}{r} + kr, \tag{1.3}$$

where, α_S is the strong coupling constant. It is also known as a running coupling constant due to its explicit dependence on the momentum transfer scale. r is the distance between partons and k is the color string tension constant ($\simeq 0.85$ GeV fm^{-1}) [19].

QCD has two important features called asymptotic freedom and confinement, which are discussed in the next subsections.

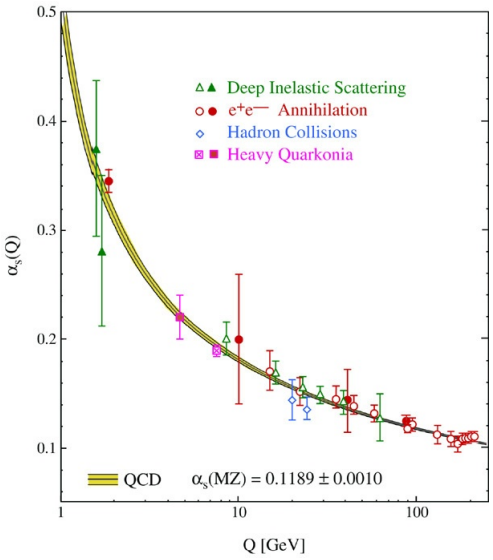

Figure 1.5: The strong coupling constant (α_S) as a function of momentum transfer [20].

1.3.1 Asymptotic Freedom

One of the most unique features of QCD is asymptotic freedom. David J. Gross, H. David Politzer and Frank Wilczek were awarded jointly the Nobel Prize in Physics in 2004 for the discovery of asymptotic freedom in the theory of the strong interaction [21]. It states that,

with the decrease in distance between the partons, the strength of interaction between partons becomes smaller and the energy density gets higher.

One can notice in Eq. 1.4 that α_S is not really a constant but a function of momentum transfer. This is an outcome of gluon or quark pairs vacuum polarization. The quark-antiquark pair created and annihilated in the vacuum can be polarized by the color charge similar to a molecule that can be polarized by an electric charge in a dielectric medium. Similarly, the quark polarization screens the color charge in QCD which is similar to electric charge screening in QED. However, the key difference with respect to the QED is the self-interaction among gluons which smears the color charge of quarks. This creates an anti-screening effect. This effect in QCD causes the strong coupling to become small at a short distance (large momentum transfer) and it causes the quarks inside hadrons to behave as free particles when probed at high energy.

The α_S as a function of momentum transfer (Q^2) is given as,

$$\alpha_S(Q^2) = \frac{12\pi}{(11n - 2n_f)ln(Q^2/\Lambda^2_{QCD})}, \tag{1.4}$$

where Λ_{QCD} is the non-perturbative QCD scale parameter and the perturbative QCD is applicable above $\Lambda_{QCD} \simeq 200$ MeV. n_f is the number of quark flavours. At lower values of momentum transfer ($Q \sim 1$ GeV/c^2), $\alpha_S(Q^2)$ grows and the perturbative theory breaks down. However, in the denominator, the anti-screening effect will dominate if $11n$ becomes higher than $2n_f$. The strong coupling constant will decrease with an increase of Q^2. Thus, at very short distances, which corresponds to high momentum transfer, the value of $\alpha_S(Q^2)$ becomes very small, making the coupling weak. When Q^2 tends to a very large value (*i.e.*, ∞), the coupling strength becomes almost negligible making the quarks and gluons behave as free particles inside the QCD vacuum. This feature is called asymptotic freedom [17]. When the coupling becomes small, the perturbative QCD is applicable. Fig. 1.5 depicts the value of $\alpha_S(Q^2)$ estimated by different systems such as deep inelastic scattering, e^+e^- annihilation and hadron collisions.

1.3.2 Confinement

In addition to the asymptotic freedom, the QCD potential has another salient feature where the quarks exhibit color confinement. This means an isolated quark cannot be found in nature. Similar to Coulomb potential, the first term of Eq. 1.3 indicates that with increasing distance between the two color charges, the linear term dominates and the strength of the potential increases. This term arises from a single gluon exchange and dominates at small r. Thus to get free quarks, one requires nearly infinite energy. When the separation between two quarks increases, a string is formed due to the gluon self-coupling as the color field lines are attracted. At a large distance, when the potential energy becomes large enough, a quark-antiquark pair is created instead of producing two free quarks. Due to this feature of the QCD potential, the quarks are always confined [19].

1.4 QCD phase transition and Quark-Gluon Plasma (QGP)

Based on the temperature and the density of the system, QCD calculations suggest that strongly interacting matter can exist in different phases. A system of deconfined states of quarks and gluons, also called quark-gluon plasma (QGP) is brought into a confined state where partons are confined inside hadrons via a phase transition characterised by a specific critical temperature and baryo-chemical potential. Thus, by reproducing similar temperature and energy density conditions, this QCD phase transition can be investigated in the laboratory leading to the QGP formation with the help of ultra-relativistic heavy-ion collisions. In such heavy-ion (A–A) collisions, a large number of nucleon-nucleon interactions take place in a very small region in space, which provides significantly high energy density to allow the creation of the QGP state. When the collision energy is high enough for the phase transition of deconfined matter to occur, the initial state is expected to be made up of solely strongly interacting quarks and gluons. This phase later hadronises, when the system cools down. This particular evolution of the system in heavy-ion collisions is believed to reproduce the stages of evolution in the early Universe after the electro-weak phase transition from the deconfined state of quarks and gluons to confined

hadrons, nearly few μs after the Big Bang. Therefore, heavy-ion collisions at ultra-relativistic energies are often referred to as Little Bang.

1.4.1 Thermodynamics of QCD

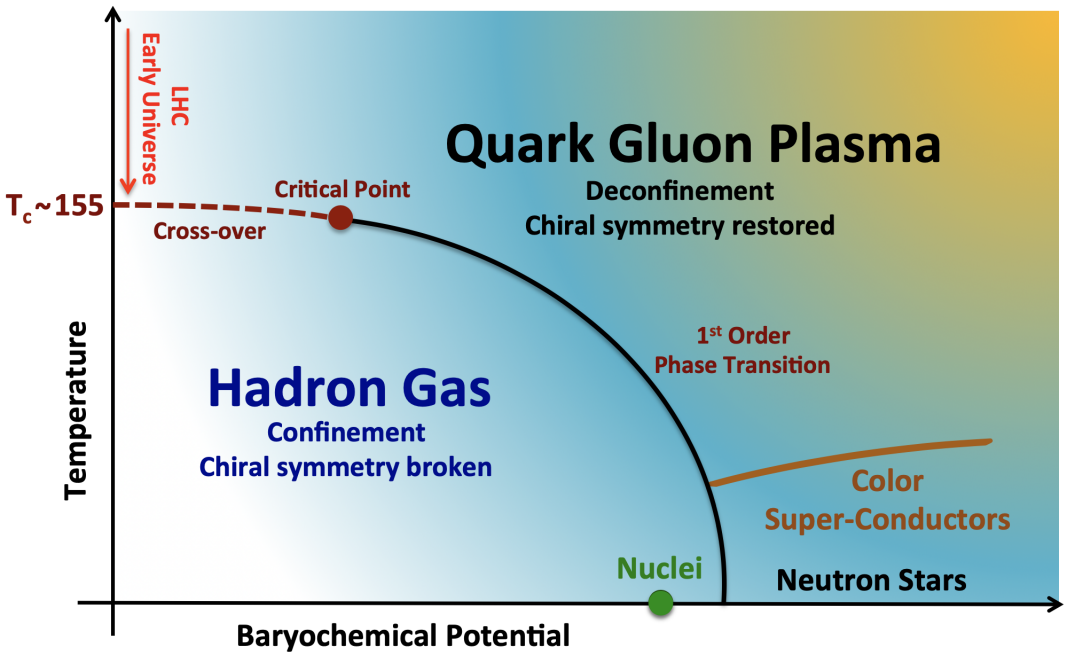

Figure 1.6: Schematic view of QCD phase diagram [22]

Figure 1.6 shows the schematic view of the QCD phase diagram which has possible states of strongly interacting matter confined in it. The x-axis represents the baryon chemical potential (μ_b) and the y-axis represents the temperature (T) of the system. As shown in the phase diagram of QCD, strongly interacting matter can exist in different phases which are characterized by temperatures and densities. The μ_B is defined as the amount of energy needed to increase the total number of baryons N_B by one unit in a system, i,e., $\mu_B = \frac{\partial E}{\partial \mu_B}$. At relativistic energies, the baryon number in a system may not be conserved due to particle annihilation and creation processes at the microscopic level. Thus, μ_B is introduced. Low baryon chemical potential ($\mu_B \sim m_p \sim 1$ GeV) in the phase transition diagram corresponds to the nuclear matter in its normal state. Based on how fast the free energy of the system varies near the transition temperature, the order of a phase transition is governed. When the first differential of the free energy is

discontinuous accompanied by a discontinuous variation of entropy along with the presence of latent heat, a first-order transition occurs. In a similar way, the second-order transition occurs when the second differential of the free energy is discontinuous. In a special case, a phase transition is called a crossover transition if it occurs without any discontinuity of free energy. At the critical point, two states of matter can coexist at the same time. The phase transition governed by QCD is expected to be of the first-order transition until the critical endpoint is achieved. From the lattice QCD calculations, strong evidence of a crossover phase transition is expected at T $\simeq$ 160 MeV and $\mu_b \simeq 0$ [23, 24]. An assumption of first-order phase transition is considered at higher μ_b and the first-order transition is thought to reach the position of the transition to the cross-over region [25, 26]. However, the precise information on the properties and the location of the phase transition from hadrons to the QGP are still unknown.

The pressure of hadronic phase as a function of temperature can be expressed via the Stefan-Boltzmann law:

$$P_{HG} = g\frac{\pi^2}{90}T^4, \tag{1.5}$$

where g is the degeneration factor that signifies the degrees of freedom of the system. The degrees of freedom in deconfined QGP state increase to include fermionic (3 colors $\times$ N_f flavours $\times$ 2 spin states) and bosonic (2 spin $\times$ 8 color states for gluons) degrees of freedom. The pressure is now given as,

$$P_{HG} = g\frac{\pi^2}{90}T^4 - B, \tag{1.6}$$

where, B is the bag constant [17]. $B^{-1/4} \simeq 0.2$ GeV, acts as an external pressure, which is equivalent to some sort of latent heat. It is defined as the difference in energy density per unit volume between the two different phases of the QCD matter.

At the beginning of the Universe, it is a widespread belief that matter formed in the Big Bang evolved from very high temperatures to the formation of hadrons. This process features a small quark–antiquark excess ($\sim 10^{-9}$), which corresponds to $\mu_B \sim 0$. At the LHC, the nuclear matter formed in heavy-ion collisions is compressed and heated enough to undergo the formation of QGP, at a low baryon chemical potential. In contrast, a neutron star can represent a case of production of QGP via large baryonic density and very low temperature which is induced

by the collapse of a star due to gravity. However, for extreme values of chemical potential (μ_B), the nuclear matter would be in conditions of quark–colour superconductivity.

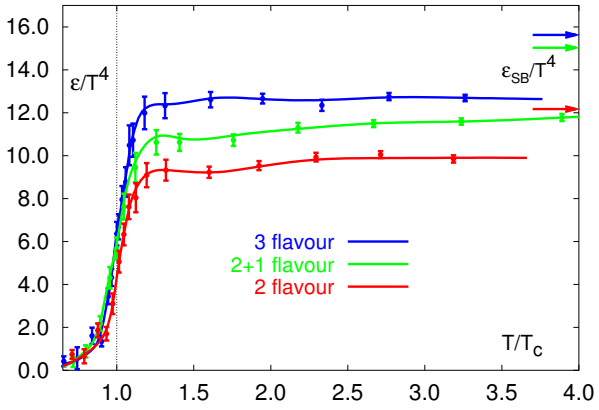

Figure 1.7: The predictions from Lattice QCD calculations of ε/T^4 as a function of temperature normalized by the critical temperature (T_C) and the Stefan-Boltzmann limit is shown as the horizontal arrows [27].

The lattice QCD calculations predict a phase transition from a hadronic to QGP phase at temperatures of about 154-170 MeV [27, 28]. Fig. 1.7 shows the predictions from Lattice QCD calculations of ε/T^4 as a function of temperature normalized by the critical temperature (T_C). The calculations are shown for $\mu_B = 0$ and considering 2 and 3 light (u and d) quarks, or with 2 lights and 1 heavier (strange quark). The case with 2+1 is the closest to the physically achieved quark mass spectrum. In this ratio, the steeper trend reflects the increase in degrees of freedom of the system while in the phase of deconfinement.

1.5 Heavy-ion collisions at the LHC

At the LHC, heavy nuclei like Pb ions are accelerated at ultra-relativistic energies and they appear as Lorentz contracted "Pancakes" while traversing along the beam axis. Fig. 1.8 depicts a schematic of ultra-relativistic heavy ion collisions at the LHC. The nucleons which participated in the collisions are called “participants” (N_{part}) and those that do not participate in the collisions are called “spectators” ($N_{spect} = 2A - N_{part}$, where A is the mass number). Fig. 1.9

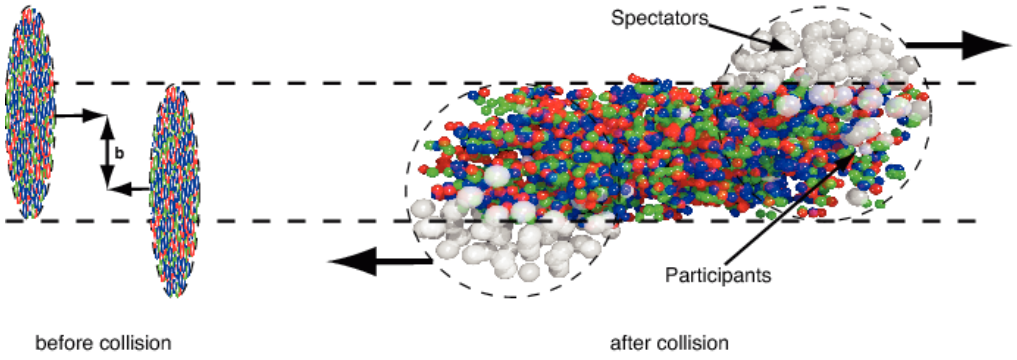

Figure 1.8: Depiction of ultra-relativistic heavy ion collisions at the LHC [29].

shows a geometrical picture of the transverse plane in the collision of two heavy ions where traditionally, the beam axis is considered as the z-axis. Event plane is defined by the impact parameter (b) vector and the event plane angle (Ψ_R) as shown in Fig. 1.9.

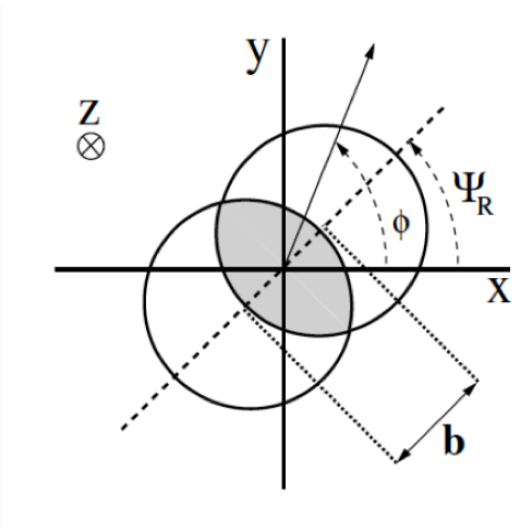

Figure 1.9: A schematic of the plane of ultra-relativistic heavy ion collisions in the transverse direction [30].

One of the key parameters, impact parameter (b) is defined as the perpendicular distance between the centres of the two nuclei. It essentially quantifies the extent of the overlap region of the nuclei after the collision. A small impact parameter signifies the central collisions indicating that the collision is almost head-on. For central collisions, most of the nucleons inside the heavy ions interact in the collision with each other. Thus, one would expect that the central collisions

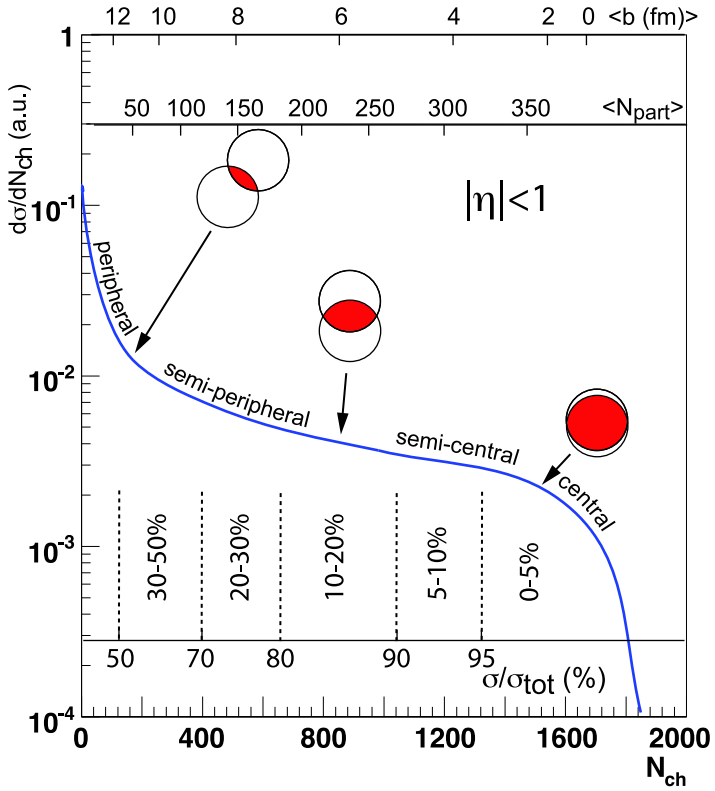

Figure 1.10: Cartoon depicting the correlation of the impact parameter and number of participants with final state charged particle multiplicity [31].

would have maximum multiplicity in the final state. In contrast, peripheral collisions have larger impact parameters and fewer nucleons participate in the collision.

Fig. 1.10 shows the correlation between the impact parameter and the number of participants with final state charged-particle multiplicity. Usually, centrality classes are defined in terms of percentiles of the total hadronic cross-section in nucleus-nucleus collisions. Finding the number of participants, spectators and defining centrality classes in heavy-ion collisions is crucial as they are essential to normalize different observables prior to their comparison with different models or other collision systems. Experimentally the selection of centrality can be

performed either by measuring the number of final-state charged particles in the collision [30] or from the measurement of the number of spectators in the collision. The first method relies on a geometrical model which is applicable for the hadronic processes while the latter exploits the measurement of the spectator nucleons' energy in the very forward detectors like zero degree calorimeter (ZDC). For small collision systems, like pp and p–Pb, a similar method based on final state charged particle multiplicity is to divide the events in multiplicity classes.

1.5.1 Space-time evolution

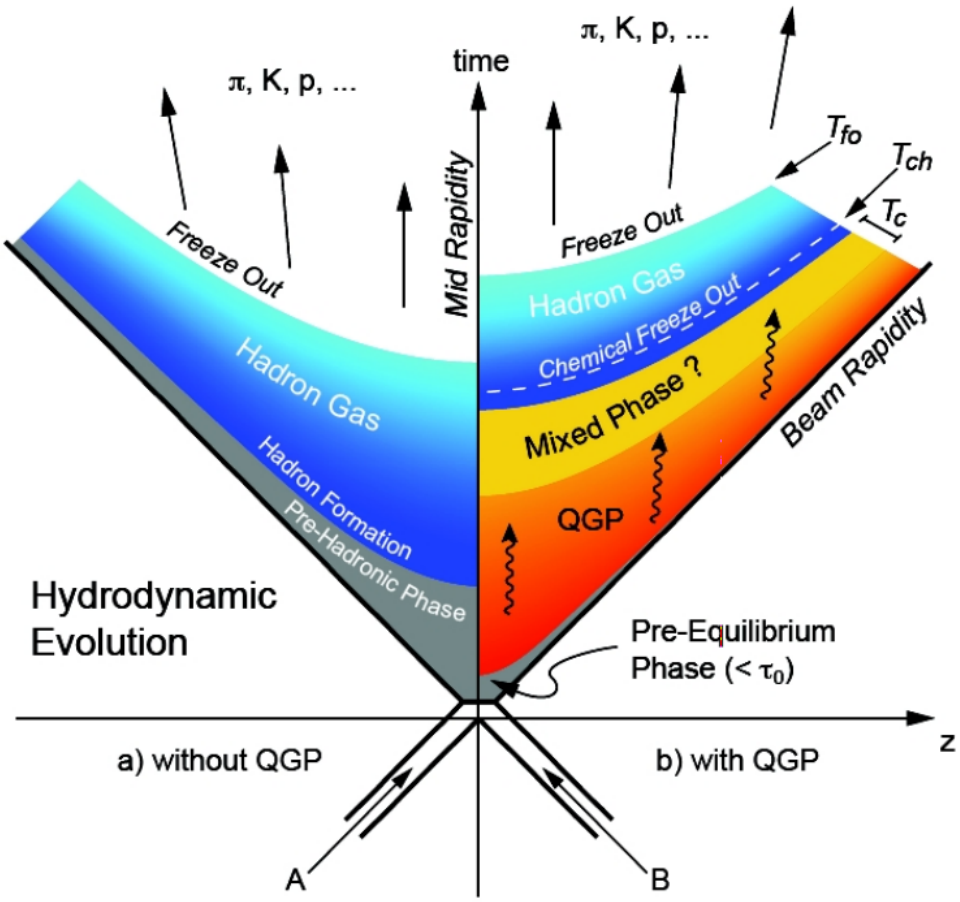

Figure 1.11: Schematic of space-time evolution of ultra-relativistic nucleus-nucleus collision [32].

Fig. 1.11 shows the schematic of the space-time evolution in ultra-relativistic nucleus-nucleus collisions. To understand the evolution in detail, the start and end time of a collision

between two heavy ions are at $t = 0$ and $z = 0$ respectively. The right side of the figure shows the scenario of formation of a very hot and dense deconfined state of matter, which is expected to be produced in central heavy-ion collisions. The various stages of the evolution are the following.

- **Pre-equilibrium stage:** This refers to the initial stage of collision, where a large amount of energy is deposited. The parton-parton hard scatterings lead to the deconfined state of the matter. For $t \leq 1\ fm/c$, the interaction among quarks and gluons give rise to the production of deconfined quarks and gluons. High transverse momentum particles are mostly produced in this stage.

- **Evolution of QGP:** After the pre-equilibrium phase, the equilibrated system of deconfined quarks and gluons is formed due to multiple partonic interactions. This thermally equilibrated state is known as QGP phase. Due to very high temperature and internal pressure, the system begins to expand rapidly till the temperature of the QGP reaches a critical temperature T_c. At this temperature the partons start to get confined within the hadrons and a "mixed phase", consisting of a mixture of QGP and hardrons is expected to be formed.

- **Hadron gas phase:** There are two possible mechanisms of hadronization from QGP, namely quark coalescence and fragmentation of partons. Hadronization from fragmentation mostly happens at high energy which occurs when a high-p_{T} parton fragments into lower p_{T} hadrons. Coalescence occurs when partons with lower momenta combine to form high-p_{T} hadrons. After hadronization, the interactions among hadrons continue with each other via elastic and inelastic interactions until they freeze out and traverse to the detectors. When the inelastic collisions cease, the system reaches chemical freeze-out and the corresponding temperature is called chemical freeze-out temperature. However, the elastic collision among hadrons continue till the mean free path of the hadrons exceeds the system size. This is called kinetic or thermal freeze-out and the corresponding temperature is known as the kinetic freeze-out temperature (T_{fo}). After the kinetic or thermal freeze-out, all the particles freely stream towards the detectors.

In contrast, another possible scenario of space-time evolution can also be possible when the matter produced in the ultra-relativistic collisions does not meet the criteria of high temperature/energy density and such a scenario is depicted in the left side of Fig. 1.11. Here, the system is left with only hadronic degrees of freedom and after the collisions, a pre-hadronic phase is created. The nucleons interact amongst themselves to form new hadrons which can be detected in the detectors after the freeze-out.

1.6 Signatures of QGP and experimental probes

Since the QGP has a relatively brief lifespan (few fm/c), it cannot be directly observed like ordinary electromagnetic plasma. If a QGP medium is created, it expands, cools, and hadronizes to produce hadrons in their final state. In the experiment, it is impossible to witness each stage independently. Instead, one may measure the final state observables that are time-integrated, such as the multiplicities of charged particles, photons, or leptons, the transverse momentum spectra of different particles, energy, anisotropic flow, etc. Nevertheless, different processes during the time evolution of fireball led to the final state observables that preserved some information over time. Some of the QGP signatures such as strangeness enhancement, anisotropic flow, J/ψ suppression, jet quenching, etc. are briefly discussed in the following sub-sections.

1.6.1 Strangeness Enhancement

"Strangeness enhancement" denotes the phenomenon where, in specific high-energy nuclear collisions, there is a greater-than-expected production of strange quarks.

The increased production of strange particles may indicate quark-gluon plasma (QGP) formation [33]. To assess the extent of strangeness enhancement, it is necessary to compare the abundance of strange particles between the QGP and hadronic phases. This comparison is essential due to differences in the production mechanisms and rates of strange particles in a hadron gas compared to a QGP medium.

In a quark-gluon plasma (QGP), the primary process for the formation of $s\bar{s}$ pairs occurs through the dominant channel $g\bar{g} \rightarrow s\bar{s}$, owing to the higher gluon density. In contrast, in proton-proton (pp) collisions, where QGP medium formation is not anticipated, the primary channel for strangeness production involves the annihilation of light quarks to produce strange quarks in the $q\bar{q} \rightarrow s\bar{s}$ channel.

The enhancement factor (E) is defined as,

$$E = \frac{2}{\langle N_{part} \rangle} \left[\frac{\frac{dN^{AA}}{dy}|_{y=0}}{\frac{dN^{pp}}{dy}|_{y=0}} \right]. \tag{1.7}$$

Here, $\langle N_{part} \rangle$ denotes the mean number of participants. $\frac{dN^{AA}}{dy}|_{y=0}$ denotes the integrated yield of strange and multi-strange in heavy-ion collisions, while $\frac{dN^{pp}}{dy}|_{y=0}$ represents the integrated yield in proton-proton (pp) collisions.

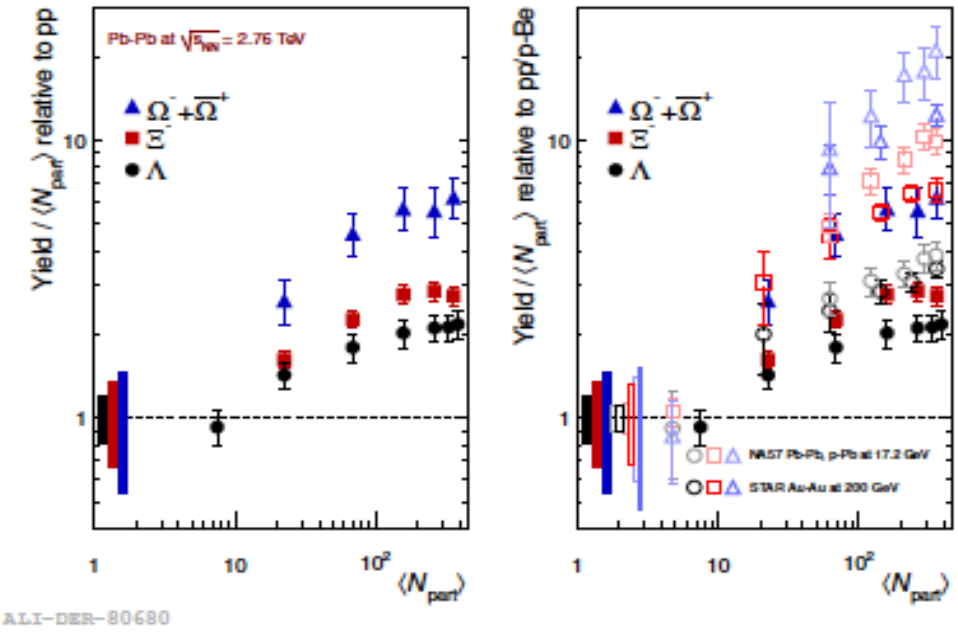

Figure 1.12: The yield of multi-strange hadrons in Pb-Pb collisions relative to pp collisions measured in ALICE (left) and NA57, STAR (right) as a function of $\langle N_{\text{part}} \rangle$ [34–36].

In Figure 1.12, the hyperon yield enhancement factor (E) as a function of centrality $\langle N_{\text{part}} \rangle$ is shown [34–36]. The significant increase in the production of strange particles in Pb-Pb collisions compared to small collision systems strongly suggests the formation of a deconfined state

of matter at LHC energies. Additionally, it is noteworthy that the enhancement factor is more pronounced for particles containing higher number of strange quarks.

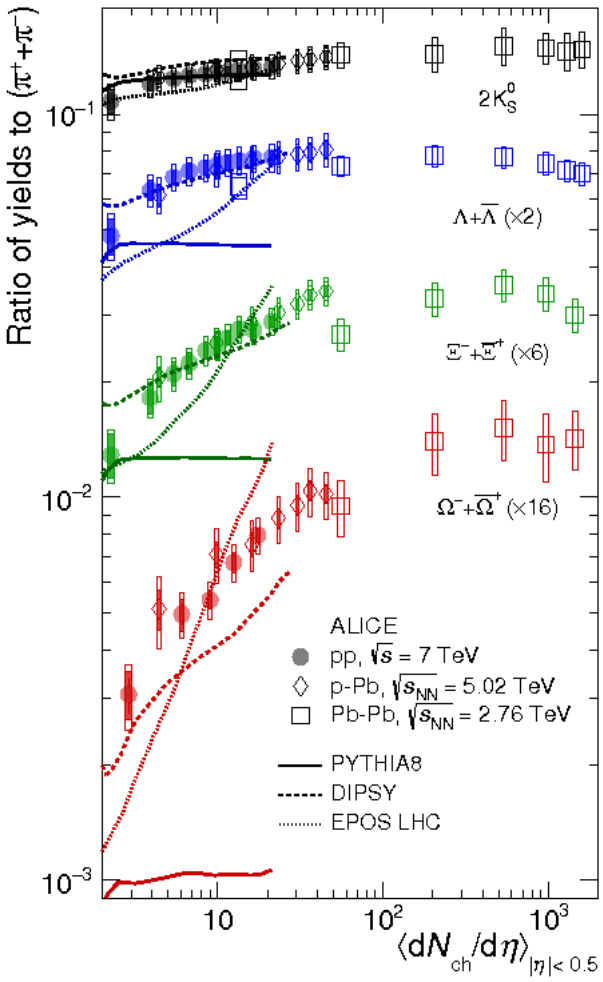

Figure 1.13: Enhanced strangeness production as a function of charged particle multiplicities for different collision systems [37].

Remarkably, the measurements published by ALICE in 2017 [37] constitute some of the most compelling evidence supporting the presence of QGP-like conditions in proton-proton (pp) collisions as well, which is depicted in Fig. 1.13. ALICE's observation of enhanced strange particle production in high-multiplicity pp collisions, a phenomenon historically associated with QGP formation [37], underscores this significant discovery.

1.6.2 Anisotropic flow

The evolution of the fireball exhibits collective phenomenon referred to as "elliptic flow." In case of peripheral collisions, where the impact parameter has a finite value, the collision between two heavy ions give rise to an almond-shaped region of overlap at the collision point, while the spectators move away from each other.

This leads to an asymmetry in the geometry, resulting in a disparity in the pressure gradient within the overlapped region. Specifically, the pressure gradient along the x-axis surpasses that along the y-axis, as depicted in Fig. 1.14 (left panel). Consequently, the medium experiences an expansion predominantly in the x-direction due to the emission of a greater number of particles in that direction. This initial spatial anisotropy ultimately manifests as a final particle anisotropy in momentum space, as illustrated in Fig. 1.14.

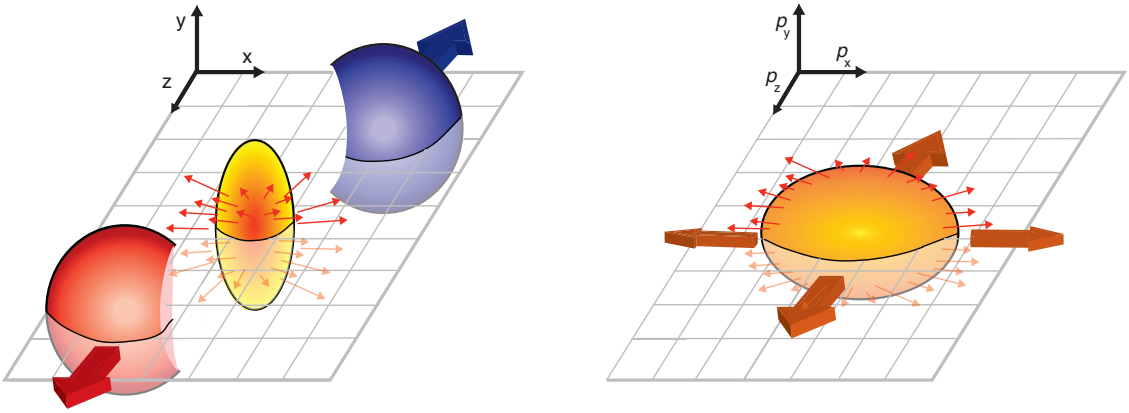

Figure 1.14: A schematic diagram of conversion of spatial anisotropy (left panel) to momentum anisotropy (right panel).

The deviation from isotropy in the azimuthal particle distributions can be characterized by employing a Fourier expansion in the azimuthal angle ϕ [38, 39], as follows:

$$\frac{dN}{p_T dp_T d\phi dy} = \frac{dN}{2\pi p_T dp_T d\phi dy}\left[1 + 2\sum_{1}^{\infty} v_n cos[n(\phi - \psi_R)]\right], \tag{1.8}$$

where v_n is the Fourier coefficient of order n and denotes the order of flow harmonics. For example, v_1 is for directed v_2 for elliptic and v_3 is the triangular flow. When v_n is large, the emission has a considerable anisotropic component, but when v_n is zero, the emission is

completely isotropic. p_T is the transverse momentum, y is the rapidity, ϕ is the azimuthal angle and ψ_R is the event plane angle.

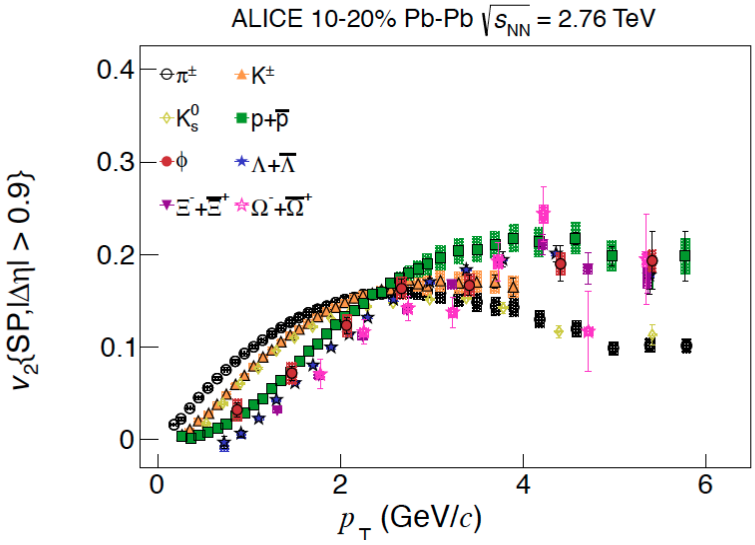

Figure 1.15: Elliptic flow as a function of p_T for 10 - 20 % centrality class in Pb-Pb collisions at $\sqrt{s_{NN}}$ = 2.76 TeV for different particle species [40]

Elliptic flow (v_2) is measured for identified mesons ($\pi^{\pm}, K^{\pm}, K^0_s, \phi$) and baryons ($p, \Lambda, \Xi^-, \Omega^-$ and their antiparticles) as a function of p_T in the range 0.2 - 6.0 GeV/c within Pb-Pb collisions at $\sqrt{s_{NN}}$ = 2.76 TeV, conducted by the ALICE collaboration [40]. The results are illustrated in Fig. 1.15.

It is noteworthy that for $p_T < 2$ GeV/c, there exists a systematic ordering based on the mass of particles, with heavier particles displaying smaller v_2 values than lighter particles. This mass-based ordering encompasses both radial flow and elliptic flow effects. In general, heavier particles exhibit lower radial flow than lighter ones in the low p_T regime. The reduction in elliptic flow for heavier particles is attributed to the fact that the in-plane expansion velocity of the system surpasses the out-of-plane velocity due to azimuthal asymmetry within the system. This observation underscores the properties of the Quark-Gluon Plasma (QGP) as an almost perfect fluid.

1.6.3 Jet quenching

The discovery of high transverse momentum (p_T) hadrons suppression represents one of the intriguing results at RHIC, providing a compelling hint of quark-gluon plasma (QGP) formation [41]. In relativistic heavy-ion collisions, extremely high-p_T partons are created, radiating outward in all directions from the collision points and subsequently fragmenting into narrow cones of hadrons, known as jets. The initial partonic jets, upon traversing the thermalized QGP medium, these jets interact with the constituent particles within the medium, shedding energy and gradually losing momentum before undergoing hadronization. Consequently, suppression of high momentum particles is observed in nucleus-nucleus collisions when compared to corresponding data from proton-proton (pp) collisions, normalized by the number of binary collisions [42, 43]. This phenomenon is known as jet quenching, and the suppression of high-p_T particles is typically expressed by the nuclear modification factor (R_{AA}).

$$R_{AA}(p_T) = \frac{1}{\langle T_{AA} \rangle} \times \left[\frac{(\frac{d^2N}{dp_T dy})_{AA}}{(\frac{d^2N}{dp_T dy})_{pp}} \right]. \tag{1.9}$$

R_{AA} represents the ratio of the invariant yield in heavy-ion (A-A) collisions to that in proton-proton (pp) collisions, scaled by the average nuclear overlap function, denoted as $\langle T_{AA} \rangle = \langle N_{coll} \rangle / \sigma_{inel}$, where $\langle N_{coll} \rangle$ denotes the average number of binary collisions and σ_{inel} refers to the inelastic pp cross-section. When R_{AA} equals 1, it suggests that heavy-ion collisions are a simple linear superposition of proton-proton collisions, implying the absence of quark-gluon plasma (QGP) formation. Conversely, any deviation from unity at high transverse momentum (p_T) signals quenching or enhancement phenomena within the high-density medium.

Fig. 1.16 shows the variation of R_{AA} as a function of p_T for charged hadrons ($h^{\pm}$) and neutral pions (π^0) in Au–Au and Pb–Pb collisions. The high-p_T suppression of hadrons in dense QGP medium could be seen for both RHIC and LHC energies.

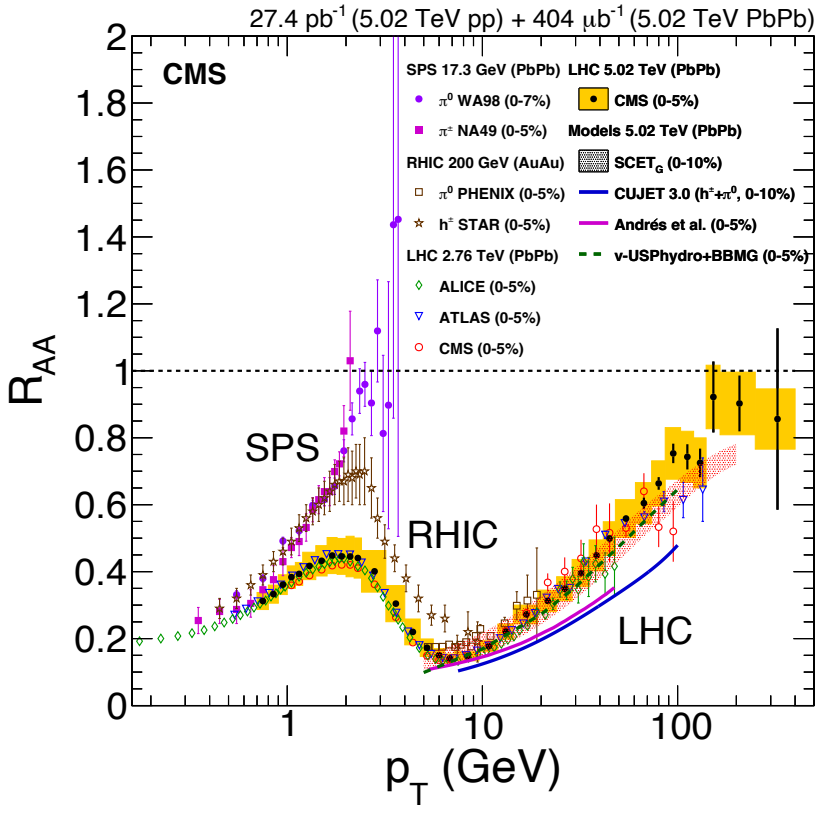

Figure 1.16: $R_{AA}(p_T)$ for charged hadrons ($h^{\pm}$) and neutral pions (π^0) in central heavy-ion collisions at SPS, RHIC and the LHC [41].

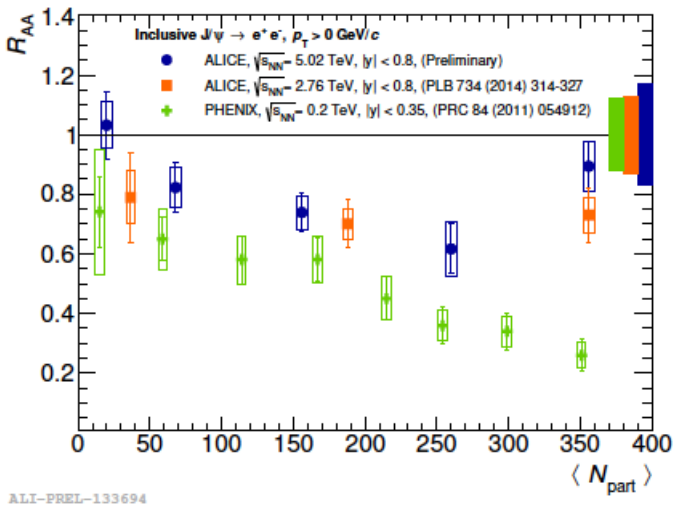

Figure 1.17: R_{AA} of J/ψ as function of centrality in Pb–Pb collisions at $\sqrt{s_{NN}}$ = 2.76 and 5.02 TeV and Au+Au collisions at $\sqrt{s_{NN}}$ = 200 GeV.

1.6.4 J/ψ suppression

The formation of the bound state of a charm quark and its anti-quark, known as $c\bar{c}$ (J/ψ), is anticipated to occur in the early stages of both hadronic and nuclear collisions. Consequently, the J/ψ particle serves as a valuable probe for investigating the initial dynamics of the medium created in heavy-ion collisions. Theoretical models predict that the production of J/ψ in heavy-ion collisions should be suppressed when compared to proton-proton (pp) collisions [44]. This suppression occurs because the quark-gluon plasma (QGP) screens the color charge of the quarks, which reduces the production of J/ψ. Significant suppression of J/ψ particles is indeed observed in heavy-ion collisions, indicating the presence of a QGP. Simultaneously, the disassociation of charm quarks leads to an increase in the production of open charm mesons ($D^0, D^{\pm}$). The phenomenon of J/ψ suppression was first observed at the Super Proton Synchrotron (SPS)[45] and later at the Relativistic Heavy Ion Collider (RHIC)[46, 47] energies, providing compelling evidence for the formation of the quark-gluon plasma.

Figure 1.17 illustrates the nuclear modification factor (R_{AA}) of J/ψ particles in Pb-Pb collisions at center-of-mass energies $\sqrt{s_{NN}}$ = 2.76 and 5.02 TeV, as well as in Au+Au collisions at $\sqrt{s_{NN}}$ = 200 GeV, plotted as a function of centrality. Notably, the suppression observed at LHC energies is less pronounced compared to RHIC and SPS energies [46]. This relative enhancement in the yield of J/ψ particles at the LHC is attributed to the recombination or coalescence of charm quarks during the hadronization process.

1.6.5 Electromagnetic Probes

Photons and di-leptons serve as essential electromagnetic probes, providing valuable insights into the properties of the quark-gluon plasma (QGP)[49–51]. These probes are particularly advantageous as they do not undergo strong final state interactions, making them ideal for penetrating the strongly interacting QCD (Quantum Chromodynamics) matter[52]. In heavy-ion collisions, photons and dileptons can originate from various processes during the initial hard scattering, such as annihilation ($q\bar{q} \rightarrow \gamma g, q\bar{q} \rightarrow \gamma\gamma$), Bremsstrahlung ($qg \rightarrow gq^* \rightarrow q\gamma g$), fragmentation ($qg \rightarrow qg^* \rightarrow q\gamma X$), Compton scattering ($qg \rightarrow \gamma q$), and pair production ($q\bar{q} \rightarrow l\bar{l}$).

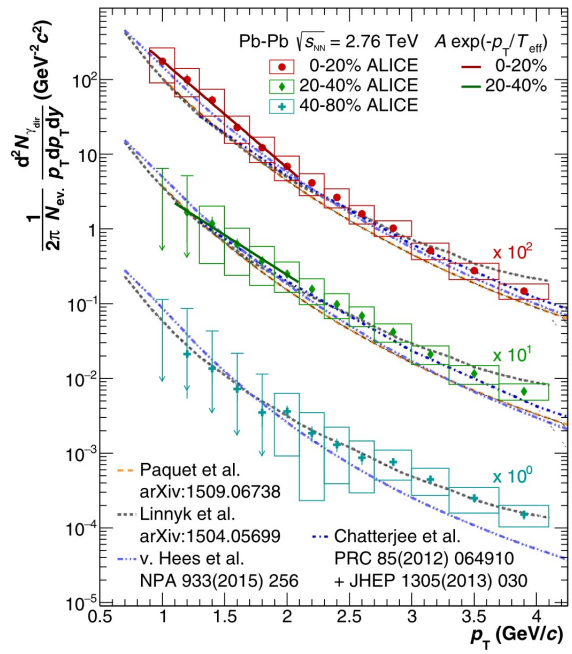

Figure 1.18: Comparison of direct photon spectra in Pb–Pb collisions at $\sqrt{s_{NN}}$ = 2.76 TeV for different centrality classes with model calculations [48]

With the exception of decay photons, these particles are often referred to as direct or prompt photons. High-p_T photons, originating directly from the initial hard scattering, are valuable for determining the momentum of associated partons. This capability enables the study of parton energy loss within the medium, making them useful probes for investigating phenomena like gluon saturation. In contrast, thermal photons are emitted within the dense QGP matter and carry information about the QGP's temperature.

Figure. 1.18 shows the direct photon spectra in Pb–Pb collisions at $\sqrt{s_{NN}}$ = 2.76 TeV for the 0–20% (scaled by a factor of 100), the 20–40% (scaled by a factor of 10), and 40–80% centrality classes are compared with model calculations from Refs. [53–56]. All models incorporate a contribution from pQCD photons. Additionally, for the 0–20% and 20–40% classes, the fit with an exponential function is shown. An inverse slope parameter of T_{eff} = (297 $\pm 12^{stat} \pm$ 41^{syst}) MeV is derived for the 0–20% most central collisions. This determination is based on an exponential function fit to the direct photon spectrum within the 0.9 < p_T < 2.1 GeV/c range, after the subtraction of the pQCD contribution. Notably, models that postulate the formation

of a Quark-Gluon Plasma (QGP) were observed to be in agreement with the measurements, considering the associated uncertainties.

1.7 Event by event fluctuations at LHC

In heavy ion collisions, event-by-event measurements play a crucial role in understanding the high-energy nuclear interaction dynamics and the quark-gluon plasma (QGP) properties. In heavy ion physics, an event is essentially the single interaction between two heavy ions like Lead or Xenon (nuclei) at extremely high energies. About 10^4 particles are produced per event in collisions at the LHC. This number is large enough to analyse the desirable physical quantity on an event-by-event basis. The event-by-event analysis of observables gives more insight into the physics mechanism when compared to studying the observable as a whole. There are different aspects of the significance of event-by-event fluctuation studies, which are described below.

1.7.1 Fluctuation and Correlation Studies

Correlations and fluctuations measures inherently encapsulate the characteristics of all particles within a single event. Correlations involve the relationships among various particles arising from the same event. An introduction to correlation observables can be found in [57] and [58]. Fluctuation measures are usually based on entire events and quantify variations from one event to another. Mostly, observables involved in fluctuation analysis are impacted by particle correlations, and they may even be derived from measuring correlations, such as those between all pairs of particles within a single event.

The fluctuations can be classified into two parts. The statistical and the dynamical fluctuations. The statistical fluctuations arise because of the finite event multiplicity in the process of measurement which are basically trivial fluctuations and the dynamical fluctuations reflect the underlying dynamics of the system, containing relevant information about the properties of

system. [59, 60]. Within the collisions, fluctuations may also help understand the relevant degrees of freedom. It decides if the nucleonic scattering scenario can be explained by the initial state of the collisions or the sub-nuclear partonic structure [61, 62]. The trivial fluctuations lack information about the system and can distort signals from dynamical fluctuations, necessitating their subtraction from the measurement.

The volume of the system created from a heavy-ion collision is contingent upon the impact parameter, which varies from event to event. Consequently, fluctuation measurements of extensive quantities, are affected by volume fluctuations. These fluctuations can distort the dynamical fluctuations that carry essential information about the system. The dependence on volume is eliminated in the ratios of any two extensive quantities. Such a ratio is referred to as an "intensive quantity" [59]. The mean transverse momentum($\langle p_{\mathrm{T}} \rangle$) is expressed as the ratio of two extensive quantities: the sum of transverse momenta of charged particles and the number of charged particles, as detailed in section 3.4. Consequently, $\langle p_{\mathrm{T}} \rangle$ represents an intensive quantity, offering the advantage of being independent of the system's volume making it suitable for the event-by-event analysis. The detailed description of the observable under study is described in the following section.

1.7.2 Statistical moments

The relevant concepts of moments in statistics are discussed in this subsection. Let an event with N number of final-state particles be considered and Y be an observable of interest, which sums over the properties y_i of all N particles in the event. So, Y is defined as,

$$Y = \sum_{i=1}^{N} y_i. \tag{1.10}$$

In the context of event by event analyses, Y can be total number of charged particles, N_{ch} where y_i is 1 for charged particles and 0 for neutral particles. Alternatively, Y can be the sum of transverse momenta of all charged particles with each having value $p_{\mathrm{T,i}}$. The observable Y is expected to fluctuate on an event-by-event basis, which would result in a distribution of Y for all events. In statistics, these distributions are characterised by the moments of distribution. The

a-th moment of Y is given by,

$$A_a(Y) = \langle Y^a \rangle = \frac{1}{n_{\rm ev}} \sum_{k=1}^{n_{ev}} Y_k^a, \tag{1.11}$$

and the b-th central moment of Y is given by,

$$B_b(Y) = \langle (Y - \langle Y \rangle)^b \rangle = \frac{1}{n_{\rm ev}} \sum_{k=1}^{n_{ev}} \langle (Y_k - \langle Y \rangle)^b \rangle. \tag{1.12}$$

Here, $n_{\rm ev}$ is the total number of events.

The first moment of a distribution corresponds to mean of the distribution, which is given by,

$$M(Y) = \langle Y \rangle = \frac{1}{n_{\rm ev}} \sum_{k=1}^{n_{ev}} Y_k. \tag{1.13}$$

The difference of Y in a single event k with respect to the mean of total events is given by the first central moment,

$$\delta Y_k = Y_k - \langle Y \rangle. \tag{1.14}$$

However, by construction, $\langle \delta Y_k \rangle = 0$, which is not useful in getting an insight on the width or spread of Y distribution. Thus, the spread is described by the average of the squares of deviations from the mean, which is the second central moment of Y distribution and also called as variance. The variance is given by,

$$\sigma^2(Y) = \langle \delta Y^2 \rangle = \langle (Y - \langle Y \rangle)^2 \rangle = \langle Y^2 \rangle - \langle Y \rangle^2, \tag{1.15}$$

where, $\sigma(Y)$ is the standard deviation of the distribution and is given by the square root of the variance. For the thermal system created in a heavy-ion collisions, the distribution of a fluctuating $\langle Y \rangle$ is expected to follow a be a normal distribution, with mean zero and the standard deviation one. However, the distribution of the observable can show deviations from a normal distribution. These deviations are explained by higher moments of a normal distribution, which are the third central moment, skewness and the fourth central moment, kurtosis.

The above described moments are defined only for the distribution of a single observable, Y. Let a second observable, Z be considered such that for each event one obtains a pair (Y_k, Z_k).

One can obtain the correlation of these observables via the covariance, which is given by,

$$cov(Y,Z) = \frac{1}{n_{\rm ev}} \sum_{k=1}^{n_{ev}} (Y_k - \langle Y \rangle) \times (Z_k - \langle Z \rangle) = \langle YZ \rangle - \langle Y \rangle \langle Z \rangle. \tag{1.16}$$

If Y value tends to go along with the Z value, then covariance is positive and if Y and Z are anti-correlated, the covariance is negative. If the observables are uncorrelated, the covariance will be zero. As an example, in the later chapters of this thesis, it is shown that the covariance between mean transverse momentum per event and charged-particle multiplicity is positive.

1.7.3 The experimental observable

Nominally, studies of average $p_{\rm T}$ fluctuations are carried out based on the integral correlator $\langle \Delta p_{\rm T,1} \Delta p_{\rm T,2} \rangle$ [63–65] which is defined according to

$$\langle \Delta p_{\rm T,1} \Delta p_{\rm T,2} \rangle \equiv \frac{\int \Delta p_{\rm T,1} \Delta p_{\rm T,2} \rho_2(p_{\rm T,1}, p_{\rm T,2}) {\rm d}p_{\rm T,1} p_{\rm T,2}}{\int \rho_2(p_{\rm T,1}, p_{\rm T,2}) {\rm d}p_{\rm T,1} p_{\rm T,2}}, \tag{1.17}$$

where $\rho_2(p_{\rm T,1}, p_{\rm T,2})$ represents a two-particle particle density expressed as a function of the transverse momenta $p_{\rm T,1}$ and $p_{\rm T,2}$ of two particles, whereas $\Delta p_{\rm T,i} = p_{\rm T,i} - \langle p_{\rm T} \rangle$, $i = 1, 2$, represents transverse momentum deviation of particles 1 and 2, of a given pair, relative to the inclusive average $\langle p_{\rm T} \rangle$ defined according to

$$\langle p_{\rm T} \rangle \equiv \frac{\int \rho_1(p_{\rm T}) p_{\rm T} {\rm d}p_{\rm T}}{\int \rho_1(p_{\rm T}) {\rm d}p_{\rm T}}, \tag{1.18}$$

in which $\rho_1(p_{\rm T})$ is the inclusive single-particle density.

In this thesis, measurements of $\langle \Delta p_{\rm T,1} \Delta p_{\rm T,2} \rangle$ are obtained based on an event-wise statistical estimator defined as

$$\langle \Delta p_{\rm T,1} \Delta p_{\rm T,2} \rangle = \left\langle \frac{\sum_{i \neq j=1}^{N_{\rm ch}} (p_{{\rm T},i} - \langle p_{\rm T} \rangle)(p_{{\rm T},j} - \langle p_{\rm T} \rangle)}{N_{\rm ch}(N_{\rm ch} - 1)} \right\rangle, \tag{1.19}$$

in which the sum spans all pairs of particles formed based on the $N_{\rm ch}$ selected charged particles of a given event. The quantities $p_{{\rm T},i}$ and $p_{{\rm T},j}$, with $i \neq j = 1$, represent the transverse momenta of particles $i = 1, \ldots, N_{\rm ch}$ and $j = 1, \ldots, N_{\rm ch}$ of all $N_{\rm ch}$ selected particles of a given event. The particle selection is based on transverse momenta, $p_{\rm T}$, and pseudorapidity, η, boundaries

discussed in the following. The quantity $\langle p_{\mathrm{T}} \rangle$ is the event-wise average of the p_{T} of N_{ch} selected particles of the given event. It is computed according to

$$\langle p_{\mathrm{T}} \rangle = \frac{\sum_{i=1}^{N_{\mathrm{ch}}} p_{\mathrm{Ti}}}{N_{\mathrm{ch}}}, \tag{1.20}$$

where p_{Ti} is the transverse momenta of the i^{th} particle of a given event.

The average is said to be an event-wise average because the sum of the product of deviation is divided by the number of pairs of particles in each event. The angle brackets, $\langle O \rangle$, represent the average of the event-wise observable O computed over an event ensemble of interest. In this analysis, averages were computed for minimum bias event samples, selected fractions of the events based on their charge particle multiplicity captured in a forward detector (see below for details), and for event subsets (measured in pp collisions) selected based on a measurement of their transverse spherocity, defined and described in the upcoming chapter about the analysis details.

Computationally, it is advantageous to reformulate the analysis of $\langle \Delta p_{\mathrm{T},1} \Delta p_{\mathrm{Tj},2} \rangle$ with the introduction of an event-wise variable Q_n defined according to

$$Q_{\mathrm{n}} = \sum_{i=1}^{N_{\mathrm{ch}}} (p_{\mathrm{T,i}})^n, \tag{1.21}$$

where $p_{\mathrm{T,i}}$represents the transverse momentum of particles, $i = 1, \ldots, N_{\mathrm{ch}}$, selected towards the measurements of $\langle \Delta p_{\mathrm{T},1} \Delta p_{\mathrm{T},2} \rangle$ and N_{ch} is the number of such selected charged particles in an event. One verifies that $\langle \Delta p_{\mathrm{T},1} \Delta p_{\mathrm{T},2} \rangle$ can be readily computed according to [66],

$$\langle \Delta p_{\mathrm{T},1} \Delta p_{\mathrm{T},2} \rangle = \left\langle \frac{(Q_1)^2 - Q_2}{N_{\mathrm{ch}}(N_{\mathrm{ch}} - 1)} \right\rangle - \left\langle \frac{Q_1}{N_{\mathrm{ch}}} \right\rangle^2. \tag{1.22}$$

This implementation of the analysis presents the significant advantage that it does not involve nested loops on pairs of particles. Indeed, only single loops are required for the event-by-event determination of Q_1 and Q_2. The analysis is thus compact and fast. Additionally, in order to study the particle density dependence of the correlator and minimize smearing effects associated with broad bin widths, the analysis is first performed in narrow multiplicity bins and values of the correlator measured within these are averaged (weighted) to obtain values reported for the wide multiplicity bins reported in this thesis.

In the absence of particle correlations, i.e., for purely Poissonian fluctuations of the event-wise $\langle p_{\mathrm{T}} \rangle$, the correlator $\langle \Delta p_{\mathrm{T},1} \Delta p_{\mathrm{T},2} \rangle$ vanishes. However, it acquires a finite value, either positive or negative, when the transverse momenta of produced particles of a given collision are correlated. Note that both the numerator and the denominator of $\langle \Delta p_{\mathrm{T},1} \Delta p_{\mathrm{T},2} \rangle$ are proportional to the square of the particle detection efficiency making $\langle \Delta p_{\mathrm{T},1} \Delta p_{\mathrm{T},2} \rangle$ robust against particle losses, i.e. efficiencies approximately cancel out in measurements of $\langle \Delta p_{\mathrm{T},1} \Delta p_{\mathrm{T},2} \rangle$. While the cancellation is not perfect, particularly if the detection efficiency depends on the p_{T} of particles, such effects were found to be rather small in the analysis reported in this thesis.

The $\langle \Delta p_{\mathrm{T},1} \Delta p_{\mathrm{T},2} \rangle$ correlator measures particle transverse momentum correlations. In heavy-ion collisions, A–A, the mean transverse momentum is known to depend on collective effects and more particularly, radial flow. One thus expects $\langle \Delta p_{\mathrm{T},1} \Delta p_{\mathrm{T},2} \rangle$, which involves a “trivial" dependence on the magnitude of this flow. This trivial dependence can be largely suppressed by formulating the results in terms of the dimensionless quantity $\sqrt{\langle \Delta p_{\mathrm{T},1} \Delta p_{\mathrm{T},2} \rangle} / \langle \langle p_{\mathrm{T}} \rangle \rangle$. The use of a dimensionless observable features a number of additional advantages: independence from uncertainties on the momentum scale, partial independence from the magnitude of $\langle p_{\mathrm{T}} \rangle$, and further reduction of sensitivity to the dependence of the particle detection and reconstruction efficiency on the transverse momentum. The dimensionless quantity $\sqrt{\langle \Delta p_{\mathrm{T},1} \Delta p_{\mathrm{T},2} \rangle} / \langle \langle p_{\mathrm{T}} \rangle \rangle$ is thus reported in this thesis in lieu of $\langle \Delta p_{\mathrm{T},1} \Delta p_{\mathrm{T},2} \rangle$.

1.7.4 Temperature fluctuations

Given that the collision between two heavy ion nuclei produces a large number of particles per event, giving rise to an approximate state of thermal equilibrium reaching a particular temperature "T" which remains constant [67]. In the context of heavy-ion collisions, the analysis is often limited to a subsystem, primarily due to constraints related to the measurement being confined to the (pseudo-)rapidity range of the detectors. Consequently, this subsystem becomes integrated into the heat bath of the entire system, enabling the exchange of energy and particles with the larger system. As a result, the grand-canonical ensemble is commonly used to describe the considered system.

In the grand-canonical ensemble, a system is defined by the pressure P(T, V, μ_b), where the pressure depends on the temperature (T), volume (V), and chemical potentials (μ_b) of the system. These chemical potentials, namely μ_b (baryon number), μ_Q (electric charge), and μ_S (strangeness), ensure the conservation of essential charges in the entire system. This conservation is crucial in the context of strongly interacting matter generated in heavy-ion collisions [68]. Study of the fluctuation of these conserved charges and temperature can impart the properties of the QGP on an event-by-event basis.

Now, having got the equilibrated temperature of a system, it is meaningful, to investigate temperature fluctuations. The dispersion in the temperature can be found by averaging over several events. This can be reflected in the equation:

$$(\Delta T)^2 = \overline{(T - \overline{T})^2} \tag{1.23}$$

And heat capacity of a system is related to the temperature fluctuation (ref) as,

$$C^{-1} = \frac{(\Delta T)^2}{T^2} \tag{1.24}$$

The heat capacity of a system gives considerable information about its thermodynamics properties. Irregularity seen in heat capacity is a characteristic of phase transition. As discussed in Sec. 1.4, the location and properties of these phase transitions are not exactly known. During phase transition, especially in the vicinity of the probable critical endpoint, the fluctuation signals are expected to be largely influenced and can show irregular behaviour [25, 26, 59, 60]. Hence, studying the temperature fluctuations, which are related to the heat capacity of the system can throw insights into the phase transition and critical end point. To probe the QCD phase diagram and understand the dynamics of the phase transition, event-by-event fluctuations of global observables like mean transverse momentum which acts like a proxy for the temperature of the system, conserved quantities like net-charge, net-baryon, net-strangeness and identified particle ratios in the hadronic final state are studied.

1.8 Previous experimental observation

Various measurements of event-by-event fluctuations of different observables have been performed in different experiments giving rise to interesting results. This section focuses on the comprehensive examination of the literature pertaining to $\langle p_{\mathrm{T}} \rangle$ fluctuation measurement that has been the motivation to delve deeper into the study of the related observable.

Previous measurements of event-by-event fluctuations of $\langle p_{\mathrm{T}} \rangle$ have been studied in nucleus-nucleus (A–A) collisions at different colliders like the Super Proton Synchrotron (SPS) [69–73] and at the Relativistic Heavy-Ion Collider (RHIC) [74–79] . The relative dynamical fluctuations have also been studied for pp and Pb–Pb collisions as a function of charged particle multiplicity for different collision energies with ALICE at the LHC. The results showed decreasing $\langle p_{\mathrm{T}} \rangle$ fluctuations with collision centrality, as generally expected in a dilution scenario caused by the superposition of partially independent particle-emitting sources.

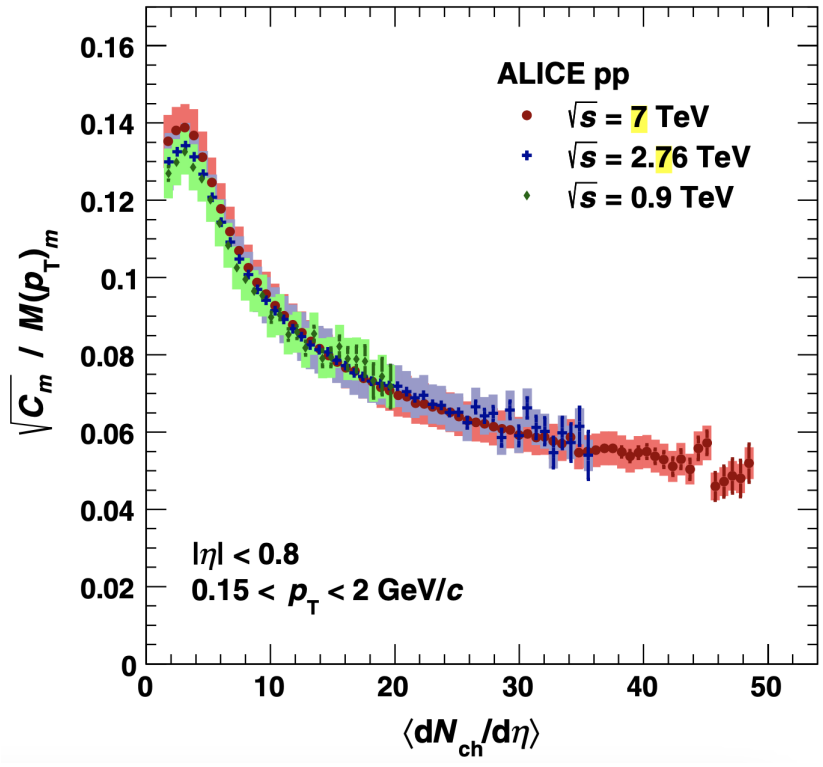

Figure 1.19: Relative fluctuation of $\sqrt{C_m}/M(p_{\mathrm{T}})$ as a function of $\langle \mathrm{d}N_{\mathrm{ch}}/\mathrm{d}\eta \rangle$ in pp collisions at $\sqrt{s}$ = 0.9, 2.76 and 7 TeV

In a more detailed analysis, deviation from a simple superposition scenario has been studied and reported. Specifically, concerning a reference scenario that assumes independent superposition – where fluctuations decrease according to $\langle dN_{ch}/d\eta \rangle^{-0.5}$, with $\langle dN_{ch}/d\eta \rangle$ representing the average charged-particle density within a specific range of collision centrality and pseudorapidity (η) – it has been observed that fluctuations increase notably as collisions progress from peripheral to semi-peripheral configurations. Subsequently, there is a gradual reduction in fluctuations as collisions become more central [80]. Several possible mechanisms have been proposed to elucidate this phenomenon, including string percolation [81] or the emergence of thermalization and collectivity [65, 82]. However, no conclusive link to critical behavior has been established. Recent suggestions [83] propose that fluctuations in the initial state density [84] could influence the final state correlations in transverse momentum and their dependence on collision centrality.

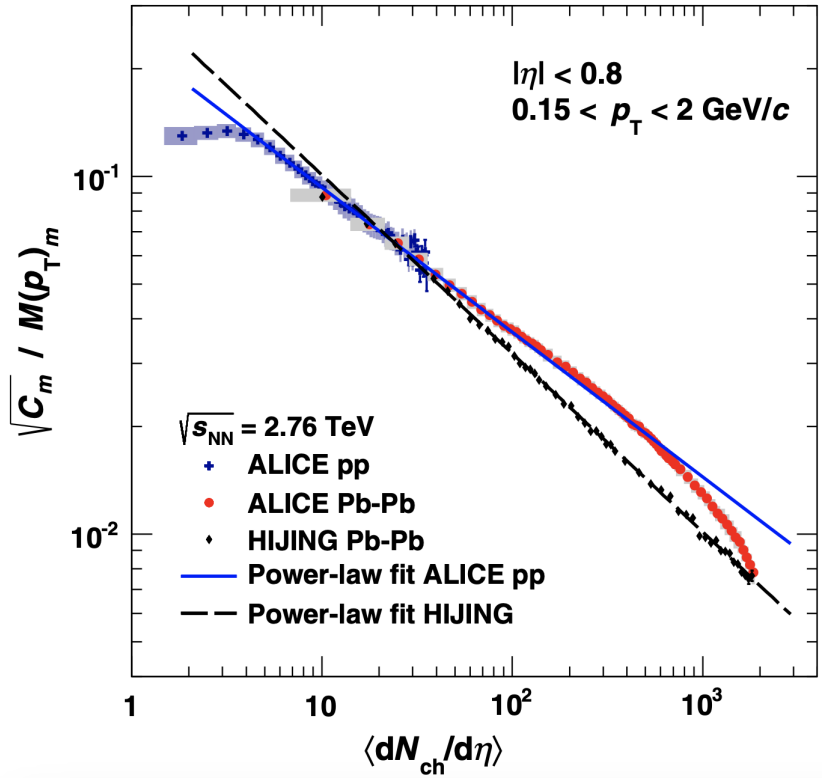

Figure 1.20: Relative dynamical fluctuation $\sqrt{C_m}/M(p_T)$ as a function of $\langle dN_{ch}/d\eta \rangle$ in pp and Pb–Pb collision at $\sqrt{s_{NN}}$ = 2.76 TeV. Also shown are results from HIJING and power-law fits to pp (solid line) and HIJING (dashed line)

Fig. 1.19 shows $\sqrt{C_m}/M(p_T)$ ($\sqrt{\langle \Delta p_{T,1} \Delta p_{T,2} \rangle}/\langle\langle p_T \rangle\rangle$) as a function of $\langle dN_{ch}/d\eta \rangle$ in pp collisions at $\sqrt{s}$ = 0.9, 2.76 and 7 TeV as measured in [85]. Significant dynamical event-by-event $\langle p_T \rangle$ fluctuations were observed as indicated by the non-zero values of $\sqrt{C_m}/M(p_T)$. Similarly Fig. 1.20 shows $\sqrt{C_m}/M(p_T)$ as a function of $\langle dN_{ch}/d\eta \rangle$ in pp and Pb–Pb collision at $\sqrt{s_{NN}}$ = 2.76 TeV. This figure also shows the HIJING [86](version 1.36) comparison without jet-quenching with the real data. A deviation from a simple superposition scenario i.e. HIJING, was reported. To be specific, a decrease of fluctuations according to $\langle dN_{ch}/d\eta \rangle^{-0.5}$ and pseudo-rapidity (η) in a given interval of collision centrality was observed with respect to a reference representing independent superposition. However, the observed fluctuations increase sharply from peripheral to semi-peripheral collisions, followed by a shallow decrease towards high multiplicity regions [80, 87]. To see if mechanisms such as string percolation [81], the onset of thermalization and collectivity [65] might explain such behaviour, further study of system size and energy scan is an interesting approach to further study this observable. Also, the deviation of the observable from an effect of simple superposition of particle emitting sources, and the higher value of the observable suggests a deviation from the idea of the suppression of jets at the high multiplicity region which in turn encouraged to study this observable using different classes of spherocity that could help separate the jetty and isotropic events and study of such an observable in more depth and better understanding.

Fig. 1.21 shows $\sqrt{\langle \Delta p_{T,i} \Delta p_{T,j} \rangle}/\langle\langle p_T \rangle\rangle$ for $\sqrt{s_{NN}}$ at 7.7 and 200 GeV for Au+Au collisions. These results are compared with similar results from the ALICE experiment for Pb+Pb collisions at $\sqrt{s_{NN}}$ = 2.76 TeV [85] discussed earlier. The results obtained from Au+Au collisions at $\sqrt{s_{NN}}$ = 200 GeV demonstrate a strong agreement with those from Pb+Pb collisions at $\sqrt{s_{NN}}$ = 2.76 TeV. To illustrate this, a dashed line (of the form $22.32\%/\sqrt{N_{part}}$) representing a power-law fit to the STAR Au+Au data at $\sqrt{s_{NN}}$ = 200 GeV has been shown. This same fit effectively reproduces the results observed in Pb–Pb collisions at $\sqrt{s_{NN}}$ = 2.76 TeV, with the exception of the most central collisions where a deviation is observed. However, as the collision energy decreases (7.7 GeV/c), a deviation from this power-law scaling is evident in the relative dynamical correlation as a function of N_{part}.

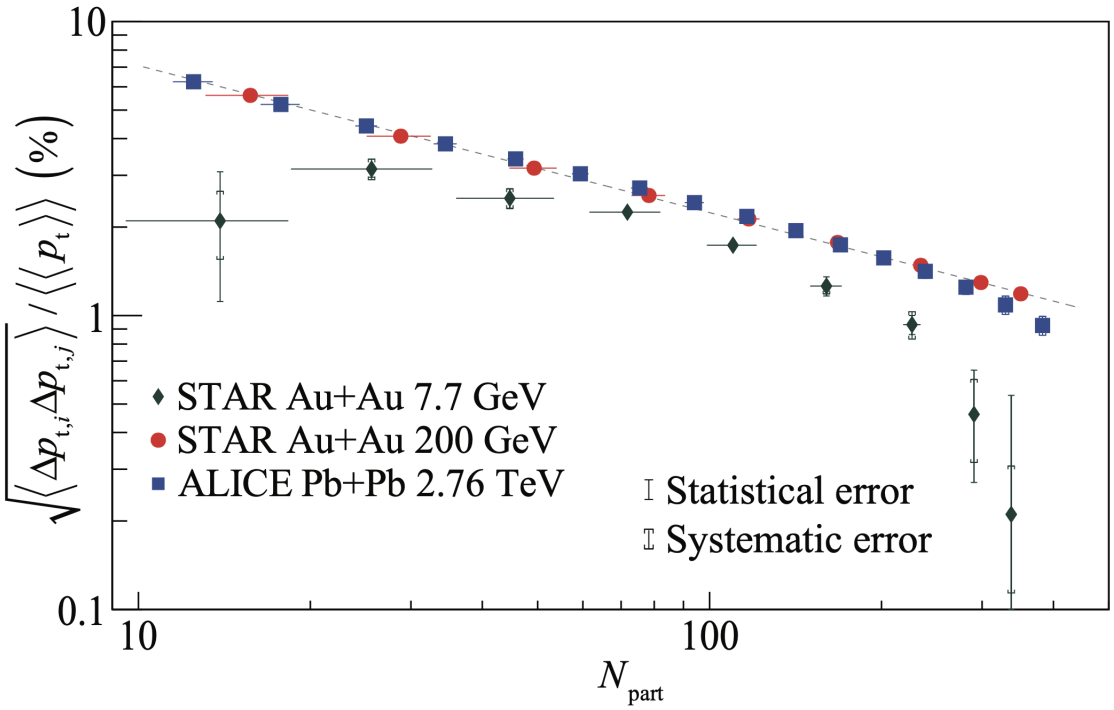

Figure 1.21: The relative dynamical correlation $\sqrt{\langle \Delta p_{\mathrm{T},i} \Delta p_{\mathrm{T},j} \rangle} / \langle \langle p_{\mathrm{T}} \rangle \rangle$ for $\sqrt{s_{NN}}$ = 7.7 GeV and 200 GeV Au+Au collisions compared with similar results from Pb+Pb collisions at $\sqrt{s_{NN}}$ = 2.76 TeV. The dashed line represents a fit the to data at $\sqrt{s_{NN}}$ = 200 GeV given by $22.32\%/\sqrt{N_{\text{part}}}$. Statistical and systematic errors are shown [88].

From fig. 1.20 and fig. 1.21, a deviation of the two-particle correlators from the simple superposition scenario has been observed at a high multiplicity region for heavy ion collisions. This deviation primarily manifests in a decreasing pattern. In central collisions, which correspond to high multiplicity events, the quenching of jets or particles with high momentum transfer(Q^2), becomes relevant. Therefore, the underlying cause for the reduced strength of the correlator in high multiplicity events could be attributed to factors such as jet quenching or radial flow, among others. Investigating this behavior in more detail by analyzing different event types holds particular interest.

In the realm of hadron-hadron collisions, one of the prevailing effects that significantly shapes the final state kinematics involves low momentum transfer (Q^2) interactions between incoming partons. For many researchers, these interactions may appear to be of limited interest and are often regarded as background noise requiring elimination when searching for new

physics. Perturbative Quantum Chromodynamics (QCD) offers a robust foundation for comprehending particle production at high momentum transfers, particularly in the context of jets, where much of the physics beyond the Standard Model is expected to manifest. Unfortunately, the applicability of these calculations diminishes as we venture into the domain of low Q^2. This is primarily due to the escalating complexity of the theoretical framework. Consequently, researchers frequently turn to phenomenological models within Monte Carlo event generators to simulate the intricate evolution of partons in this regime.

Up to this point, event shape observables have been investigated as a method for disentangling one or multiple hard scatterings from underlying events. These underlying events are primarily characterized by soft QCD interactions, although they can, in some cases, also involve hard processes. Recently, intriguing signs of collective-like phenomena have emerged in the multiplicity-dependent yields of hadrons in proton-proton (pp) collisions. These observations bear a qualitative resemblance to those previously noted in proton-lead (p-Pb) and lead-lead (Pb–Pb) collisions [89].

Typically, the manifestations of collectivity are most pronounced within the soft QCD domain. Consequently, event-shape observables offer a promising avenue to gain a deeper understanding of the fundamental physics underlying pp collisions, especially when it comes to unravelling the intricacies of collectivity effects. Event shape variables are perhaps the most popular observables to improve our understanding of the dynamics of quantum chromodynamics (QCD). In the late 1970s, event shape observables became an important tool to study the nature of gluon bremsstrahlung [90]. Event shape observables have the capability to distinguish the collisions based on their geometrical shapes and they can measure the extent of energy flow departs from a dijet structure in an event.

While various approaches exist for constructing different event shape observables [90], their common objective is to depict how energy is distributed, particularly in the transverse plane, within the final state of a collision. As a consequence of multiple low momentum transfer (Q^2) scatterings, underlying events typically display a uniform azimuthal angular distribution of final state hadrons, in contrast to the tightly collimated jets. From an experimental standpoint,

this translates to events primarily influenced by minor momentum transfers having isotropic angular distributions and an abundance of low-p_{T} particles. Conversely, events predominantly driven by a single high-energy scattering event exhibit most hadrons aligned along a single axis (manifesting as a back-to-back jet structure) and possess harder p_{T} spectra.

The event shape is quantified using transverse spherocity (S_0), is expressed as,

$$S_0 = \frac{\pi^2}{4} \min_{\hat{n}=(n_x,n_y,0)} \left(\frac{\sum_{i=1} \hat{p}_{\mathrm{T_i}} \times \hat{n}}{\sum_{i=1} \hat{p}_{\mathrm{T_i}}} \right)^2, \tag{1.25}$$

Here, $\hat{n}$ represents a two-dimensional unit vector within the transverse plane, carefully selected to minimize the transverse spherocity (S_0). In practical terms, this vector typically aligns with one of the transverse momentum vectors, denoted as $\hat{p_{\mathrm{T}}}$. By design, it exhibits two distinct limits. In the context of this parameterization, $S_0 = 0$ corresponds to the scenario characterized as the "jetty limit," whereas $S_0 = 1$ represents the "isotropic limit".

Figure 1.22 illustrates the variation of the spherocity-integrated average transverse momentum $\langle p_{\mathrm{T}} \rangle$ as a function of the particle pseudorapidity density $\langle \mathrm{d}N_{\mathrm{ch}}/\mathrm{d}\eta \rangle$ for proton-proton (pp) collisions at $\sqrt{s} = 13$ TeV. In line with measurements at lower energy levels [91], $\langle p_{\mathrm{T}} \rangle$ demonstrates an increasing trend with an increase of $\langle \mathrm{d}N_{\mathrm{ch}}/\mathrm{d}\eta \rangle$. The data obtained for minimum-bias events are juxtaposed with similar measurements for two distinct event categories: the most jet-like events (0 – 10%) and isotropic events (90 – 100%). Investigating observables as a function of spherocity unveils intriguing features. For isotropic events, $\langle p_{\mathrm{T}} \rangle$ consistently remains below the spherocity-integrated $\langle p_{\mathrm{T}} \rangle$ across the entire multiplicity range. While for jet-like events, $\langle p_{\mathrm{T}} \rangle$ exceeds that of spherocity-integrated events. Furthermore, it is noteworthy that, within the bounds of uncertainties, the overall correlation shape remains consistent, characterized by a steep linear increase below $\langle \mathrm{d}N_{\mathrm{ch}}/\mathrm{d}\eta \rangle = 10$, followed by a somewhat less pronounced but still linear rise above this threshold, and this behaviour is independent of spherocity.

Now Jetty events exhibiting larger $\langle p_{\mathrm{T}} \rangle$ than isotropic events, is a matter of interest which is of particular significance. This investigation aims to shed light on the underlying factors contributing to the observed decline in the p_{T} correlations, as exemplified in the case of Pb–Pb collisions [85]. This decline was noted when compared with the simple nucleon-nucleon

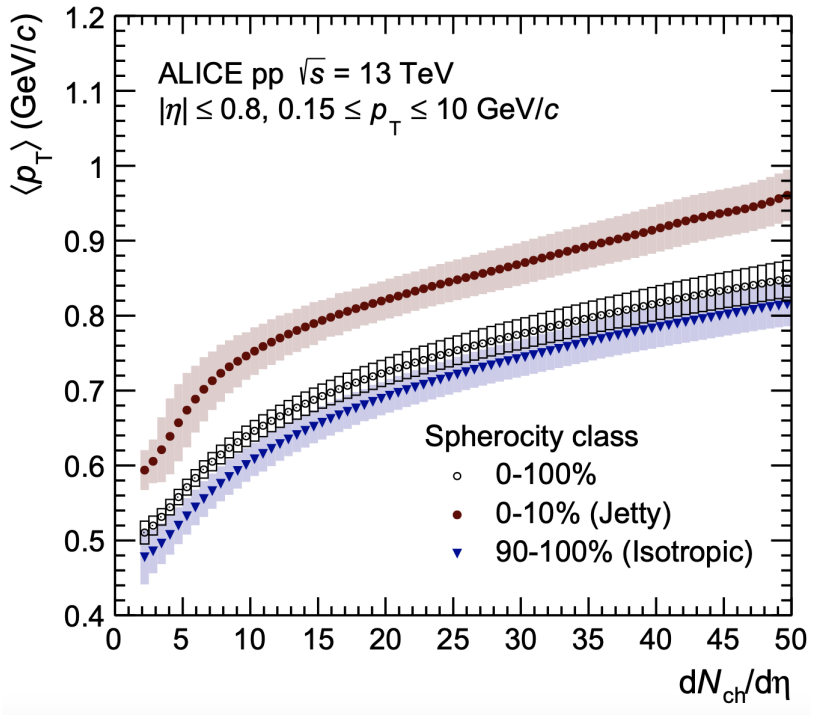

Figure 1.22: Mean transverse momentum as a function of event multiplicity in pp collisions at $\sqrt{s}$ = 13 TeV. Results for the spherocity-integrated case (0 – 100%) are contrasted with the measurements for jetty (0 – 10%) and isotropic (90 – 100%) events. While statistical uncertainties (represented by error bars) are minimal, systematic uncertainties are more prominent and are denoted by boxes surrounding the data points.

collisions that lacked rescattering effects. This thesis delves into this study, presenting intriguing findings.

1.9 Scope of the thesis

- **Chapter 1** gives a general introduction to the standard model and QCD followed by a brief discussion on QGP and its indirect signatures. Discussion on the LHC's "Little Bang", the geometry of heavy-ion collisions and kinematic variables is carried out, followed by the discussions on possible signatures of QGP. It finally delves into a literature review of fluctuation analyses, which will shed light on the motivation behind the work on event-by-event fluctuations of mean transverse momentum, its energy and system size scan.

- **Chapter 2** gives an overview of the CERN-LHC accelerator system, ALICE experiment and a brief description of different sub-detectors.

- **Chapter 3** is devoted to the detailed analysis methodology of event-by-event fluctuation analyses in pp, Xe–Xe and Pb–Pb collisions.

- **Chapter 4** discusses the main experimental results of the thesis.

- **Chapter 5** summarises the studies in the thesis that have been presented and a brief outlook is also presented.

Chapter 2

ALICE: A Large Ion Collider Experiment at the LHC

2.1 Introduction

One of the four main detectors at the Large Hadron Collider (LHC) at CERN in Switzerland is the ALICE detector. The main objective of ALICE is to learn more about the properties of the QGP, a state of matter that is considered to have existed in the first few microseconds after the Big Bang. In the LHC, heavy ions like lead (Pb) and Xenon (Xe) are made to collide at extremely high energies to produce the QGP in the laboratory.

This chapter briefly describes the LHC and different sub-detectors of ALICE.

2.2 LHC

The Large Hadron Collider (LHC) [92] (see figure 2.1), is a particle accelerator which is situated at the European Organization for Nuclear Research (CERN) in Switzerland. LHC is the largest and most powerful particle accelerator in the world. It is a ring-shaped tunnel with a circumference of 27 km and is located 100 meters (328 feet) beneath the Swiss and French border. It is designed to accelerate proton beams with a maximum energy of 13 TeV with a peak luminosity of 30 pb^{-1} for pp collisions and a maximum energy of 5.02 TeV with a peak

luminosity of 800 mb^{-1} for Pb–Pb collisions for the year 2015-2018 [93] within ALICE. The schematic is shown in Fig. 2.1

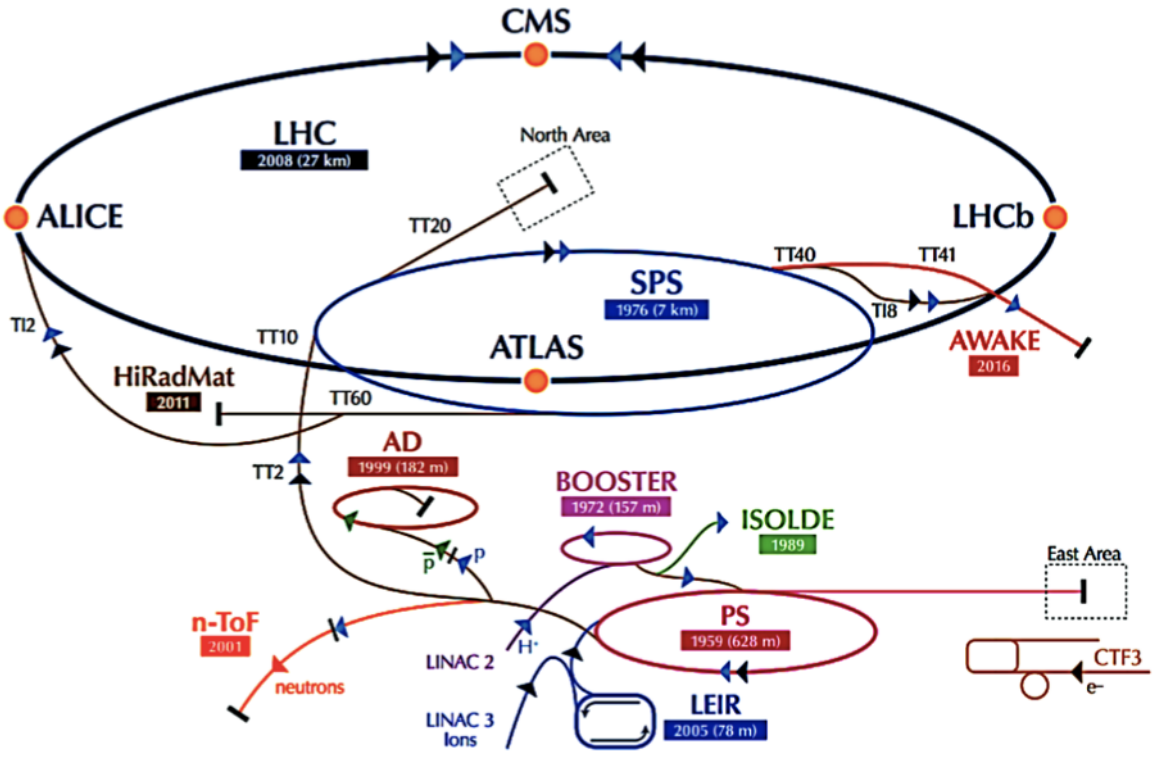

Figure 2.1: A schematic diagram of CERN's accelerator complex [92].

By letting particles collide at extremely high velocities, the LHC enables researchers to better understand the origin of matter and energy. Protons are obtained by stripping electrons from hydrogen atoms. These protons undergo acceleration in Linear Accelerator, LINAC 2, initially reaching an energy of 50 MeV. The protons then enter the Proton Synchrotron Booster, PSB and are further accelerated to 1.4 GeV within the PSB. Protons are injected into the Proton Synchrotron (PS) and undergo acceleration within the PS to reach energies of 25 GeV. The proton beams are further injected into Super Proton Synchrotron (SPS) where they are further accelerated to an impressive 450 GeV. Subsequently, these accelerated beams are injected into both the LHC rings through the transfer lines TI2 and TI8. They are made to travel in opposing directions in two vacuum pipes present in the LHC. The counter-rotating beams intersect at the four intersecting points, equipped with four detectors namely ALICE, CMS, LHCb, and ATLAS. The protons are further accelerated to attain the maximum energy of 6.8 TeV.

For accelerating lead (Pb) ions, a meticulously purified lead sample acts as a Pb ion source. It is heated to reach a temperature as high as 800^0C to generate vapours of lead atoms. These atoms undergo ionization due to electric current. Consequently, a diverse range of lead-ion charge states are produced, with the highest charge state typically reaching Pb^{29+}. Subsequently, utilizing a charge separator, these ions are carefully selected and propelled through LINAC 3, where they attain an energy of 4.2 MeV per nucleon. Thereafter, a carbon foil is employed to strip additional electrons from the lead ions forming Pb^{54+} ions. These ions are further injected into the Low Energy Ion Ring (LEIR) where they are accelerated up to 72 MeV per nucleon [94].

These accelerated Pb^{54+} ions are injected into (PS) for further acceleration to reach 5.9 GeV per nucleon. The Pb^{54+} ions are then directed through a secondary foil to completely strip away any remaining electrons, resulting in fully stripped Pb^{82+} ions. The ion beams are then transported via the transfer line TT2 to reach the SPS where they are accelerated to 177 GeV per nucleon. Subsequently, these accelerated beams are injected into both LHC rings to achieve a maximum of 2.68 TeV per nucleon.

The introduction of a pulsing electric field causes the protons and ions to be in a continuous circular motion. The protons' beam is bent around the circle by the application of strong electromagnets. These magnets are fixed in a direction that is perpendicular to the velocity of the packets. There are 1,232 dipole magnets and 392 quadrupole magnets. In total, over 1,600 superconducting magnets are installed, with most weighing over 27 tonnes. Approximately 96 tonnes of liquid helium is needed to keep the magnets, at their operating temperature of 1.9 K (271.25 C). An ultrahigh vacuum of $10^{-10} - 10^{-11}$ mbar is formed inside the beam pipes. These conditions enable a maximum of around 2808 bunches of particles to be circulated with a bunch spacing of 25 ns in each of the two rings. The maximum reaching energies of LHC are 13.6 TeV for pp collisions and 5.36 TeV for Pb-Pb collisions.

The event rate, R and the interaction cross section (σ_{int}) of the process being studied can be expressed as

$$R = L\sigma_{int} \tag{2.1}$$

where, L, is the instantaneous luminosity, an essential beam parameter after energy. The luminosity L can be expressed as,

$$L = \frac{N^2 n f \gamma}{4\pi\epsilon\beta^*} F, \tag{2.2}$$

where N and n, respectively, represent the number of particles per bunch and the number of bunches in a beam. The ϵ, f, and γ refer to normalised transverse beam emittance, revolution frequency, and gamma factor respectively. The amplitude function at the interaction point (IP) and the geometrical reduction factor that takes into account the crossing angle at the IP are β^* and F, respectively.

2.3 The ALICE detector

ALICE is one of the detectors of LHC which was designed to study the QCD matter formed in ultra-relativistic heavy ion collisions. It has a dimension of 26x16x16 m^3 detector and weighs around 10,000 tonnes [95]. It is situated in a vast cavern, 56m below the ground on the French border. ALICE consists of seventeen detector subsystems which have different acceptances serving specific physics purposes. The schematic of ALICE detector is shown in Fig. 2.2 along with the detector acceptance. The acceptance, position and main purpose of these detectors are listed in Table 2.1.

Table 2.1: Summary of ALICE sub-detector systems [96].

Detector	Acceptance (η)	Acceptance (ϕ)	Position	Purpose
SPD	±2.0	full	r = 3.9 cm	tracking, vertex
	±1.4	full	r = 7.6 cm	tracking, vertex
SDD	±0.9	full	r = 15.0 cm	tracking, PID
	±0.9	full	r = 23.9 cm	tracking, PID
SSD	±1.0	full	r = 38 cm	tracking, PID
	±1.0	full	r = 43 cm	tracking, PID
TPC	±0.9	full	$85 < r/cm < 247$	tracking, PID
TRD	±0.8	full	$290 < r/cm < 368$	tracking, $e^{\pm}$ id
TOF	±0.9	full	$370 < r/cm < 399$	PID
PHOS	±0.12	$220^0 - 320^0$	$460 < r/\text{cm} < 478$	photons
EMCal	±0.7	$80^0 - 187^0$	$430 < r/\text{cm} < 455$	photons and jets
HMPID	±0.6	$1^0 - 59^0$	r = 490 cm	PID
ACORDE	±1.3	$30^0 - 150^0$	r = 850 cm	cosmics
PMD	2.3 – 3.9	full	z = 367 cm	photons
FMD	3.6 – 5.0	full	z = 320 cm	charged particles
	1.7 – 3.7	full	z = 80 cm	charged particles
	(−3.4) – (−1.7)	full	z = −70 cm	charged particles
V0	2.8 – 5.1	full	z = 329 cm	charged particles
	(−3.7) – (−1.7)	full	z = −88 cm	charged particles
T0	4.6 – 4.9	full	z = 370 cm	time, vertex
	(−3.3) – (−3.0)	full	z = −70 cm	time, vertex
ZDC	> 8.8	full	z = ±113 m	forward neutrons
	6.5 – 7.5	$\phi < 10^0$	z = ±113 m	forward protons
	4.8 – 5.7	$2\phi < 32^0$	z = 7.3 m	photons
MCH	(−4.0−)−(−2.5)	full	$-14.2 < z/m < -5.4$	muon tracking
MTR	(−4.0) – (−2.5)	full	$-17.1 < z/m < -16.1$	muon trigger

2.4 Central barrel detectors

The central barrel of ALICE is embedded in a large solenoidal magnet (L3 magnet, taken from the LEP experiment), which provides a 0.5T magnetic field. The central barrel covers the pseudorapidity interval of -0.9 < η < 0.9 which corresponds to polar angle 45^0 - 135^0. Central barrel comprises Inner Tracking System (ITS) [97], Time Projection Chamber (TPC) [98], Time of Flight (TOF) [99] detector, Transition Radiation Detector (TRD)[100], Cherenkov counter (HMPID) [101], Photon Spectrometer (PHOS) [102], Electro-magnetic calorimeter (EMCAL) [102, 103] and the ALICE Cosmic Ray Detector (ACORDE) [102]. The central detectors are mainly used for tracking, vertex reconstruction, particle identification and measurement of track momentum.

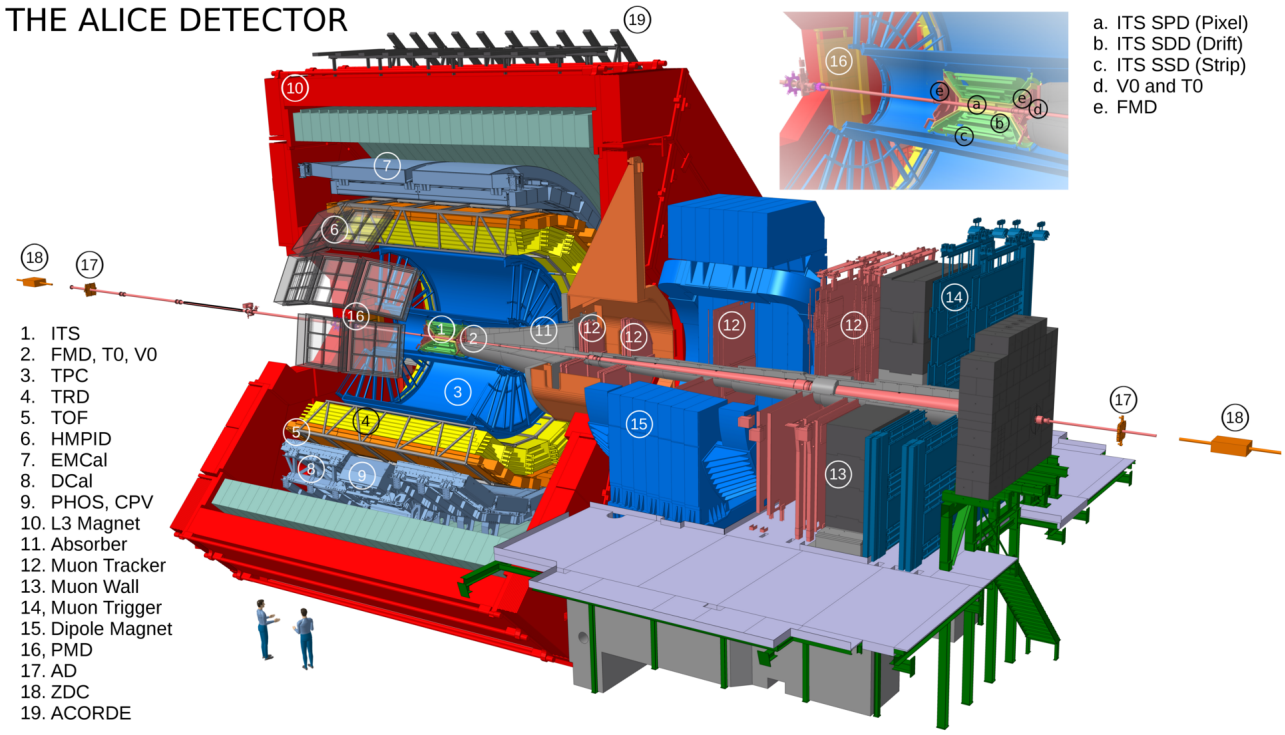

Figure 2.2: Schematic layout of ALICE detector [104].

A brief description of the central barrel detectors is discussed in the following subsections.

2.4.1 Inner Tracking System (ITS)

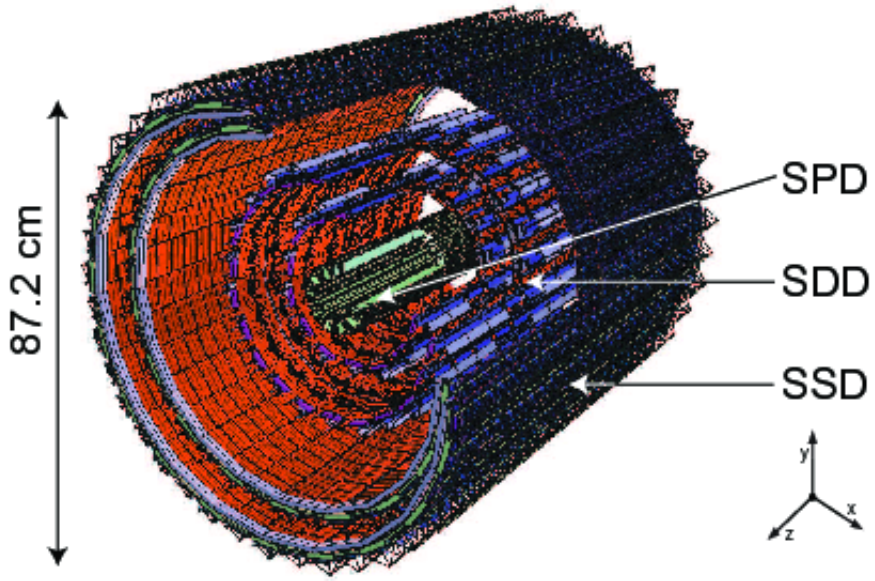

Figure 2.3: Depiction of Inner Tracking System (ITS) [97]

The Inner Tracking System (ITS) [97], comprises six cylindrical layers of silicon detectors, which are closest to the interaction point and have full azimuthal coverage. The layout of ITS is shown in Fig. 2.3. The key goal of ITS is the accurate determination of primary and secondary vertices of a collision. It also provides excellent two tracks momentum resolution along with the distance of the closest approach to the primary vertex of a collision.

The innermost detector in the ITS, Silicon Pixel Detector (SPD) plays a vital role in the accurate determination of primary and secondary vertices of a collision. SPD can withstand high radiation levels and can operate at very high track densities of about 50 tracks/cm^3. SPD consists of reverse-biased silicon detector diodes in a two-dimensional matrix and they are connected through a conductive solder bump on read-out chips which correspond to the input of readout cells. In total, it contains 1200 readout pixel chips and 107 cells. The pixel chips provide Fast-OR digital pulses when a pixel or a group of them detects a signal above a particular threshold. This makes SPD capable of acting as a prompt trigger.

The intermediate layers (3rd and 4th) of the ITS, Silicon Drift Detectors (SDD) provide very high precision position information with a resolution of about 35 μm. SDD also provides information on the energy loss, (dE/dx), which can be used for particle identification.

The outermost layer in the ITS, the Silicon Strip Detector (SSD) plays an important role in matching the tracks in ITS and the Time Projection Chamber (TPC). It provides a two-dimensional measurement of the position of tracks along with information on the specific energy loss of the particle dE/dx.

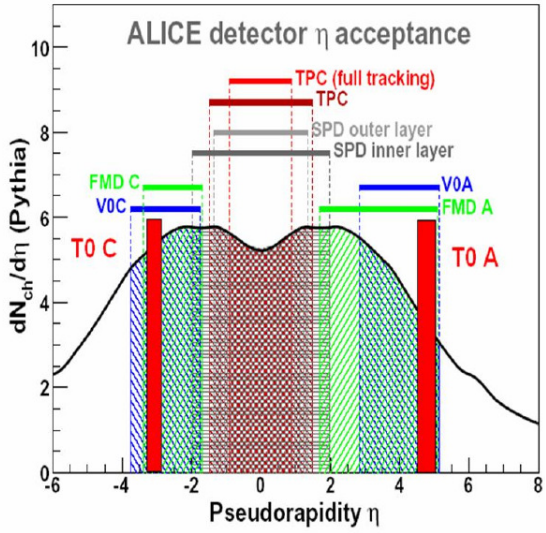

Figure 2.4: Pseudo-rapidity coverage of ALICE sub-detectors [105]

2.4.2 Time Projector Chamber (TPC)

The Time Projector Chamber (TPC) [98, 106], a cylindrical gaseous detector, is the main tracking detector of the ALICE detector system. TPC is optimised to measure the momentum of charged particles with good two-track resolution. The layout of TPC is shown in Fig. 2.5. TPC has the pseudo-rapidity coverage of $|\eta| < 0.9$ and full azimuthal coverage. It is cylindrical in shape with an inner and outer radius of 80 and 250 cm, respectively. It is filled with 90% of Ne and 10% of CO_2. At the centre, a cylindrical conducting electrode is placed to maintain a uniform electrostatic field of 400 V/cm.

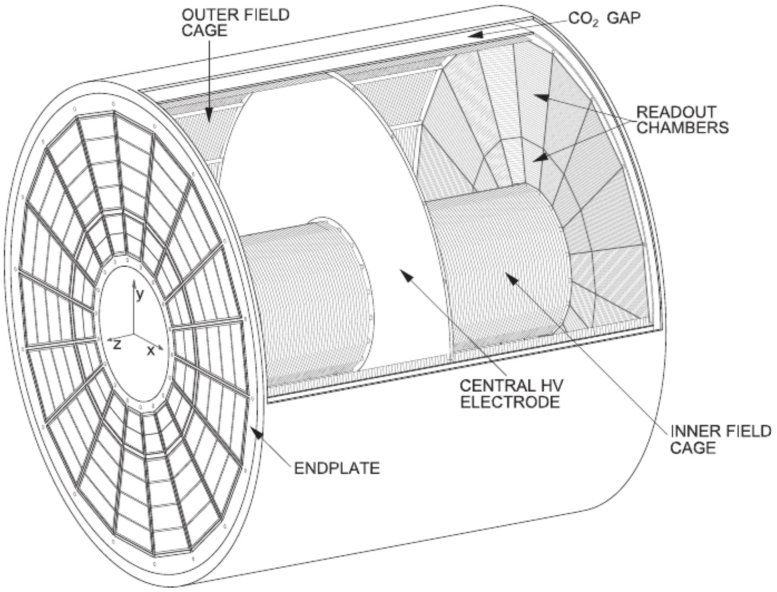

Figure 2.5: Depiction of Time Projection Chamber (TPC) [98, 106]

The working principle of TPC is shown schematically in Fig. 2.6. While a charged particle traverses through the gas mixture in the TPC, the gas atoms are excited and ionized along its path due to which the charged particle loses an amount of energy per unit track length (dE/dx) and the energy loss is different for each particle type. The free electrons from ionisation drift towards the endplates of the cylinder due to the electric field and the ions drift towards the cathode at the centre of the TPC. A magnetic field is oriented parallel to the electric field so that the drifting electrons are not affected by it. At the end of the drift path, the electron signals are amplified by an avalanche process around the anode. The Multi-Wire Proportional Chambers (MWPCs) at the end plates are used for the readout of the signal.

2.4.3 Transition Radiation Detector (TRD)

The Transition Radiation Detector [108], consists of six layers of radiators and a drift chamber, located in the radial position of 2.9 to 3.7 m from the interaction point. It has a full azimuthal coverage and pseudo-rapidity range of $-0.84 < \eta < 0.84$. TRD is instrumental in measuring electrons for $p_{\mathrm{T}} > 1$ GeV/c, where the TPC cannot identify them via the energy loss measurements. TRD helps to study the electron spectra and light/heavy vector meson

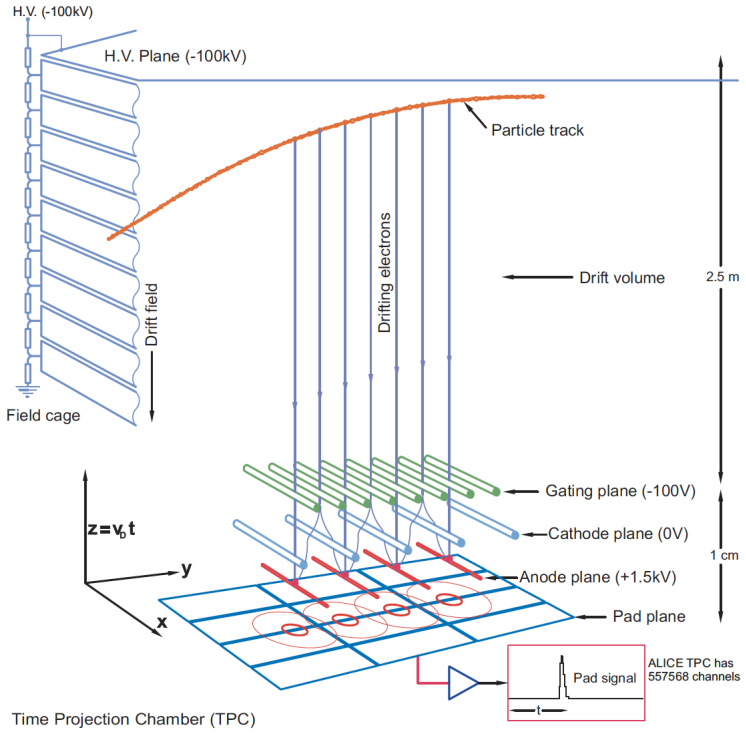

Figure 2.6: The schematic illustration of the working principle and the read-out chambers of the TPC [107].

resonances via their leptonic decay channels. Fig. 2.7 shows the cross-sectional view of a module along with the working principle of TRD [108].

2.4.4 Time Of Flight (TOF) detector

The time of flight (TOF) detector comprises Multi-gap Resistive Plate Chamber (MRPC), which is a gaseous cylindrical detector placed around the TRD within $|\eta| < 0.9$. It measures the charged particle velocity by measuring the time of flight along the track trajectory. TOF detector helps in identifying hadrons in the intermediate momentum region, where TPC is unable to identify particles by dE/dx measurement. While a charged particle traverses through the detector, it ionizes the gas and because of the high electric field, the ionization is amplified through an electron avalanche. Then the electrons are stopped due to the resistive plates. TOF detector has the ability to detect particles with a time resolution of about 85 ps for Pb–Pb and 120 ps in pp collisions with 99.9% efficiency.

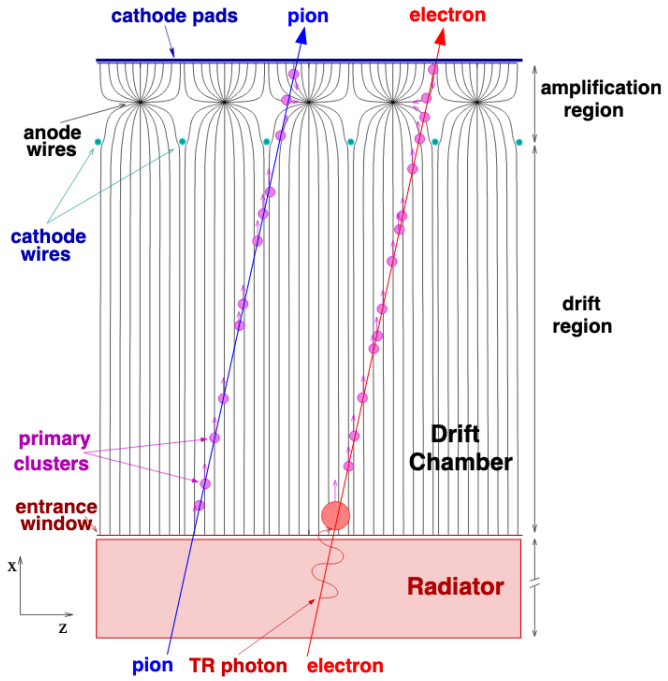

Figure 2.7: Cross-sectional view of a module along with the working principle of TRD [108]

2.4.5 High Momentum Particle Identification Detector (HMPID)

The High Momentum Particle Identification Detector (HMPID) is based on Ring Imaging Cherenkov (RICH) counters. The HMPID extends track-by-track charged hadron identification at high-p_{T} in ALICE. The momentum reach of HMPID is beyond the momentum interval achievable by ITS, TPC and TOF detectors. Electromagnetic radiation is emitted when a charged particle passes through the detector and the Cherenkov photons are emitted by the fast charged particle traversing the radiator. The photons are detected in HMPID through which the hadrons are identified.

2.4.6 Photon Spectrometer (PHOS)

The Photon Spectrometer (PHOS) [102], consists of dense scintillating $PbWO4_4$ crystals offering both high granularity and exceptional energy resolution. PHOS is primarily designed for the precise measurement of direct photons and photons originating from the decays of neu-

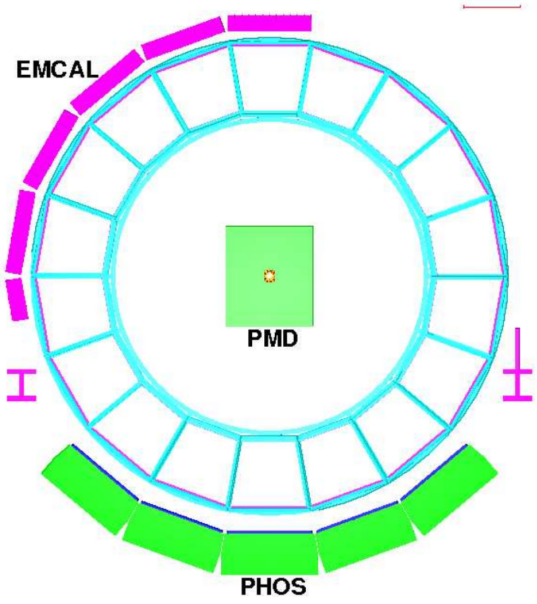

Figure 2.8: ALICE detector setup with PHOS, EMCAL and PMD sub-detectors [109]

tral mesons. Positioned at the lower part of ALICE's central barrel region, it covers only a limited portion. It covers pseudo-rapidity range of $|\eta| < 0.12$ and azimuthal range of 220^0-320^0.

2.4.7 Electro Magnetic Calorimeter (EMCAL)

Electro Magnetic Calorimeter (EMCAL) [102], is a sampling calorimeter located opposite to the PHOS and it has an azimuthal coverage between 80^0 to 187^0 and pseudo-rapidity coverage of $|\eta| < 0.7$. The major goal of EMCAL is to enhance the measurement of jets along with high-p_{T} photons and identification of electrons. When the photons and electrons enter the EMCAL, they produce an electromagnetic shower and deposit their energy in the EMCAL towers. The measurement of transverse energy in the range of 100 MeV to 100 GeV is performed using EMCAL. EMCAL also provides an efficient and fast trigger for hard jets, photons and electrons.

2.4.8 ALICE Cosmic Ray Detector (ACORDE)

ALICE Cosmic Ray Detector (ACORDE) [110], as the name suggests, provides a trigger for the cosmic rays. It has an azimuthal coverage of -60^0 to 60^0 and a pseudo-rapidity range

of $|\eta| < 1.3$ and it is placed on the top of the L3 magnet. ACORDE acts as a crucial detector to provide a fast L0 trigger signal during the alignment and calibration of several other ALICE tracking detectors.

2.5 Forward Detectors

2.5.1 V0

The V0 scintillator arrays [102, 111] play a pivotal role in ALICE, which helps in triggering and determining fundamental event properties. These arrays are instrumental in providing minimum-bias and centrality triggers while also measuring the multiplicity of charged particles. This multiplicity measurement is essential for determining event centrality in Pb–Pb collisions. Furthermore, the V0 arrays aid in distinguishing between beam-beam and beam-gas interactions, with the latter being excluded from physics analyses. Additionally, by capturing the azimuthal distribution of charged particles, the V0 system facilitates the determination of the event plane. Lastly, it enables the measurement of the LHC beam luminosity.

The V0 detector system comprises two independent arrays of scintillator counters, situated on either side of the nominal interaction point within the L3 solenoid. Their positions along the beam's (z) direction are asymmetric, as illustrated in figure 2.9. Specifically, V0A is positioned on the A side at z = 329 cm, while V0C is located directly in front of the hadronic absorber required for the muon spectrometer on the C side, at z = 87 cm, much closer to the nominal interaction point (z = 0). These arrays, situated near the beam pipe, cover the forward pseudo-rapidity ranges of $2.8 < \eta < 5.1$ for V0A and $-3.7 < \eta < -1.7$ for V0C. Each array consists of four rings, which are further subdivided into eight sections of 45° in azimuth, resulting in 32 channels per array.

The process of the centrality estimation is given in section 2.6.

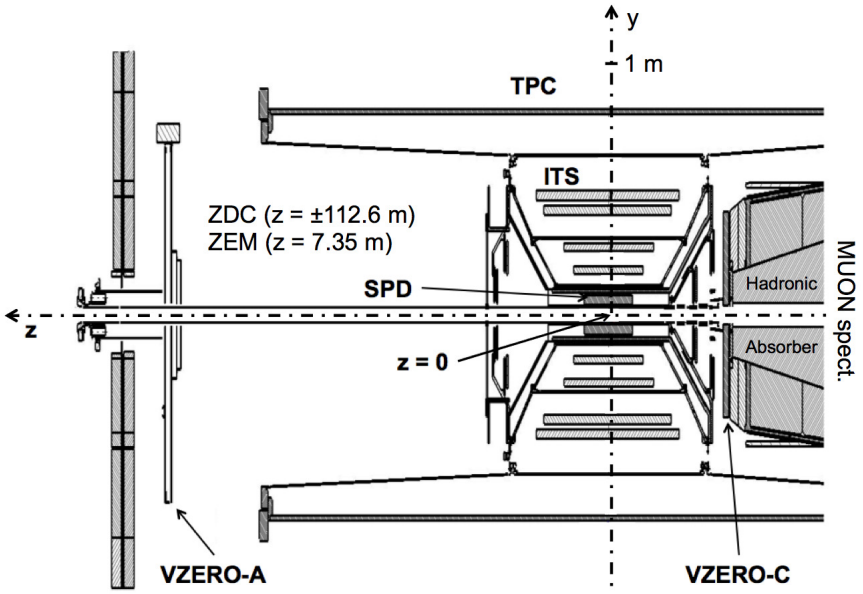

Figure 2.9: Position of the two VZERO arrays within the ALICE detector system [112].

2.5.2 Zero Degree Calorimeter (ZDC)

The ZDC [113] consists of four calorimeters, two tungsten-quartz neutron calorimeters (ZN) and two brass-quartz proton calorimeters (ZP). The calorimeters are symmetrically positioned at 112.5 m on either side of the interaction point (IP). The tungsten-quartz neutron and brass-quartz proton detectors have an η acceptance of $|\eta| > 8.8$, $6.5 < \eta < 7.5$ and full and $|\varphi| < 10^{\circ}$ azimutal coverage, respectively.

The spectator protons are detected in ZP after being separated from the ion beams by a dipole magnet, and the spectator neutrons, being charge neutral, move without deviation and are detected in ZN [113]. By measuring the deposited energy of spectator nucleons, the ZDC aids in estimating the centrality of heavy-ion collisions. Furthermore, the ZDC can help determine the reaction plane in nuclear collisions since it is a position-sensitive detector.

The position of zero-degree calorimeters in the ALICE detector system are depicted in Fig. 2.10.

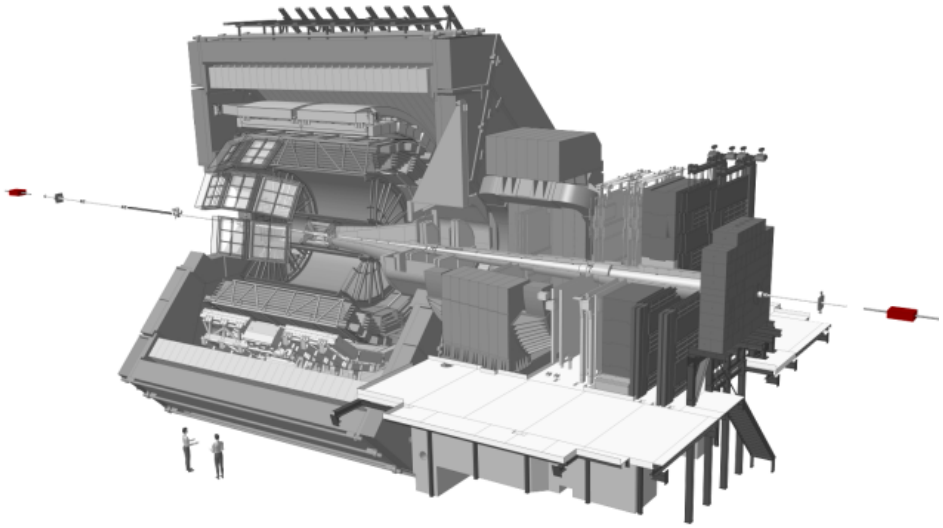

Figure 2.10: Position of the two zero degree calorimeters within of the ALICE detector system [113].

2.5.3 T0

The T0 [108] consists of two arrays of Cherenkov counters. The 1st array, T0A is located at z=375 cm with an η acceptance of $4.61 < \eta < 4.92$ and the 2nd array situated at $z = -72.7$ cm with an η acceptance $-3.28 < \eta < -2.97$. Being the fastest detector in ALICE, it provides the first trigger signal. The primary function of the T0 detector within ALICE is to measure collision interaction times, thereby establishing a start time (T0) for the Time-of-Flight (TOF) with a time resolution of about 25ps and 40ps in Pb–Pb and pp collisions, respectively. It also serves as an L0 trigger and measures the vertex position (with a precision of 1.5 cm) along the beam axis for each interaction. It provides a fast assessment of Pb-Pb collision multiplicity. Additionally, it sends the TRD a wake-up signal before L0.

2.5.4 Photon Multiplicity Detector (PMD)

PMD is a gas-based proportional counter and is positioned 3.64 meters away from the interaction point on the A-side and is perpendicular to the beam axis. It provides full azimuthal coverage and has a pseudorapidity range of $2.3 < \eta < 3.7$. It includes a charged particle veto

detector in front and a pre-shower detector behind it. On an event-by-event basis, it calculates the number and spatial (η - ϕ) distribution of photons in the forward direction.

The position of PMD in the ALICE detector is shown in Fig. 2.11.

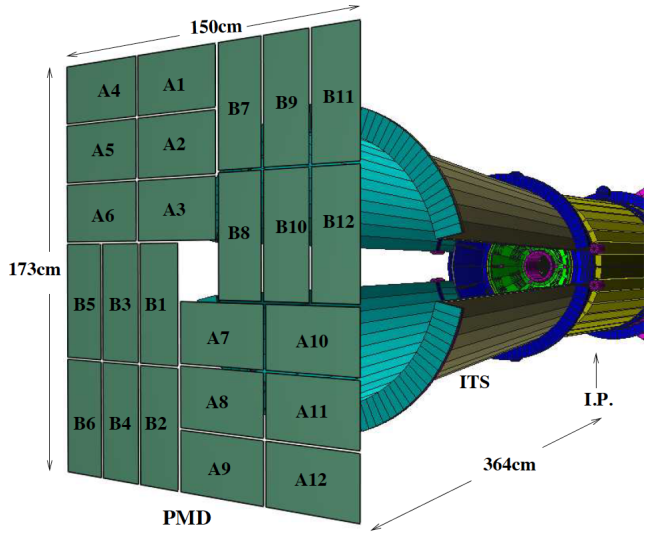

Figure 2.11: Position of PMD in ALICE detector system [108].

2.5.5 Forward Multiplicity Detector (FMD)

The FMD [108] comprises three sub-detectors, i.e., FMD1, FMD2 and FMD3 consisting of silicon strip detectors. FMD1 and FMD2 are situated on the A-side at a distance of 320 cm and 80 cm from the nominal IP and cover the pseudorapidity range of $3.6 \leq \eta \leq 5.0$ and $1.7 \leq \eta \leq 3.7$, respectively. FMD3 is situated on the C-side at a distance of 70 cm from the nominal IP and covers the pseudorapidity range of $-3.4 < \eta < -1.7$.

It helps in the measurement of charged particle multiplicity as well as the study of event-by-event multiplicity fluctuation, reaction plane determination, and elliptic flow measurement.

2.5.6 Muon spectrometer

The muon spectrometer, is designed to reconstruct muons and is located is located outside the central barrel covering the pseudorapidity range of $-4.0 < \eta < -2.5$ with full azimuthal

coverage. A carbon absorber has been placed in front of the spectrometer to reject most of the primary and secondary particles produced in the collisions at the interaction point. Thus, the p_{T} cut-off for muons has been chosen to be of $p_{\mathrm{T}} > 4$ GeV/c. The muons are measured by five tracking stations with two planes of the spectrometer. The momenta of muons are reconstructed via a dipole magnet placed outside the L3 magnet. An iron wall acts as a further muon filter after which two trigger stations are located. In addition, to protect from secondaries produced at large rapidity, an inner beam shield is placed in the spectrometer.

2.6 Determination of centrality

In ALICE, the determination of centrality is assessed in two alternative ways: either by the energy deposited in the ZDCs or by the multiplicity of charged particles detected in one of the detector systems. The "V0 amplitude" is the standard procedure, which is obtained by summing the amplitudes of the signals that are measured in the V0A and V0C arrays. These methods are essentially introduced because the collision geometry, often represented by the impact parameter (b), cannot be determined by the experiment directly. The impact parameter is basically the distance between the centre of two colliding nuclei. The total hadronic interaction cross-section percentile is hence used as a proxy for b, and is also called the centrality of collision of the system. The centrality values can go from 0 to 100 % which corresponds to the most central ($b = 0$) to peripheral collisions, respectively.

The event distribution as a function of V0 amplitude for Pb–Pb collision at $\sqrt{s_{\mathrm{NN}}} = 5.02$ TeV is shown in Fig. 2.12. A Monte Carlo (MC) implementation of the Glauber model together with a two-component model fitting is performed to describe the measured distribution. The heavy-ion collisions can be described by the Glauber model in a purely geometrical way. The geometrical quantities are computed as statistical averages performing the Monte Carlo simulation on an event-by-event basis. The nuclear density profile corresponds to the initial distributions of the nucleons in the two nuclei. With the assumption that they move in straight lines, nucleons experience collisions with other nucleons that correspond to the inelastic nucleon-

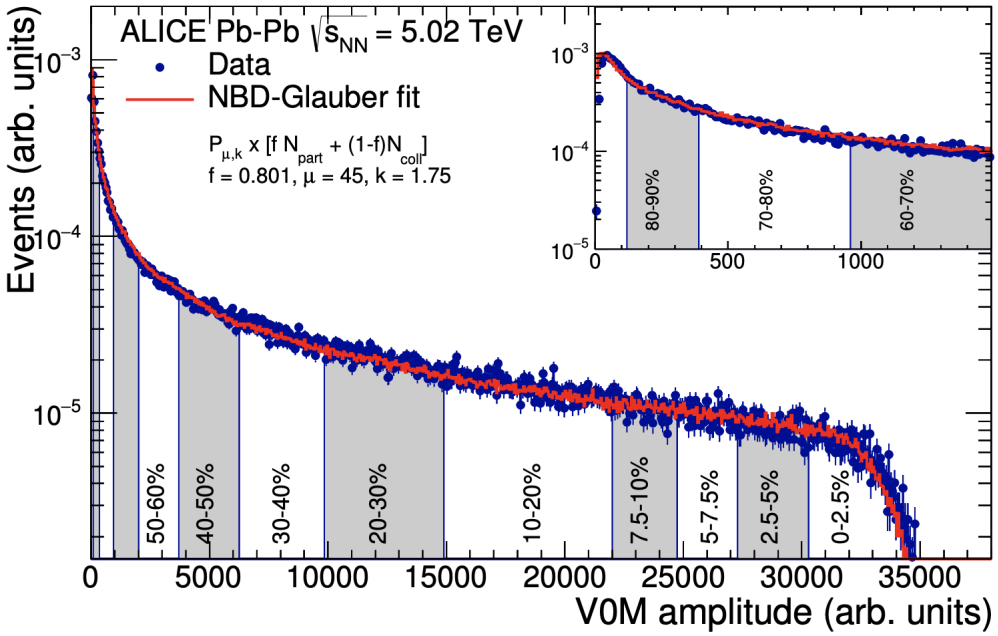

Figure 2.12: (Color online) Distribution of the sum of amplitudes in the V0 scintillators. The distribution is fitted with the NBD-Glauber fit (explained in the text) shown as a line. The inset shows a zoom of the most peripheral region [114].

nucleon cross section. In the two-component model, the effective number of particle-producing sources, N_{sources}, is given by:

$$N_{\text{sources}} = fN_{\text{part}} + (1 - f)N_{\text{coll}} \tag{2.3}$$

where, N_{part} and N_{coll} denote the number of participating nucleons and the number of binary nucleon–nucleon collisions respectively. The contribution from the soft processes is described by f which is proportional to N_{part} whereas the contribution from hard processes are described by $1 - f$ which is proportional to N_{coll}. The number of particles generated by each source is described using a Negative Binomial Distribution (NBD), parametrized by k and μ, where k controls the contribution at large multiplicities and μ is the mean multiplicity per source. The high-multiplicity region of the V0 amplitude distribution, which corresponds to the most central 90% of the cross-section, is fitted using the Glauber model. In this region, the contamination by electromagnetic processes and the effects of trigger inefficiency are negligible. The fit for the peripheral region is extrapolated from the central region. The point at which 90%

of the hadronic cross-section is achieved is determined using the integral of this fit, which gives an estimate of the total number of hadronic events. The measured event sample has a large fraction of non-hadronic interactions between 90–100% centrality. The centrality classes that are used to categorise the events in the 0–90% centrality range are shown in figure. 2.12. An extensive description of the centrality estimation in Pb-Pb collisions can be found in [115].

2.7 Track reconstruction, measurement of transverse momentum and particle identifcation

The event and track reconstruction process unfolds through two distinct phases:

1. Clusterization: During this initial step, the measured raw data is converted into clusters, which represent the positions in space and time. It also converts to signal amplitudes for select detectors. Importantly, this process is performed separately for each detector.

2. Vertex Estimation and Particle Tracking: In this subsequent phase, an initial estimation of interaction vertices is generated based on the clusters identified by the SPD. Following this, the tracking of charged particles occurs within the central barrel, culminating in the ultimate determination of the vertices.

2.7.1 Primary vertex determination:

The process begins with the usage of clusters from the two SPD layers, which correspond to the innermost layers of the ITS, to construct short tracklets. These SPD tracklets are then extrapolated to the expected beam positions. The point in space where the majority of these tracklets converge is identified, serving as the initial estimation of an interaction vertex. This particular vertex is referred to as the primary interaction vertex and it has the largest number of tracklets. Subsequently, in an iterative manner, additional vertices are sought, which may potentially arise from additional interactions occurring in the same or a nearby bunch crossing. This phenomenon of recording multiple interactions within a single event is termed "pile-up".

2.7.2 Track reconstruction:

Following the determination of the primary interaction vertex, the reconstruction of charged-particle tracks within the central barrel unfolds in a three-stage process, as described below:

1. Track Seed Generation and TPC Tracking:

   Initially, track seeds are generated using clusters from the outer TPC layers. These seeds are then propagated inwards, examining each pad row for the nearest cluster within a predefined search window.

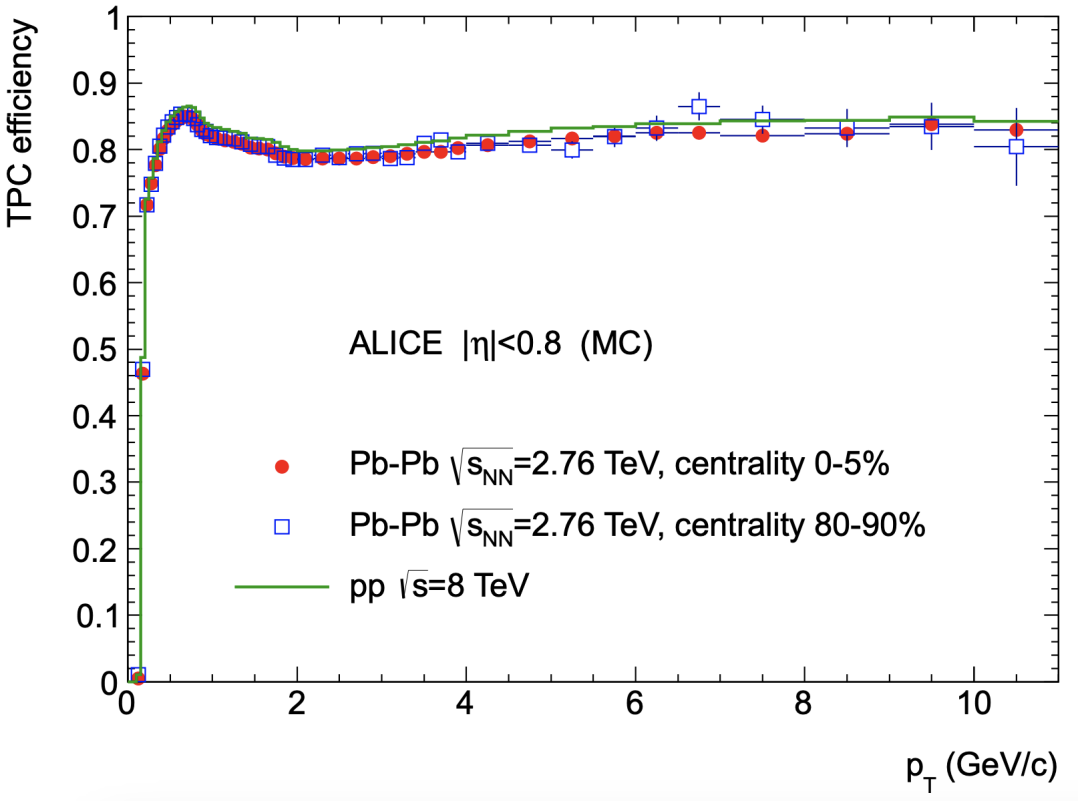

Figure 2.13: TPC track finding efficiency for primary particles in pp and Pb–Pb collisions (simulation) [114].

This procedure can assign up to 159 clusters to a single TPC track. Tracks identified during this initial iteration within the TPC are saved as "TPC-standalone" tracks. The track reconstruction continues by extending these TPC-standalone tracks outward to the

outermost ITS layer. Here, all clusters within the search window are used as seeds for distinct track hypotheses. These seeds are propagated through all six ITS layers, resulting in multiple ITS track candidates for each TPC track. The candidate with the highest track quality is merged with the TPC track, creating a global track that incorporates clusters from both the TPC and the ITS. Any ITS cluster not associated with global tracks are used to construct additional ITS standalone tracks, excluding information from the TPC.

Figure 2.13 illustrates the tracking efficiency, which is defined as the ratio between the reconstructed tracks and the generated primary particles in the simulation. This efficiency is plotted as a function of p_{T}. The drop in efficiency below a $p_{\mathrm{T}} \simeq 0.5$ GeV/c, is primarily due to energy loss within the detector material. The findings from proton-proton (pp) collisions are juxtaposed with those from 0–5% central and 80–90% peripheral lead-lead (Pb–Pb) collisions. This comparison highlights that the tracking efficiency of the TPC remains largely unaffected by the occupancy levels within the TPC, irrespective of the collision type.

2. Outward Propagation and Track Parameter Refinement:

   In the subsequent step, the tracks are propagated outward. Using the Kalman filter technique [116], the clusters identified in the first inward tracking stage are refitted, refining the track parameters. As the tracks reach the outer radius of the TPC, they are propagated to other detectors like the TOF, TRD, and HMPID. However, at this stage, there are no further updates to the track kinematics.

3. Inward Propagation and Final Track Refinement:

   Finally, the third tracking stage occurs, with the tracks being refitted once more, but this time inwards from the outer TPC radius to the innermost ITS layer. Ultimately, the kinematic track parameters of the global TPC-ITS tracks are stored within the event for further analysis and use.

   A more comprehensive description of charged-particle tracking and vertex reconstruction can be found in [114].

2.7.3 Transverse momentum reconstruction

Transverse momentum (p_{T}) is a fundamental and crucial measurable quantity of particles in high-energy physics. The three-momentum is a combination of its longitudinal component (p_z) and its transverse component (p_{T}). As mentioned in the previous subsections, ALICE is equipped with tracking detectors ITS and TPC. These detectors are designed to track the trajectories of particles when they move through the volume of the detector. In the transverse plane, the curvature of the trajectories of the particles is proportional to the charge of the particles and is inversely proportional to their transverse momentum. By the curvature measurement of these trajectories in the magnetic field of ALICE, the transverse momentum of the particles is determined. The trajectory of the charged particle with momentum (p) and charge (q) in a magnetic field of B(r) is given by the equation [117],

$$\frac{d^2\mathbf{r}}{d\mathbf{s}^2} = \frac{q}{p}\frac{dr}{ds}B(r). \tag{2.4}$$

Here, ds is the distance along the trajectory which is equal to vdt, and the vector $d^2\mathbf{r}/d\mathbf{s}^2$ is orthogonal to the trajectory. Its magnitude is equal to 1/R, where R(s) represents the curvature radius of the trajectory. The vector $d\mathbf{r}/d\mathbf{s}$ has unit length and is tangent to the trajectory. The coordinates along the trajectory are measured with position-sensitive detectors such as ITS and TPC, while the TOF and TRD detectors of ALICE provide the information on the identification of the particles which help to determine the p_{T} with high precision.

The precision of the p_{T} measurement is determined by the momentum resolution, which is influenced by both particle properties and detector capabilities. Data collected from these detectors undergo analysis through a pattern recognition program that associates coordinate measurements with particle trajectories, forming tracks. Equation 2.4 is employed along with the magnetic field map to fit these measurements to a track model. The primary parameters of interest for each track are its momentum vector and point of origin. The reconstructed tracks are subsequently combined to identify both primary and secondary vertices within the event.

The tracks are reconstructed within the TPC using 3-dimentional space points, and the transverse momentum is derived from the curvature of the track. The TPC is capable of recon-

structing primary tracks with momenta (p) ranging from 100 MeV/c to 100 GeV/c. Figure 2.14 illustrates the tracks reconstructed within the TPC from Pb-Pb collisions at $\sqrt{s_{\mathrm{NN}}}$ = 5.02 TeV in 2015.

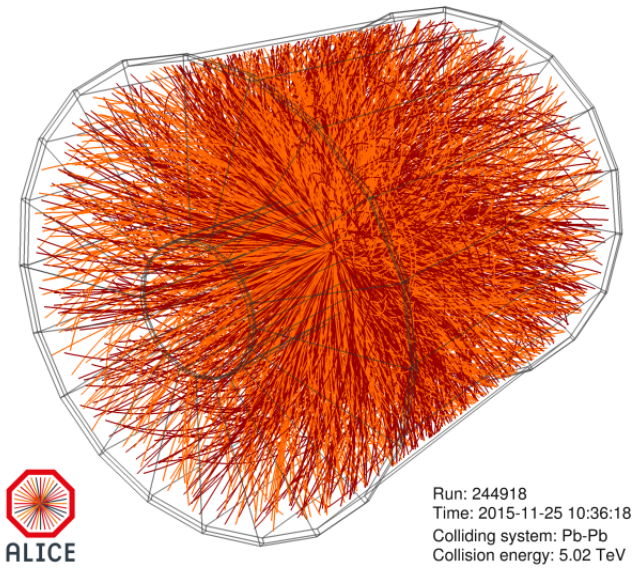

Figure 2.14: Event display of the tracks reconstructed inside TPC in Pb–Pb collisions at $\sqrt{s_{\mathrm{NN}}}$ = 5.02 TeV during 2015

2.8 Data acquisition and Trigger

In ALICE, the central online system controls the data-taking activities. A central interface, Detector Control System (DCS) operates all the detector hardware centrally and during data taking, the Data AcQuisition (DAQ) system is responsible for obtaining the configuration of the detectors. DAQ is also interfaced with the Trigger and High-Level Trigger (HLT) systems. All the operations of the central systems (DAQ, Trigger and HLT) are coordinated by the Experiment Control System (ECS) in the ALICE control room (ACR). A Standalone mode is used to perform detector commissioning, calibration and debugging activities, where detectors can operate individually. During the physics runs, the detectors are grouped in different partitions which can operate concurrently with a given set of inputs from the trigger.

2.8.1 Central Trigger Processor (CTP)

The trigger system of ALICE comprises a Central Trigger Processor (CTP) along with a High-Level Trigger (HLT) [118]. CTP consists of 24 Local Trigger Units (LTU) and it is defined for each detector. The LEVEL-0, L0 and LEVEL-1, L1 triggers are fast triggers. And their signal is delivered after 1.2 μs and 6.5 μs, respectively. The final trigger, L2, is delivered after 100 μs. After the L2 trigger is delivered, the event is stored. The output of the CTP then goes to the LTUs of each detector and then the output is transferred to the front-end electronics (FEE) of the detector via optical fibres and low-voltage differential signalling cables.

2.8.2 High-Level Trigger (HLT)

HLT defines firmware and software through a filtering mechanism to select interesting events in the entire sample. HLT receives the raw data via data links of detectors followed by extraction of hits and clusters to perform the basic detector calibration. Thereafter, the event is reconstructed for each detector and is selected on the basis of the physics region of interest. HLT also performs data compression at a later stage.

2.8.3 Data Acquisition (DAQ)

The Data Acquisition (DAQ) system handles the data flow from the detector's electronics to the permanent storage. The Local Data Concentrators (LDCs) read the events from the optical detector data links. The LDC assembles the data into the sub-events and ships to Global Data Collectors (GDCs). The whole event is built in GDCs. The GDCs record the events to a transient data storage and then it is migrated to the tape in the permanent data storage.

2.9 Offline Data structure and analysis

2.9.1 ALICE Grid and ALIEN

To efficiently manage and process the vast amount of distributed data resources, the ALICE Grid is introduced. Within this framework, data processing is distributed across multiple computing centres located worldwide. This distributed computing infrastructure, integral to the LHC experimental program, is coordinated through the Worldwide LHC Computing Grid (WLCG) project.

The ALICE Grid is organized according to the Models of Networked Analysis at regional centres (MONARC) model, which is structured into distinct stages and tiers. CERN is considered to be Tier-0. Here all the real data is originated. Tier-1 consists of large regional computing centres, which collaborate with CERN to ensure secure data storage.

Additionally, the ALICE Offline project has developed the ALIce Environment (ALIEN), enabling ALICE users to seamlessly access grid computing and storage resources.

2.9.2 AliRoot Framework

The raw data captured by the detectors undergoes a reconstruction process facilitated by the AliRoot software framework [102, 119, 120], which is built upon the C++-based ROOT framework [120, 121]. It is worth noting that a given dataset may be reconstructed multiple times, allowing for the incorporation of software improvements over time. Each reconstruction iteration is referred to as a "pass," and these passes are labelled sequentially (pass1, pass2, and so on).

The outcomes of this reconstruction process are stored in Event Summary Data (ESD) objects. ESD objects comprehensively contain all event-related information, encompassing details about vertices, tracks, and additional detector-level data. To reduce file size and expedite analysis, the ESD objects are further processed to generate Analysis Object Data (AOD) files. AOD files include only the information essential for physics analysis, resulting in significantly

smaller file sizes than their corresponding ESD objects. Moreover, due to their distinct internal structure, analysis processes are more efficient when conducted on AOD files.

However, it is important to note that certain analyses may necessitate access to information exclusively stored within the ESD objects. In general, physics analyses can be conducted using either the ESD or the AOD format, depending on the specific requirements of the analysis at hand.

In addition to the software package designed for ALICE physics analysis, there is a need for software capable of simulating events as they traverse through a detector. AliRoot integrates various software components such as GEANT3 and GEANT4 [122] to accurately simulate the interactions between particles and detector materials. Moreover, different Monte Carlo (MC) event generators simulate events corresponding to various collision types, including pp, p-Pb, and heavy-ion collisions.

Chapter 3

Analysis of event-by-event fluctuations of $\langle p_{\mathrm{T}} \rangle$ in pp, Xe–Xe and Pb–Pb collisions

This chapter focuses on a detailed description of the tools by which the analysis of the mean transverse momentum fluctuations in pp and Pb–Pb collisions at $\sqrt{s_{\mathrm{NN}}}$ = 5.02 TeV and Xe–Xe collisions at $\sqrt{s_{\mathrm{NN}}}$ = 5.44 TeV is performed. This chapter also describes details of event shape analysis in pp collisions at 5.02 and 13 TeV. In particular, the detailed study of data samples, collision environment used for all the systems, the description of the selection of events and tracks, the methodologies used to calculate statistical and systematic uncertainties, the Monte Carlo closure test and the determination of the charged particle pseudorapidity density derived from the accepted charged particles are highlighted in this chapter.

3.1 Data sample

The study in this chapter is based on ALICE data from Pb–Pb collisions at $\sqrt{s_{\mathrm{NN}}}$ = 5.02 TeV, Xe–Xe collisions at $\sqrt{s_{\mathrm{NN}}}$ = 5.44 TeV and pp collisions at $\sqrt{s_{\mathrm{NN}}}$ = 13 TeV, acquired during Run 2 in the form of Analysis Object Data (AOD) files. The details of the beam energy, the number of events, the trigger selection etc. are listed in table 3.1.

The online system of ALICE facilitates it to keep the data-taking process smooth and accurate. The five online systems that are included in this analysis, are described in the previous

System	Pb–Pb	Xe–Xe	pp
Energy	$\sqrt{s_{\mathrm{NN}}}$ = 5.02 TeV	$\sqrt{s_{\mathrm{NN}}}$ = 5.44 TeV	$\sqrt{s}$ = 5.02 TeV
Events	13 M	1.4 M	104 M
Event Trigger	Minimum-Bias (kINT7)	kINT7	kINT7
Centrality Estimator	V0M	V0M	V0M
Main detectors	TPC and ITS	TPC and ITS	TPC and ITS

Table 3.1: Details on the data set

chapter. The C++-based ROOT framework [123, 124] constitutes the AliRoot. The AliRoot software framework [102, 119, 125] is used to reconstruct the raw data obtained from the sub-detectors of ALICE in RUN-1 and RUN-2. Depending on how many times the raw data is reconstructed, the “pass" number is assigned (e.g. pass1, pass2 etc). For example, in this analysis, pass-3 of the LHC18q dataset is used for Pb–Pb collision.

Two kinds of output files can be used for analysis: Event Summary Data (ESD) objects and Analysis Object Data (AOD) files. In ESD objects, the reconstructed data is stored which contains crucial event information like vertices and tracks. The AOD files on the other hand are obtained by further processing the ESDs making them smaller in size than their corresponding ESDs. AODs are specific to provide information on the physics analysis.

To help researchers make predictions, gain insights, and test hypotheses, various computational tools are available that simulate the outcome of collisions in high-energy particle physics by generating random samples. These are called the Monto Carlo (MC) event generators. These data simulated from the MC event generators are used to compare with the experimental data for the collision systems. The models used in the Pb–Pb and Xe-Xe analysis are HIJING (heavy-ion Jet INteraction Generator) [126] and AMPT (A Multi-Phase Transport Model). For pp collisions, PYTHIA and EPOS models are used for comparison with the data.

3.2 Event selection

The standard event selection in the analysis includes basic trigger criteria, quality of primary vertex reconstruction (with TPC and ITS detectors) and removal of pile-up events.

3.2.1 Trigger selection

In order to extract useful information from the collected data, ALICE utilised multiple triggers. In ALICE, multiple triggers are usually active simultaneously, and each event retains information about the specific trigger it corresponds to. Subsequently, during the analysis phase, events associated with the relevant trigger class are chosen for further examination. The details of usage of such triggers can be found in [127].

In order to produce a data sample with the minimum amount of bias from the trigger decisions itself, minimum-bias (MB) triggers are used. The minimum bias trigger is the most basic class of trigger in the ALICE.

In this analysis, kINT7, which is a minimum bias trigger, corresponding to V0(AND) is used for all collision systems. "V0AND" stands for the logical "AND" combination of signals from the V0A and V0C detectors i.e. the detectors start after getting a signal from both the forward detectors i.e. V0A and V0C.

3.2.2 Vertex determination

The position in the z-axis, where the two beams collide is referred to as the “Vertex Z” position. One event is considered as the collision of two heavy ions or two protons depending on the type of system under action. For every event, one primary interaction vertex is identified and determined. The primary vertices are usually expected to spread over a few inches along the z-axis or in a plane perpendicular to the beam direction. In this analysis, the global TPC-ITS tracks are used for the determination of the vertex. To ensure a successfully reconstructed primary interaction vertex, certain criteria are implemented. Firstly, this is achieved by mandating the presence of at least one track contributing to the determination of the primary vertex.

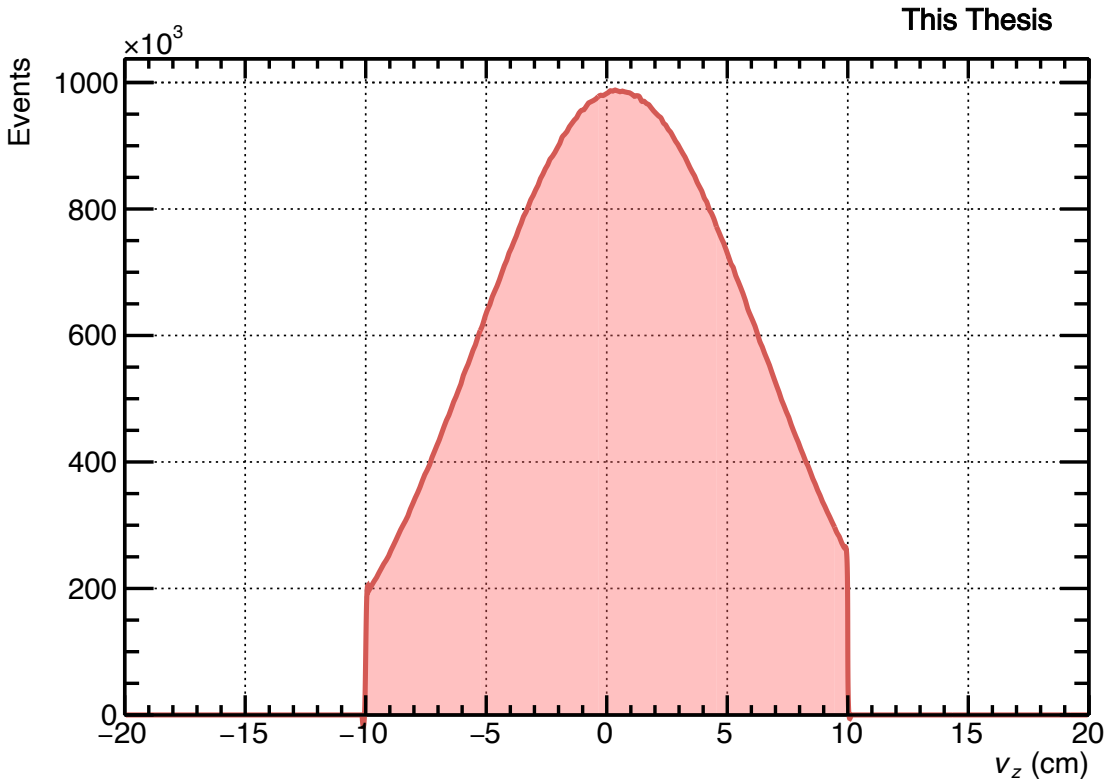

Figure 3.1: Primary vertex distribution in Pb–Pb collision at $\sqrt{s_{\mathrm{NN}}}$ = 5.02 TeV after event selection criteria

Additionally, a limitation is imposed on the maximum allowed distance of the reconstructed primary vertex from the nominal interaction point, which is at the centre of the experiment, along the beam's direction (z-direction), set at 10 cm. This selection criterion is crucial due to the impact it has on the geometrical acceptance of charged-particle tracks within the subdetectors concerning the vertex's z-position. At the precise location of the nominal interaction point (z = 0), the geometrical acceptance of the central barrel detectors symmetrically covers pseudorapidity. However, as the distance from this nominal centre increases, the acceptance changes asymmetrically, expanding on one side while reducing on the other side of the experiment. By setting the maximum z-vertex distance to 10 cm, a uniform tracking acceptance is ensured both in the Inner Tracking System (ITS) and in the Time Projection Chamber (TPC) within a pseudorapidity interval of $|\eta| < 0.8$. This standardized acceptance facilitates consistent and reliable tracking of particles across these detector systems [128].

Event selection criteria	
Trigger selection	Minimum Bias ("KINT7")
No. of vertex contributors	≥ 1
V_Z, distance from nominal interaction point	≤ 10
Distance b/w pile-up and primary vertex (SPD)	$\geq 0.8\ cm$
No. of SPD pile-up candidate vertices' contributors (pp)	≥ 3
No. of SPD pile-up candidate vertices' contributors	≥ 3, for $N_{SPDtrk} < 20$
(Pb–Pb and Xe–Xe)	≥ 4, for $20<N_{SPDtrk} < 50$
	≥ 5, for $N_{SPDtrk} > 50$

Table 3.2: Summary of the event selection criteria applied in this analysis for all collision systems.

The vertex z distribution after the application of each event cut is shown in Fig 3.1.

3.2.3 Pile-up removal

There are two primary categories of pileup events. Same-bunch-crossing pileup involves the occurrence of multiple collisions within the same bunch-crossing. This type of pileup is detected by all detectors. In drift detectors like the Time Projection Chamber (TPC) and Silicon Drift Detectors (SDD), the reconstructed points accurately align spatially, preserving correct track parameters estimation. The efficiency of extending tracks from TPC to ITS remains consistent for both the primary collision and any piled-up collisions. To address this, cuts based on multiple reconstructed vertices can be employed at the event selection stage to potentially remove these same-bunch-crossing pileup events.

The centrality percentile distribution before and after the applied event cuts is shown in Fig 3.2.

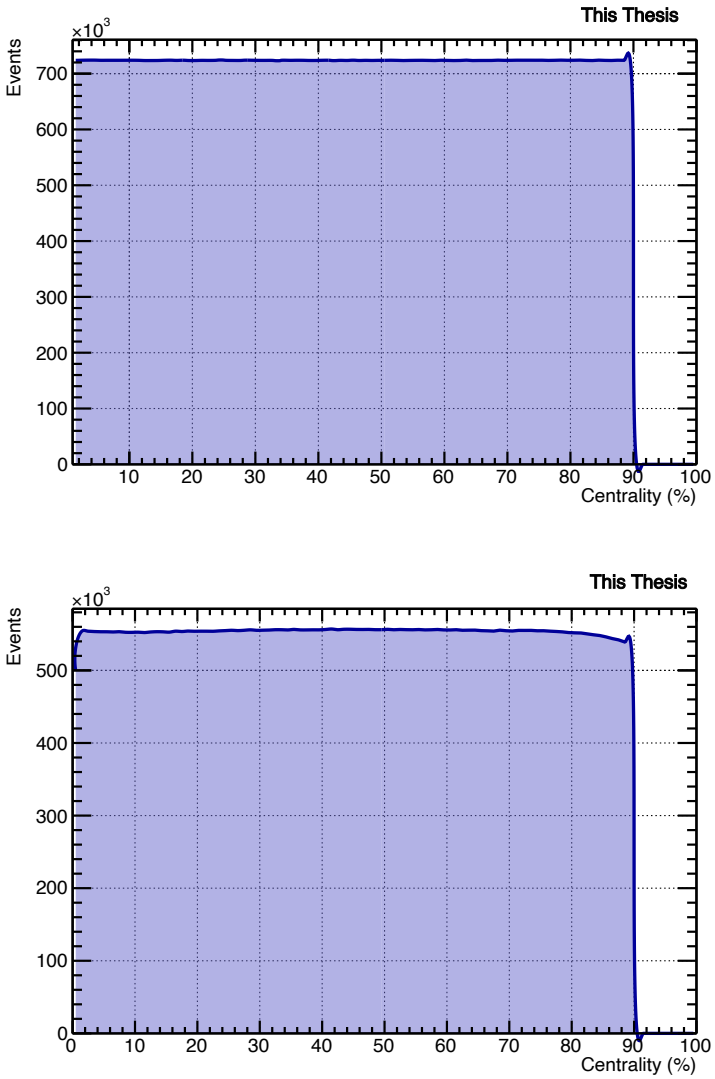

Figure 3.2: Centrality distribution before (upper panel) and after (lower panel) event cuts for Pb–Pb collisions at 5.02 TeV

Collisions occurring in neighbouring bunch crossings have the potential to be captured within the same event due to the relatively shorter time interval between two consecutive bunches, which is smaller than the detector's read-out time. This is referred to as out-of-bunch pileup. The impact of this type of pileup varies across detectors based on their readout time. Removal of out-of-bunch pileup can be attempted during event selection using cuts based on multiple reconstructed vertices and correlations between track/tracklets/amplitudes in different detectors [129].

The presence of particle tracks stemming from these extra interactions, poses a risk of distorting results, particularly when a pile-up vertex lies in close proximity to the primary interaction vertex. Such proximity could result in an inflated count of tracks assigned to the primary vertex, potentially skewing outcomes. In correlation analyses, these effects are notably sensitive. Tracks originating from distinct collisions exhibit a complete lack of correlation, potentially leading to a substantial reduction in any observed correlation signal.

To address the pile-up events across various collision systems, specific cuts are implemented to reduce their impact. In pp collisions, the requirement demands a minimum of three contributors (tracklets) associated with the identified pile-up candidate vertices. However, in the case of Pb-Pb and Xe-Xe collisions, this threshold varies based on the event multiplicity. In events where the primary vertex has a total of less than 20 SPD tracklets (N_{SPDtrk}), the criterion for the minimum number of tracklets associated with the pile-up vertex is established at three. For primary vertices where the N_{SPDtrk} count falls between 20 and 50, and in cases where N_{SPDtrk} is greater than or equal to 50, the prescribed minimum number of tracklets associated with the pile-up vertex adjusts to four and five, respectively [130].

Additionally, there is a stipulation for a minimum separation distance, measured in centimetres along the z-direction, between the primary vertex and any identified candidate pile-up vertices, ensuring it is greater than or equal to 0.8 cm for all collision systems.

In total, 13 million, 1.4 million, and 104 million events passed the above criteria and were retained towards the analysis of $\langle p_{\mathrm{T}} \rangle$ fluctuations in Pb–Pb, Xe–Xe, and pp collisions, respectively.

3.3 Track selection

ALICE's central barrel consists of key tracking detectors, the Time Projection Chamber (TPC) and the Inner Tracking System (ITS). The reconstruction of charged-particle trajectories is described in section 2.7.2. Throughout the analysis, track selection criteria are meticulously applied to select primary charged particles stemming from the primary interaction vertex. These

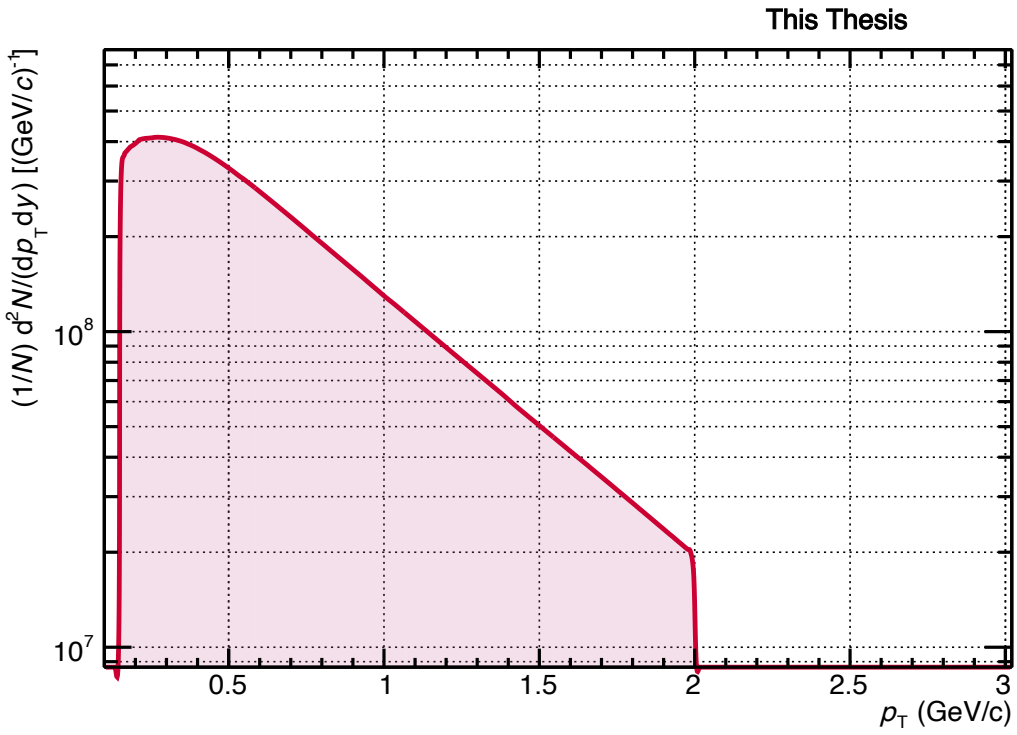

Figure 3.3: p_{T} distributions of selected tracks for Pb–Pb collisions at 5.02 TeV

selection criteria serve the purpose of effectively diminishing the presence of spurious trajectories unrelated to physical particles and low-quality tracks.

Measurements of $\langle p_{\mathrm{T}} \rangle$ fluctuations are based on charged particle tracks reconstructed within the ITS and the TPC. To ensure uniform tracking efficiency, the analysis is restricted to particles produced within the pseudorapidity range of $|\eta| < 0.8$. Additionally, the transverse momentum range of $0.15 < p_{\mathrm{T}} < 2$ GeV/c is chosen for all charged particles. The higher p_{T} cut is chosen to focus the analysis on the soft and “bulk" part of the system. The lower p_{T} limit is chosen because the reconstruction efficiency of the TPC decreases below this limit.

In pp collisions, the analysis is limited to charged tracks with a minimum of 70 out of a maximum of 159 reconstructed space points in the TPC. For Pb–Pb and Xe–Xe collisions, a p_{T}-dependent cut of the number of TPC clusters per track, $N_{\mathrm{TPC}} = 70 + 1.5 \times p_{\mathrm{T}}$, was applied to further limit the probability of split tracks arising from running conditions yielding large hit occupancy in the TPC. Furthermore, for all collision systems, a maximum χ^2 per TPC and ITS cluster of 4 and 36, respectively, were used to further suppress contamination associated

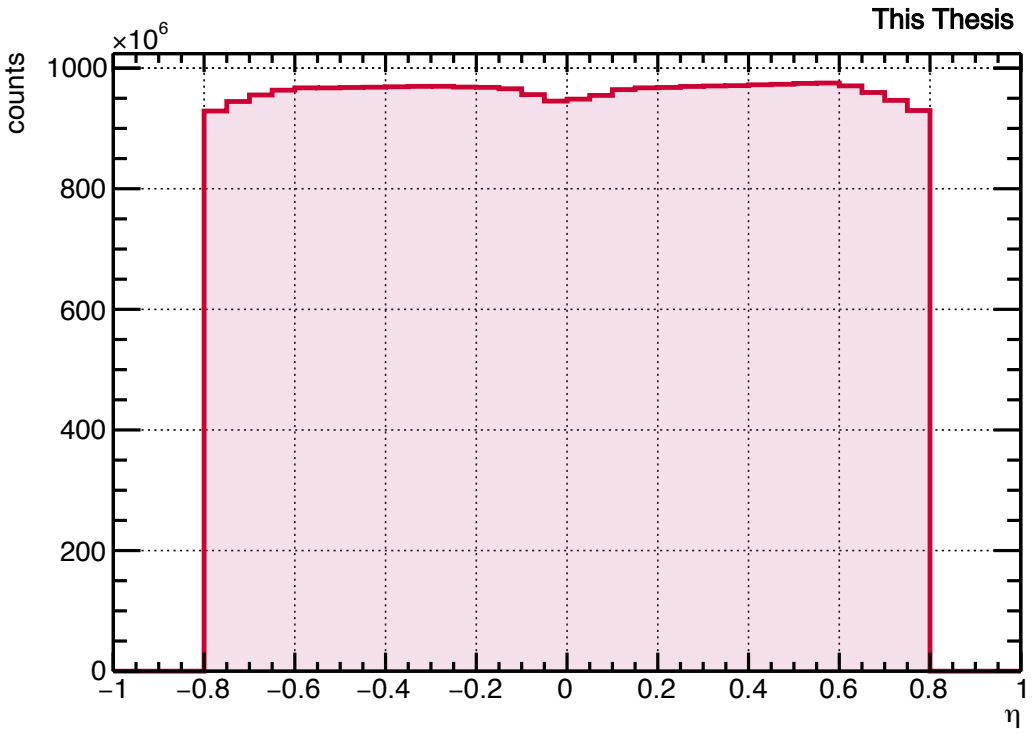

Figure 3.4: η distributions of selected tracks for Pb–Pb collisions at 5.02 TeV

with poor-quality tracks. Besides, kinks, which are the daughter tracks from reconstructed secondary weak decay topologies, are rejected. The closest distance between a reconstructed track and the primary vertex of the collision event along the track's trajectory is called the Distance of Closest Approach (DCA). It essentially measures how close a particle's trajectory is to the collision point. The DCA in the longitudinal and transverse direction is taken to be less than 1 cm ($DCA_z < 1$ cm, $DCA_{xy} < 1$ cm) respectievly for Pb–Pb and Xe–Xe collisions. A criterion $DCA_z < 2$ cm and a p_T dependent cut of $DCA_{xy} < 0.0182\,mm + \frac{0.0350\,mm}{p_T^{1.01}}$ was applied for pp collisions. A summary of track selection criteria is listed in Table 3.3.

These track selection criteria serve to enhance the purity and reliability of the selected particle tracks for analysis. The p_T and η distribution of the selected track are shown in Fig 3.3 and Fig 3.4 respectively.

Track selection criteria	
Pseudo-rapidity (η) range	$\lvert\eta\rvert < 0.8$
Transverse momentum (p_T) range	$0.15 < p_T < 2.0$ GeV/c
Number of TPC clusters (pp)	≥ 70
p_T-dependent Number of TPC clusters	$\geq 70 + 1.5 \times p_T$ for $p_T < 20.0$ GeV/c
(Pb–Pb and Xe–Xe)	≥ 100 for $p_T > 20.0$ GeV/c
Reject kink daughters	Yes
DCA to vertex along beam direction (pp)	< 2 cm
DCA to vertex along beam direction (Pb–Pb and Xe–Xe)	< 1 cm
DCA to vertex along xy plane (pp)	$< 0.0182\,mm + \frac{0.0350\,mm}{p_T^{1.01}}$
DCA to vertex along xy plane (Pb–Pb and Xe–Xe)	< 1 cm

Table 3.3: Summary of the track selection criteria applied in this analysis for all collision systems.

3.4 The two particle correlator

The mean transverse momentum ($\langle p_{\mathrm{T}} \rangle$) of a multiplicity class is calculated by taking the mean of individual transverse momenta of tracks belonging to a particular multiplicity class. The calculation is done on an event-by-event basis given by the following expression:

$$\langle p_{\mathrm{T}} \rangle = \frac{\langle \sum_{i=1}^{N_{\mathrm{ch}}} p_{\mathrm{Ti}} \rangle}{\langle N_{\mathrm{ch}} \rangle}, \tag{3.1}$$

Where, N_{ch} represents the charged particle counts within a specific event, while p_{Ti} signifies the transverse momentum of the i^{th} particle. The angular brackets encompass an average computed across multiple events within a given multiplicity class. In every event, the moments of the p_{T} distributions are evaluated. This is defined by,

$$Q_{\mathrm{n}} = \sum_{i=1}^{N_{\mathrm{ch}}} (p_{\mathrm{T,i}})^n, \tag{3.2}$$

where $p_{\mathrm{T,i}}$represents the transverse momentum of particles, $i = 1, \ldots, N_{\mathrm{ch}}$, selected towards the measurements of $\langle \Delta p_{\mathrm{T},1} \Delta p_{\mathrm{T},2} \rangle$ and N_{ch} is the number of such selected charged particles in an event. One verifies that $\langle \Delta p_{\mathrm{T},1} \Delta p_{\mathrm{T},2} \rangle$ can be readily computed according to,

$$\langle \Delta p_{\mathrm{Ti}} \Delta p_{\mathrm{Tj}} \rangle = \left\langle \frac{(Q_1)^2 - Q_2}{N_{\mathrm{ch}}(N_{\mathrm{ch}} - 1)} \right\rangle - \left\langle \frac{Q_1}{N_{\mathrm{ch}}} \right\rangle^2 \tag{3.3}$$

This implementation of the analysis presents the significant advantage that it does not involve nested loops on pairs of particles. Indeed, only single loops are required for the event-by-event determination of Q_1 and Q_2. The analysis is thus compact and fast. Additionally, in order to study the particle density dependence of the correlator and minimize smearing effects associated with broad bin widths, the analysis is performed in narrow multiplicity bins.

This analysis studies event-by-event fluctuations of the event-wise mean transverse momentum, $\langle p_{\mathrm{T}} \rangle$, of charged particles produced in pp, Xe–Xe and Pb–Pb collisions. The magnitude of the p_{T} fluctuations is quantified based on the two-particle correlator. In addition, to

understand the impact of the presence of jets in the measurement of $\langle p_{\mathrm{T}} \rangle$ fluctuations, a transverse spherocity dependence study has been performed in pp collisions.

3.5 Transverse spherocity dependence of $\langle p_{\mathrm{T}} \rangle$ fluctuations in pp collisions at $\sqrt{s}$ = 5.02 and 13 TeV

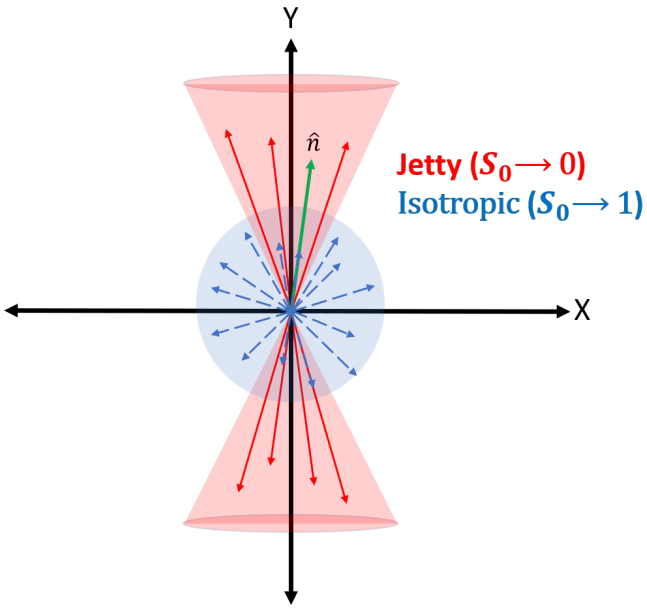

Figure 3.5: Depiction of jetty and isotropic events based on transverse spherocity [131]

In the context of event-by-event analysis mean transverse momentum fluctuations of charged particles, it is crucial to perform multiple differential studies of the experimental observables, event-by-event, in small systems, and to correlate these observables with initial and final state observables, such as the charged-particle multiplicity. Several different observables can be used to classify different event topologies and to study final state observables in relation to the event shape. Among them, the transverse spherocity and relative transverse activity classifier allow the possibility to distinguish and characterize events by a different content of hard versus soft particle production and to select therefore interactions with a different number of multi-parton interactions (MPI). The goal of these studies is to better understand the production

mechanisms of particles in hard and soft processes [132, 133]. The transverse spherocity is given by,

$$S_0 = \frac{\pi^2}{4} \min_{\hat{n}} \left(\frac{\sum_{i=1} \vec{p_{\mathrm{T_i}}} \times \hat{n}}{\sum_{i=1} \vec{p_{\mathrm{T_i}}}} \right)^2, \tag{3.4}$$

where i runs over a total number of charged-particle tracks in a given event and $\hat{n}$ is a unit vector that minimizes Eq. 3.4. The shape of the events for the two extreme values of transverse spherocity is depicted in Fig. 3.5. As Events with $S_0 \to 0$ are dominated by a single back-to-back jet-like structure while events with $S_0 \to 1$ are dominated by isotropic particle production.

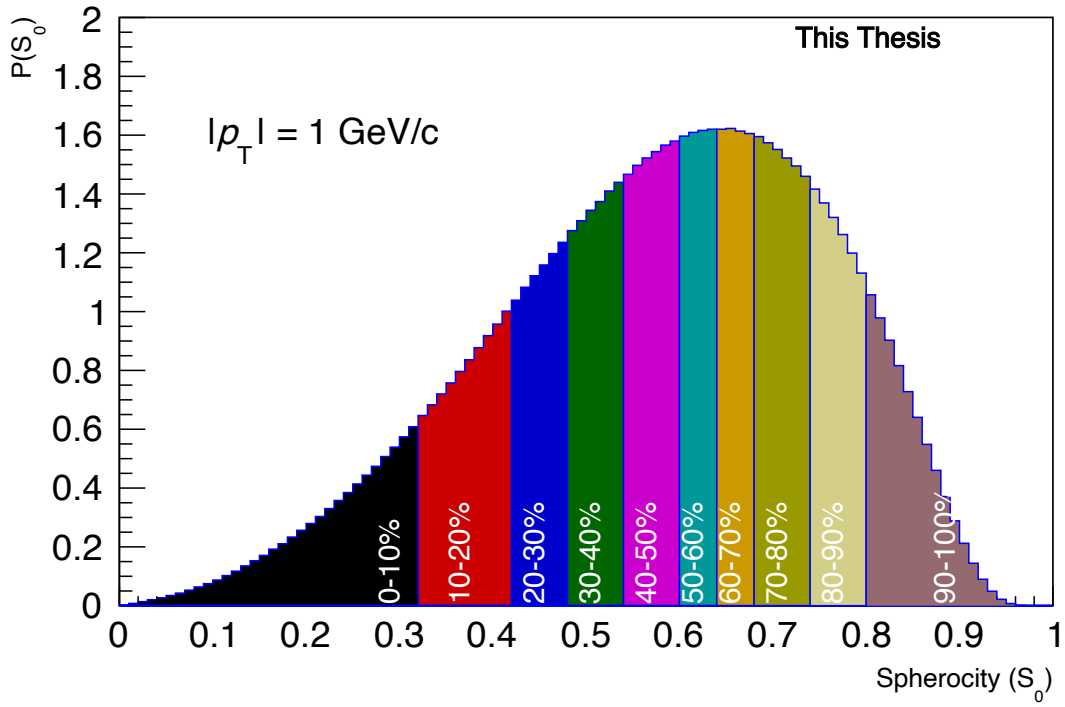

Figure 3.6: Transverse spherocity distribution in pp collisions at $\sqrt{s}$ = 5.02 TeV with depiction of the cuts for jetty and isotropic events

Figure 3.6 illustrates the spherocity distribution resulting from the analysis of proton-proton (pp) collisions at a center-of-mass energy of $\sqrt{s}$ = 5.02 TeV, with unweighted transverse

momentum (p_{T}). The various coloured bands in the figure correspond to distinct spherocity bins, each spanning a range of 10%.

The spherocity limits for pp collisions at $\sqrt{s}$ = 5.02 TeV, for the top 20% are determined to be from 0.005 to 0.425, indicating a predominantly jet-like configuration. In contrast, the lowest 20% of the distribution exhibits spherocity values ranging from 0.745 to 0.985, signifying an isotropic or more spherical arrangement of events.

Overall, the integrated events span the entire spherocity range from 0.005 to 0.985, covering the entire 0-100% range of the spherocity distribution.

For this analysis, the p_{T}-unweighted definition of transverse spherocity ($p_{\mathrm{T}} = 1$) is used to ensure that the spherocity selection affects charged and neutral particles alike. It is given by,

$$S_0^{p_{\mathrm{T}}=1} = \frac{\pi^2}{4} min_{\hat{n}=(n_x,n_y,0)} \left(\frac{\sum_{i=1} \hat{p_{\mathrm{T_i}}} \times \hat{n}}{N_{\mathrm{trks}}} \right)^2, \tag{3.5}$$

where N_{trks} is the total number of charged tracks. The interpretation of the measurement remains unaffected when one chooses between the two spherocity variants. Events containing at least 5 tracks, $N_{\mathrm{trks}} > 4$, which ensures that it is meaningful to talk about a topology, are considered candidates for the transverse spherocity distribution. The track selection criteria are chosen to have full azimuthal coverage. The spherocity distribution is related to the two limits by selecting the upper/lower percentiles of the distribution. Fig. 3.7 illustrates the comparison of p_{T}-weighted and unweighted spherocity distributions.

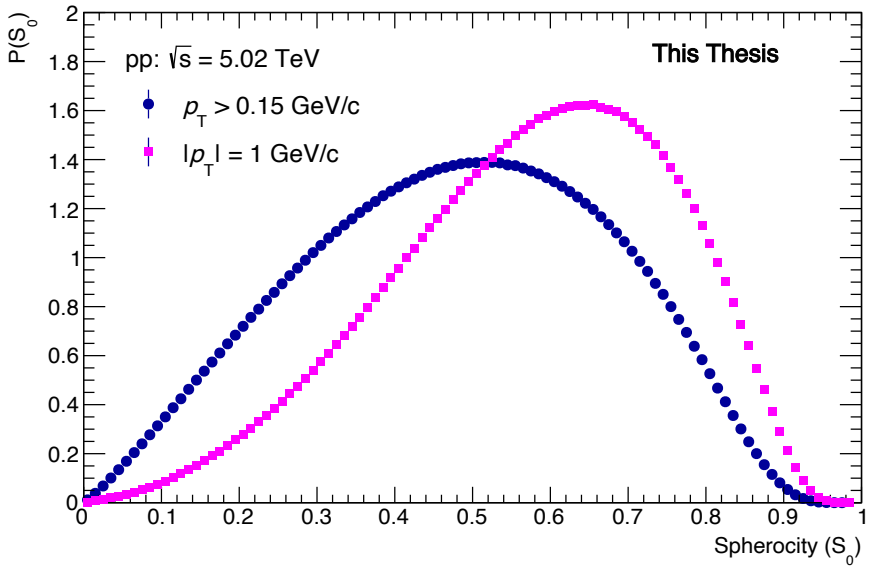

Figure 3.7: p_{T}-weighted and unweighted spherocity distributions in pp collisions at $\sqrt{s}$ = 5.02 TeV

3.6 Monte Carlo closure test

A study of the impact of the detector response and analysis procedure on the measured observables was carried out based on detailed simulations of the performance of the ALICE detector. The study was performed by processing simulated collisions generated with Monte Carlo event generators and then propagated to GEANT3 [134] which contains the geometry of the various components of the ALICE detector to account for energy and momentum losses and scatterings of produced particles within the fiducial volume of the measurement. The events which pass through the GEANT3 are called reconstructed events. The reconstructed events include losses due to detector inefficiencies, resolution smearing effects and potential sources of contamination of the signal due to poorly reconstructed tracks and tracks resulting from secondary particles. Hence, ratios of the observables of interest in reconstructed events and generated events would deviate from one. A perfect Monte Carlo closure is achieved when the estimations at reconstructed level agree with those obtained at the generator level. The event generators used for the MC closure tests were HIJING [126] for Pb–Pb and Xe–Xe collisions, and PYTHIA 8 [135] for pp collisions.

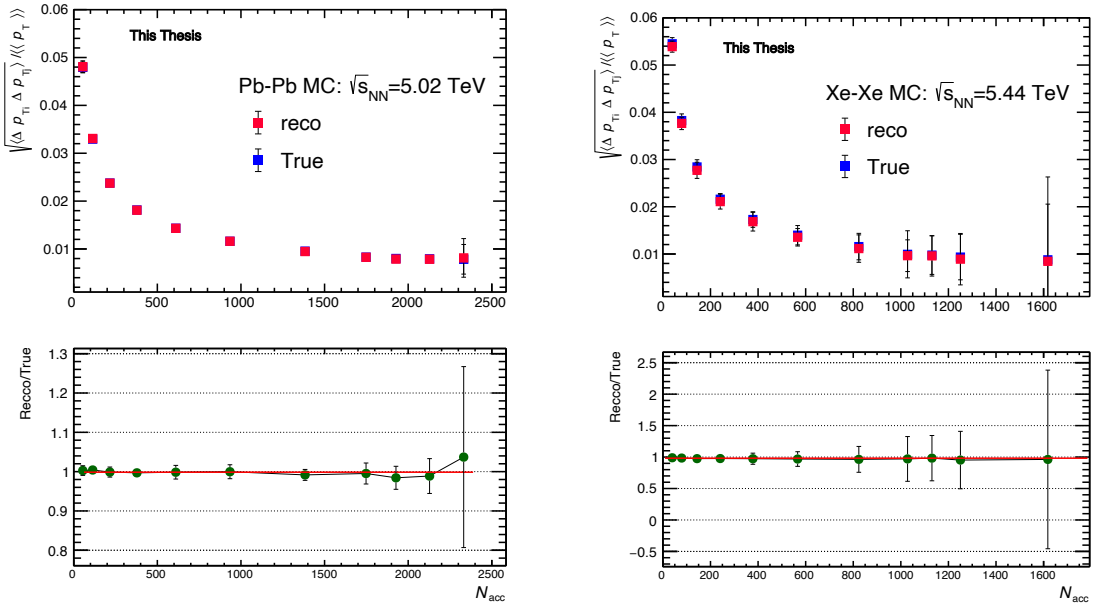

Figure 3.8: The upper panel shows the comparison of generated and reconstructed values of $\sqrt{\langle \Delta p_{\mathrm{Ti}} \Delta p_{\mathrm{Tj}} \rangle}/\langle\langle \mathrm{p_T} \rangle\rangle$ as a function of N_{acc} in Pb–Pb collisions at $\sqrt{s_{\mathrm{NN}}}$ =5.02 TeV (Left) and Xe–Xe collisions at $\sqrt{s_{\mathrm{NN}}}$ =5.44 TeV(Right). The lower panel shows the ratio of reconstructed to generated values of $\sqrt{\langle \Delta p_{\mathrm{Ti}} \Delta p_{\mathrm{Tj}} \rangle}/\langle\langle \mathrm{p_T} \rangle\rangle$ as a function of N_{acc}.

The observable, $\sqrt{\langle \Delta p_{\mathrm{Ti}} \Delta p_{\mathrm{Tj}} \rangle}/\langle\langle p_{\mathrm{T}} \rangle\rangle$, was calculated for Monte Carlo data at generated (true) and reconstructed level. Figure. 3.8 shows the comparision of $\sqrt{\langle \Delta p_{\mathrm{Ti}} \Delta p_{\mathrm{Tj}} \rangle}/\langle\langle p_{\mathrm{T}} \rangle\rangle$, for generated and reconstructed MC data in Pb–Pb and Xe–Xe collisions. In both cases, the deviations between reconstructed and generated levels do not exceed 2%. Thus, $\sqrt{\langle \Delta p_{\mathrm{Ti}} \Delta p_{\mathrm{Tj}} \rangle}/\langle\langle p_{\mathrm{T}} \rangle\rangle$ is robust against particle losses due to detector inefficiencies. The minor deviations from perfect closure are conservatively added to the systematic uncertainties.

For pp collisions, the reconstructed and true values of the observable agree with each other with a maximum discrepancy of 2% (see Fig. 3.9). To ensure the feasibility of the analysis methodology, MC closure test was also performed for pp collisions at $\sqrt{s}$ = 5.02 TeV and $\sqrt{s}$ = 13 TeV for different kinds of events as distinguished by unweighted transverse spherocity. The closure test for jetty and isotropic events in pp collisions at $\sqrt{s}$ = 5.02 TeV has also been performed and is shown in the left and right panels of Fig. 3.10. It is found that, for both jetty and isotropic events, the perfect closure is achieved within 1% and 2%, respectively.

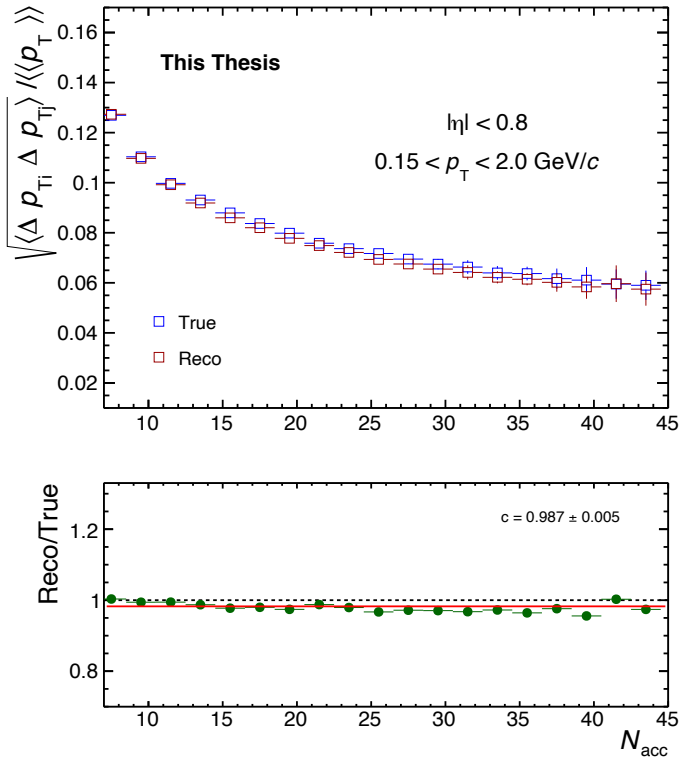

Figure 3.9: The upper panel shows the comparison of generated and reconstructed values of $\sqrt{\langle \Delta p_{Ti} \Delta p_{Tj} \rangle}/\langle\langle \mathrm{p_T} \rangle\rangle$ as a function of N_{acc} for pp collisions at $\sqrt{s}$ = 5.02 TeV for spherocity Integrated events. The lower panel shows the ratio of reconstructed to generated values of $\sqrt{\langle \Delta p_{Ti} \Delta p_{Tj} \rangle}/\langle\langle \mathrm{p_T} \rangle\rangle$ as a function of N_{acc}.

As there is a good agreement with the reconstructed and generated data observed for all collision systems, the efficiency correction has not been performed for the real data.

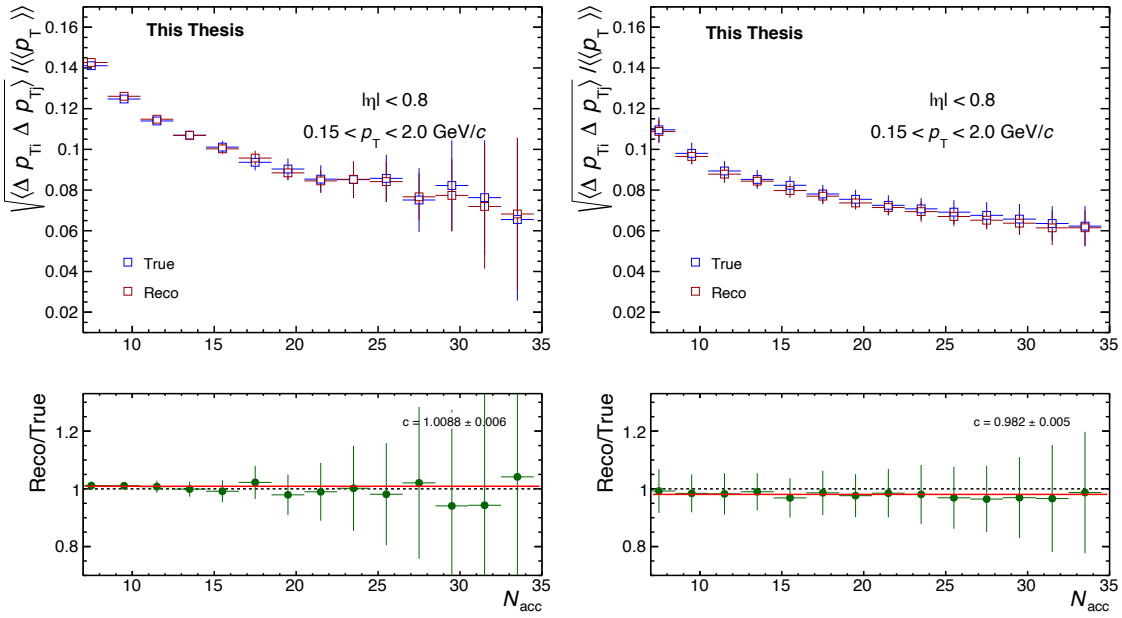

Figure 3.10: The upper panel shows the comparison of generated and reconstructed values of $\sqrt{\langle \Delta p_{Ti} \Delta p_{Tj} \rangle}/\langle\langle \mathrm{p_T} \rangle\rangle$ as a function of N_{acc} in pp collisions at $\sqrt{s}$ = 5.02 TeV for jetty events (Left) and isotropic events(Right). The lower panel shows the ratio of reconstructed to generated values of $\sqrt{\langle \Delta p_{Ti} \Delta p_{Tj} \rangle}/\langle\langle \mathrm{p_T} \rangle\rangle$ as a function of N_{acc}.

3.7 Estimation of statistical and systematics uncertainties

The statistical uncertainties arise due to the limited number of measurements in an experiment. They represent the precision of the measurement. Including these error bars helps convey the accuracy of the measured values. Systematic uncertainties account for potential biases and inaccuracies introduced by the experimental setup, calibration, or analysis techniques. These can affect the results consistently and need to be quantified to provide a complete understanding of the measurement's reliability. Different experiments or different analysis techniques may yield results with different uncertainties. By including these error bars, the results can be compared more accurately and the agreement or discrepancies between experiments or theoretical predictions can be looked upon.

3.7.1 Statistical uncertainty calculation

A subsampling method is used to calculate the statistical uncertainty associated with the observable. The subsampling method is a statistical approach utilized to gauge uncertainties or standard errors within a dataset. It involves iteratively selecting smaller subsets, known as subsamples, from the original dataset and computing the desired parameter for each of these subsets. This process aims to assess the variability or uncertainty in the parameter of interest by observing its fluctuations across multiple subsamples drawn from the original dataset. Here is a simplified explanation of how statistical uncertainty is estimated using the subsampling method in this analysis:

- Choosing subsample: Entire sample is divided into m number of subsamples. For instance for a sample having n number of events, m number of events with the condition, $m < n$, can be chosen repeatedly to form each subsample. In this analysis, 30 subsamples with similar statistics are selected.

- Calculating standard deviation: The standard deviation for each subsample is calculated for each multiplicity bin. The formula to estimate the standard error, using the subsampling method is given by:

$$S = \sqrt{\frac{1}{N-1}\sum_{i=1}^{N}(x_i - \overline{x})^2}, \tag{3.6}$$

  In the above equation, the observable, x_i, here the two-particle correlator, is calculated for each of the subsamples of a bin. $\overline{x}$, which is the mean value of the correlators in all samples, is calculated for the same multiplicity bin. The sum of squared differences between each x_i belonging to the i^{th} sample and the $\overline{x}$, is calculated for all "N" number of subsamples per bin. This sum is then divided by $N-1$ to get the variance of the subsample. To get an unbiased estimate of the standard deviation of the whole population, from a sample dataset, $N-1$ is divided instead of N in the denominator. This adjustment, known as Bessel's correction, ensures that the calculated sample standard deviation tends to be closer to the true population standard deviation. Finally, the square root of the variance then gives the standard deviation of the desired multiplicity bin.

The standard deviation for all multiplicity bins is then calculated to get the statistical uncertainties of the measurement.

3.7.2 Systematic uncertainty estimation

Systematic uncertainty refers to potential biases or errors arising from systematic effects within the experimental setup, data collection, or analysis techniques. These uncertainties stem from consistent and repeatable sources that could influence the measurement and are distinct from random fluctuations or statistical uncertainties. Several potential sources of systematic uncertainties were considered due to the variation of event and track selection criteria, including effects due to event pile-up, contributions from poorly formed tracks, secondary tracks, non-uniformity of the acceptance, and possible dependencies of the track reconstruction efficiency of the position of the primary vertex. Testing for these contributions was accomplished by studying the variation of $\sqrt{\langle \Delta p_{\mathrm{Ti}} \Delta p_{\mathrm{Tj}} \rangle}/\langle\langle p_{\mathrm{T}} \rangle\rangle$ from its baseline value (obtained using the default cuts) in response to variations of event and track quality selection criteria used in the analysis.

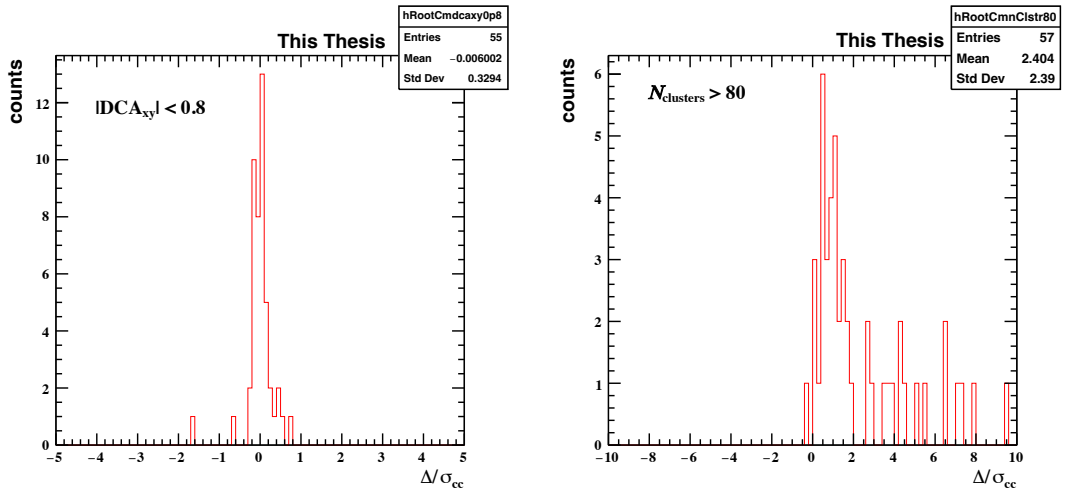

Figure 3.11: Distribution of Δ/σ_{cc} for the variations which pass the Barlow test (left) and which fail the Barlow test (right) for Pb–Pb collisions at $\sqrt{s_{\mathrm{NN}}} = 5.02$ TeV

To check whether a particular set of cuts qualifies to be considered as a potential source of systematic uncertainty, a Barlow test is performed. A brief description of the Barlow test is given below.

Parameter	Default	Variation-1	Variation-2
$\|V_z\|$ (cm)	10	8	-
$\|DCA_{xy}\|$ (cm)	1	0.8	1.2
$\|DCA_z\|$ (cm)	1	0.8	1.2
No. of TPC Clusters	70	80	-
Pile up	Cut applied	Cut applied	
Polarity	LHC18q (+ve)	LHC18r (-ve)	
Track quality	Filtler bit-768	Filtle bit-96	

Table 3.4: Sources of systematic uncertainties for Pb–Pb and Xe–Xe collisions at $\sqrt{s_{\rm NN}}$ = 5.02 TeV. The red and orange shaded cells show the variations that are passed by the Barlow checks in Pb–Pb and Xe–Xe collisions, respectively.

Let D be the default measurement, i.e. the value of the correlator with the default set of cuts for all sources of uncertainty taken into account and σ_D be the statistical uncertainty associated with the default value. Let A be the alternate measurement i.e. the value of the correlator after altering one set of cut amongst all the variations of sources considered whose statistical uncertainty is given by σ_A. Then the difference in the default and alternate measurement can be represented as Δ, which is given by:

$$\Delta = D - A \tag{3.7}$$

The square root of the squared differences in the standard deviation of the default and alternate measurements is given by:

$$\sigma_{cc} = \sqrt{|\sigma_D^2 - \sigma_A^2|} \tag{3.8}$$

The Δ/σ_{cc} distribution is found for different multiplicity bins. If the variations between the default and alternate measurements are purely statistical, the distribution should be a Gaussian with mean = 0 and $\sigma = 1$. Large deviations from the ideal behaviour indicate that the variations are not purely statistical and should be included in the systematic uncertainties. A distribution with σ much less than 1 is still acceptable as long as it is approximately Gaussian and the mean is nearly 0.

Parameter	Default	Variation-1	Variation-2
$\|V_z\|$ (cm)	10	8	-
$\|DCA_{xy}\|$ (cm)	0.2	0.2	-
$\|DCA_z\|$ (cm)	2.0	2.0	1.2
No. of TPC Clusters	70	80	-
Pile up	Cut applied	Cut applied	
FitlterBit	96	768	

Table 3.5: Sources of systematic uncertainties pp collisions at $\sqrt{s} = 5.02$ TeV.

The sources considered in the Barlow test are the $|V_z|$ position of primary vertex, the distance of the closest approach in both longitudinal and transverse directions, the total number of TPC

clusters, the applicable pile-up cut and the track quality check for all collision systems. In addition to that, magnetic polarity has also been included in the case of Pb–Pb collisions. All sets of default sources and their variations along with their values for Pb–Pb and Xe–Xe collisions are listed in table 3.4 and for pp collisions in table 3.5.

Figure 3.11 shows the distribution of Δ/σ_{cc} for the $DCA_{xy} < 0.8$ (left), and $n_{\text{cluster}} > 80$ (right), for Pb–Pb collisions at $\sqrt{s_{\text{NN}}} = 5.02$ TeV.

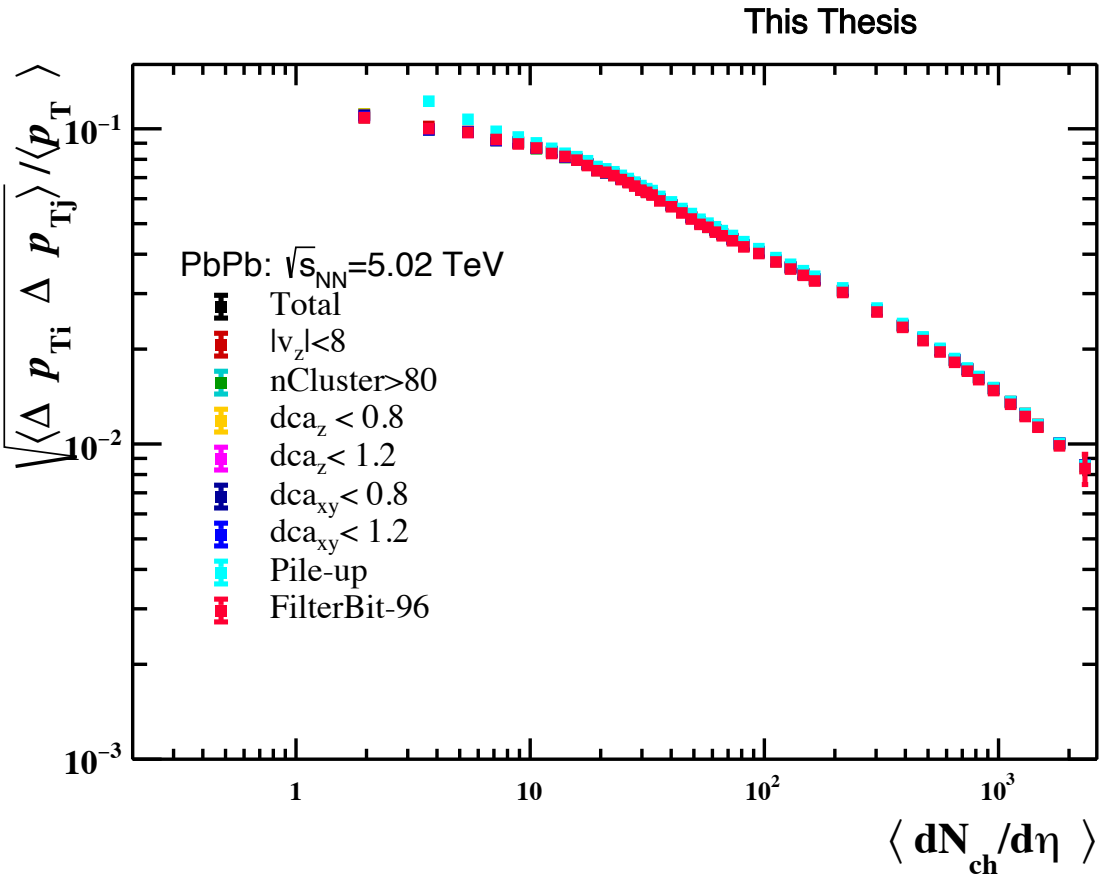

Figure 3.12: The relative non-statistical fluctuation of mean transverse momentum $\sqrt{\langle \Delta p_{\text{Ti}} \Delta p_{\text{Tj}} \rangle}/\langle\langle p_{\text{T}} \rangle\rangle$ as a function of $\langle \mathrm{d}N_{\text{ch}}/\mathrm{d}\eta \rangle$ for Pb–Pb collisions at $\sqrt{s_{\text{NN}}} = 5.02$ TeV corresponding to various systematic sources.

The mean of the distribution for $DCA_{xy} < 0.8$, is very close to zero and the standard deviation is less than one. In this case, the source obeys the Barlow criteria and hence gives a near Gaussian distribution. As the alternate measurement $DCA_{xy} < 0.8$, qualifies the Barlow criteria, it has been rejected as a potential contributor in the estimation of systematic uncertainties. On

the contrary, the mean and standard deviation of $n_{\text{cluster}} > 80$ variation, are way greater than 0 and 1 respectively (Fig. 3.11). This source is hence considered for the systematic error calculation. The distributions of Δ/σ_{cc} for the variations of the considered sources are obtained for all the collision systems used in both analyses and were checked if they pass the Barlow criteria.

The red and orange shaded cells in Tab. 3.4 show the variations that passed the Barlow checks in Pb–Pb and Xe–Xe collisions, respectively. The rest of the sources are considered for the determination of systematic uncertainties. For pp collisions, all the sources are used for systematic uncertainty calculations.

The systematic uncertainty calculation is done using the maximum deviation method for all the systems. In the maximum deviation method, systematic uncertainty is estimated by identifying the largest discrepancy or deviation between measurements. In this method, the default and the alternate value of the correlator are found for each source across the measured multiplicity bin. For each source, the absolute difference of the variations (var_{n1} and var_{n2}) from the default (Val) is calculated. The largest deviation among the variations within the source is identified (S_n).

$$S_n = max(|Val - var_{n1}|, |Val - var_{n2}|) \tag{3.9}$$

The total systematic uncertainty of a bin, Sys_{err}, is calculated by the quadrature sum of the maximum value of the deviation between the default and variation coming from all the sources considered (S_n). The equation is given by:

$$Sys_{err} = \sqrt{\sum_{n=1}^{N} S_n^2}, \tag{3.10}$$

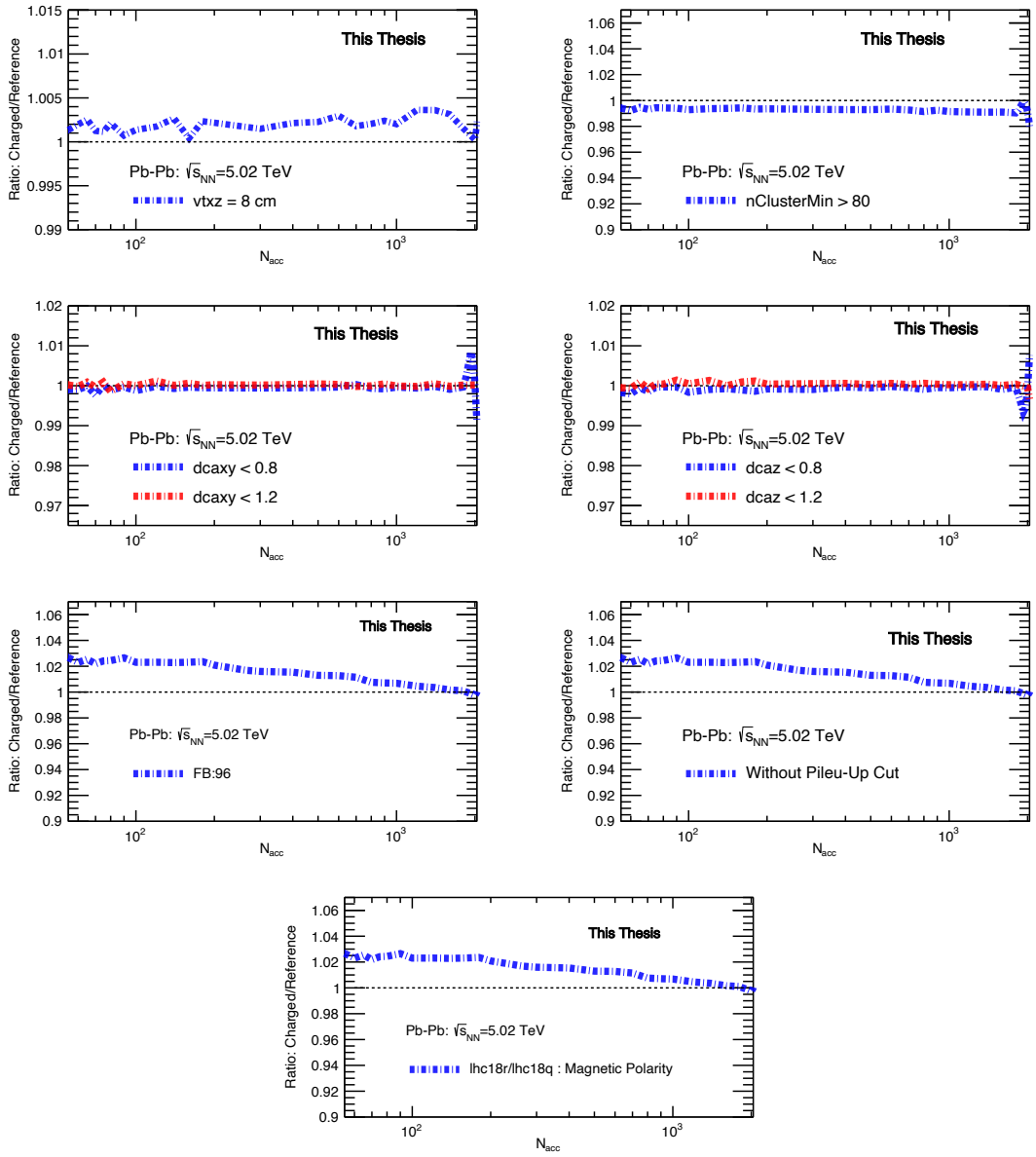

Figure 3.13: Ratio of $\sqrt{\langle \Delta p_{\mathrm{Ti}} \Delta p_{\mathrm{Tj}} \rangle} / \langle \langle p_{\mathrm{T}} \rangle \rangle$ from different sources with default values for Pb–Pb collisions at $\sqrt{s_{\mathrm{NN}}} = 5.02$ TeV.

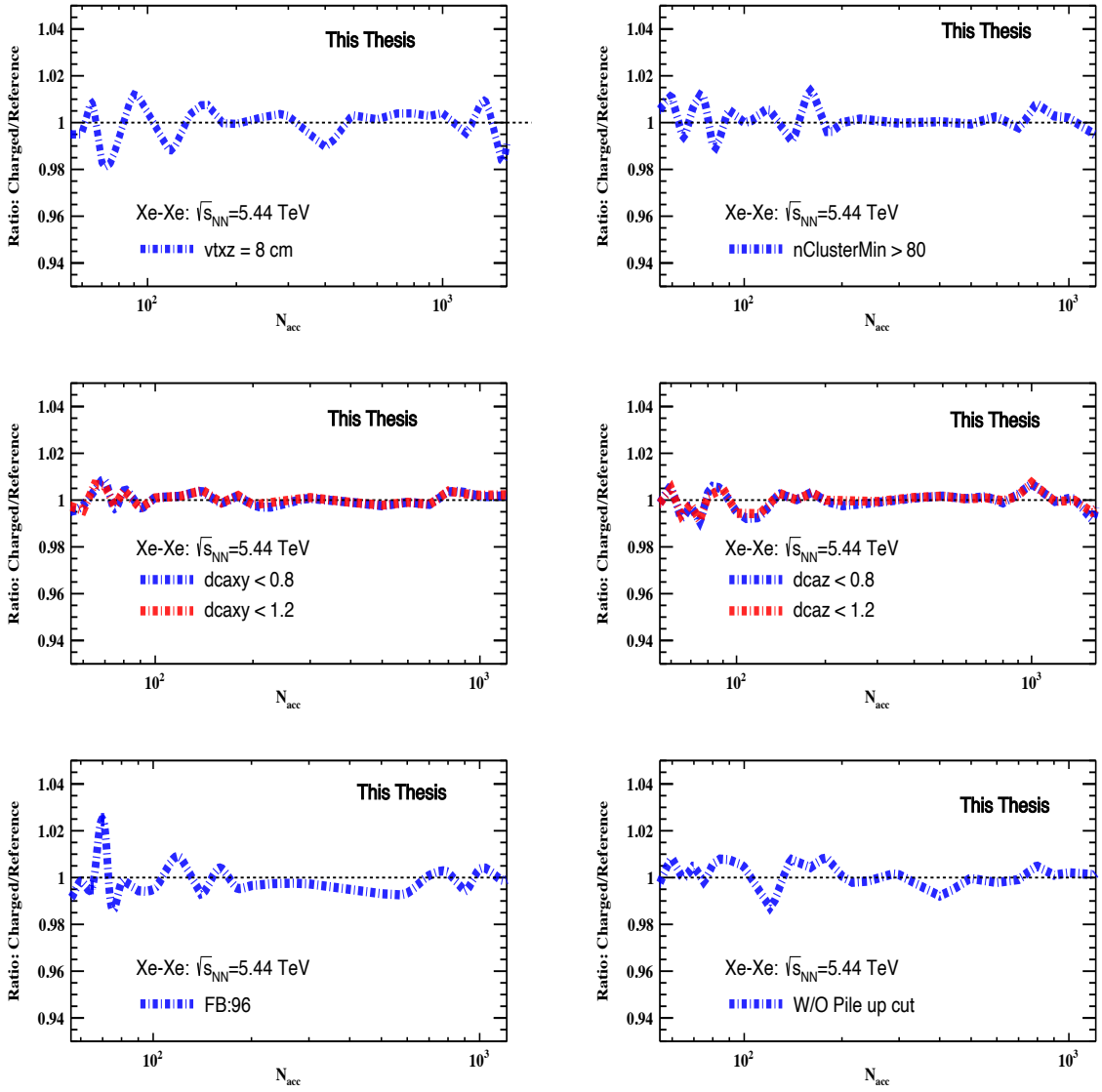

Figure 3.14: Ratio of $\sqrt{\langle \Delta p_{\mathrm{Ti}} \Delta p_{\mathrm{Tj}} \rangle} / \langle \langle p_{\mathrm{T}} \rangle \rangle$ from different sources with default values for Xe–Xe collisions at $\sqrt{s_{\mathrm{NN}}}$ =5.44 TeV

The fluctuation of mean transverse momentum, $\sqrt{\langle \Delta p_{\mathrm{Ti}} \Delta p_{\mathrm{Tj}} \rangle} / \langle \langle p_{\mathrm{T}} \rangle \rangle$, corresponding to various systematic sources for Pb–Pb collisions at $\sqrt{s_{\mathrm{NN}}}$ = 5.02 TeV has been shown as a function of $\langle \mathrm{d}N_{\mathrm{ch}}/\mathrm{d}\eta \rangle$ in figure 3.12. Variations of different sources are taken into consideration to be compared with the default sets of cuts used in the analysis. Figs. 3.13, 3.14 and 3.15 show the ratio of the changed to the default value of correlator, $\sqrt{\langle \Delta p_{\mathrm{Ti}} \Delta p_{\mathrm{Tj}} \rangle} / \langle \langle p_{\mathrm{T}} \rangle \rangle$ for all the sources in Pb–Pb, Xe–Xe and pp collisions, respectively.

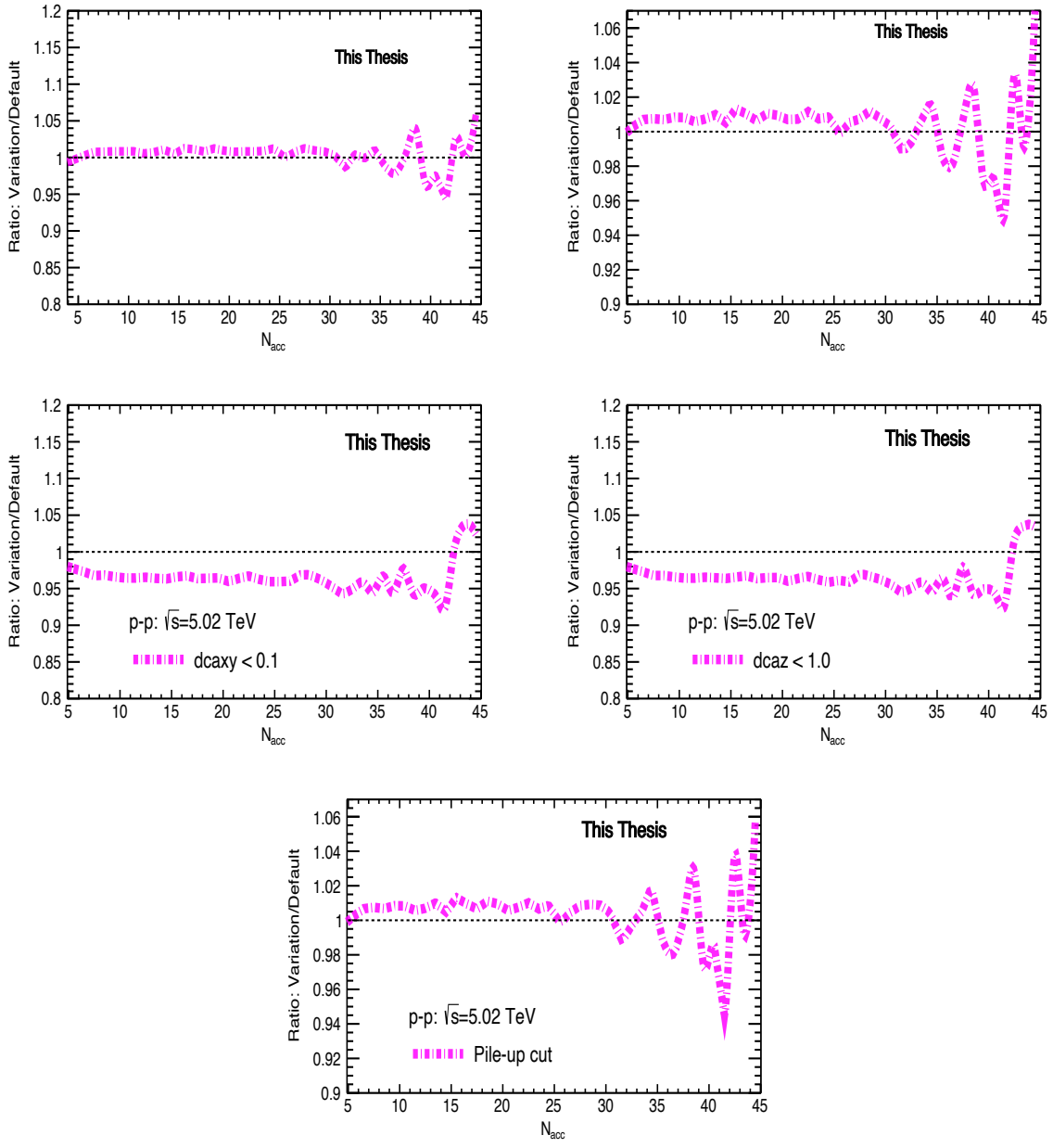

Figure 3.15: Ratio of $\sqrt{\langle \Delta p_{\mathrm{Ti}} \Delta p_{\mathrm{Tj}} \rangle} / \langle \langle p_{\mathrm{T}} \rangle \rangle$ from different sources with default values for pp collisions at $\sqrt{s}$ = 5.02 TeV

The relative percentage error for each of the considered sources is found for all collision systems. The total relative percentage error from all sources is the square root of the quadrature sum of the individual errors of the sources considered. The relative uncertainty for Pb–Pb collisions at $\sqrt{s_{\mathrm{NN}}}$ = 5.02 TeV, Xe–Xe collisions at $\sqrt{s_{\mathrm{NN}}}$ = 5.44 TeV and pp collision at $\sqrt{s}$ = 5.02 TeV from various systematic sources are shown in figure 3.16 (left and right) and

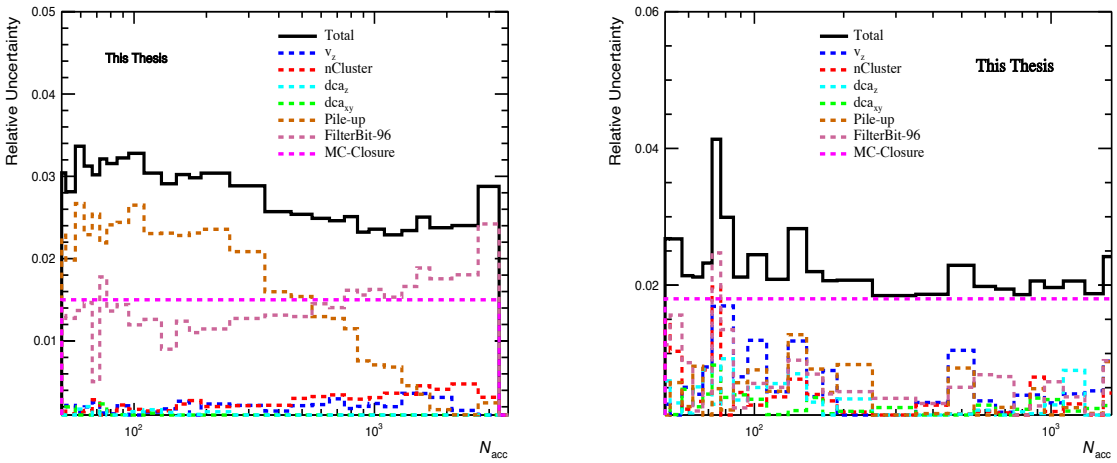

Figure 3.16: The relative uncertainty for Pb–Pb collisions at $\sqrt{s_{\rm NN}}$ = 5.02 TeV (left) and Xe–Xe collisions at $\sqrt{s_{\rm NN}}$ = 5.44 TeV (right) from various systematic sources.

3.17 respectively. At the event level, selection criteria considered include the accepted vertex-z position (v_z) along the beam axis, and selection criteria used to suppress contributions from event pile-up. Vertex-z (v_z) selection contributes uncertainties smaller than 2.1% for pp collisions, 3.7% for Xe–Xe collisions and 2.2% in Pb–Pb collisions. The relative uncertainties due to event pile-up are less than 2% and 3.3% for pp and Xe–Xe collisions respectively and vary from a minimum of 0.1 to a maximum 3.5% for Pb–Pb collisions. At the track level, selected quality cuts are varied including the longitudinal and transverse DCA of each track and the minimum number of TPC clusters required on a track. The maximum contribution to relative systematic uncertainty due to the track selection criteria arises from DCA_z selection, which is < 5.5%. Similarly, the maximum contributions to relative percentage uncertainty from the track selection, are 2.2% from TPC clusters and 0.8% from DCA_z selection for Xe–Xe and Pb–Pb collisions, respectively. The total systematic uncertainties from all the sources are smaller than 7.1%, 6.7% and 3.8% for pp, and Pb-Pb collisions, respectively. A summary of the relative systematic uncertainties assessed for the three collision systems is presented in Table 3.6.

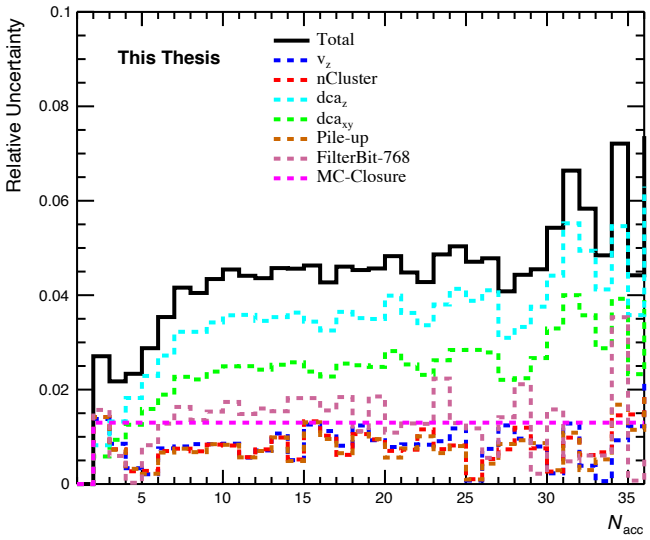

Figure 3.17: The relative uncertainty for pp collisions at $\sqrt{s}$ = 5.02 TeV from various systematic sources.

3.7.3 Estimation of $\langle dN_{ch}/d\eta \rangle$ from $\langle N_{acc} \rangle$

The results for the strength of the correlator, $\sqrt{\langle \Delta p_{Ti} \Delta p_{Tj} \rangle}/\langle\langle p_T \rangle\rangle$, are presented, with a focus on their dependence on the average charged-particle multiplicity density, $\langle dN_{ch}/d\eta \rangle$. It is important to note that $\langle dN_{ch}/d\eta \rangle$ has been meticulously corrected for detector effects, making them highly suitable for comparisons with results from other experiments and/or theoretical models. In the present analysis, $\sqrt{\langle \Delta p_{Ti} \Delta p_{Tj} \rangle}/\langle\langle p_T \rangle\rangle$, was calculated as a function of the mean of the number of accepted charged tracks, $\langle N_{acc} \rangle$. These values vary from system to system and depend on event and track selection criteria.

The ALICE findings, regarding $\langle dN_{ch}/d\eta \rangle$ across various collision centrality ranges serve as the basis for this analysis for both Pb–Pb and Xe–Xe collisions. These findings establish a correlation between the current measurements of computing $\langle N_{acc} \rangle$ with $\langle dN_{ch}/d\eta \rangle$, within equivalent centrality intervals-specifically, spanning from 0–2.5%, 2.5–5%, 5-7.5 %, 7.5-10 % and progressing in 10% increments from 10–20% to 70–80%, within the kinematic ranges of $|\eta| < 0.8$ and 0.15 GeV/c $< p_T <$ 2 GeV/c to maintain consistency with the physics of the study. Table 3.7 shows the values of $\langle dN_{ch}/d\eta \rangle$, $\langle N_{part} \rangle$ obtained from previous measurements of

Source of uncertainty	pp, 5.02 TeV	Xe-Xe, 5.44 TeV	Pb-Pb, 5.02 TeV
Vertex selection	< 2.1%	< 3.7%	< 2.2%
Pile-up	< 2.0%	< 3.3%	0.1–3.5%
No. of TPC clusters	0.1– 2.0%	< 2.2 %	< 0.5%
DCA_{xy}	0.2– 4.0%	< 1.5 %	< 0.3%
DCA_{z}	3.1– 5.5%	< 3.1 %	< 0.8%
MC non-closure	1.3%	1.8%	1.5%
Total	4.0–7.1 %	1.8–6.7%	2.2–3.8 %

Table 3.6: Contributions to the relative (%) systematic uncertainty on $\sqrt{\langle \Delta p_{T,1} \Delta p_{T,2} \rangle}/p_T$ of primary charged particles in pp and Pb–Pb collisions at $\sqrt{s_{NN}}$ = 5.02 TeV and Xe–Xe collisions at 5.44 TeV. Although the systematic uncertainties depend on multiplicity, for illustration, the values in the table correspond to the range of relative systematic uncertainty for all three collision systems. The individual contributions are summed in quadrature to obtain the total uncertainty.

ALICE, and $\langle N_{acc} \rangle$, as obtained in this analysis in different centrality ranges for Pb–Pb collision at $\sqrt{s_{NN}}$ = 5.02 TeV.

The mapping of $\langle dN_{ch}/d\eta \rangle$ with $\langle N_{acc} \rangle$ is performed for both Pb–Pb and Xe–Xe collisions. The left panel of Fig. 3.18 shows the variation of $\langle dN_{ch}/d\eta \rangle$ with $\langle N_{acc} \rangle$ for Pb–Pb collisions at $\sqrt{s_{NN}}$ = 5.02 TeV. As anticipated, a consistent linear correlation is evident across the entire centrality range being examined, enabling the estimation of $\langle dN_{ch}/d\eta \rangle$ for any given $\langle N_{acc} \rangle$ value through interpolation. The functional form of the fitting function is given by,

$$\left\langle \frac{dN_{ch}}{d\eta} \right\rangle = p_0 + p_1 \times \langle N_{acc} \rangle. \tag{3.11}$$

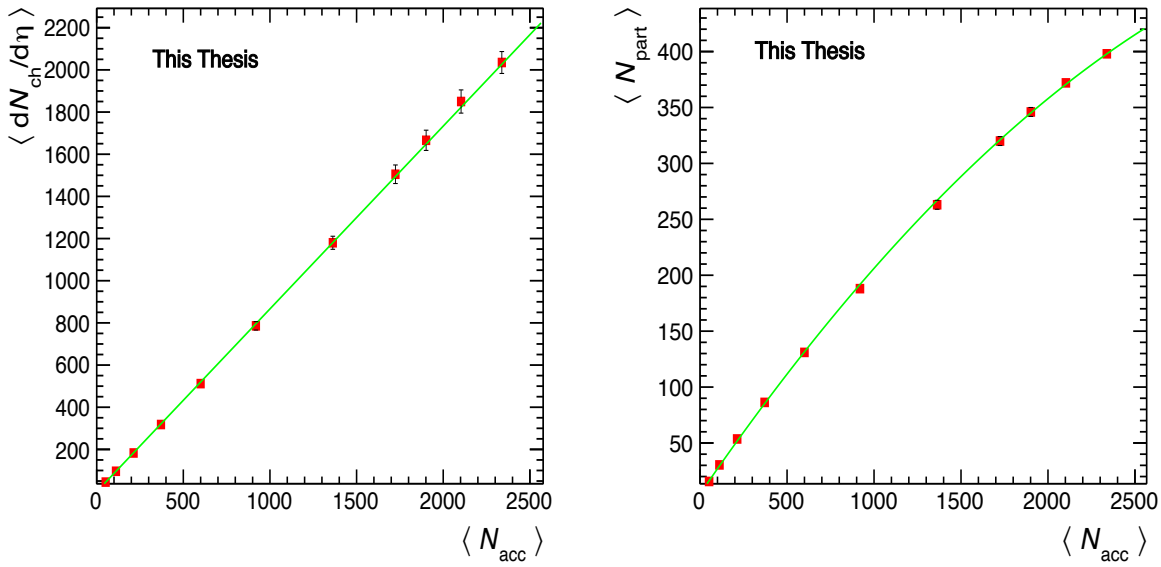

Figure 3.18: $\langle \mathrm{d}N_{\mathrm{ch}}/\mathrm{d}\eta \rangle$ as a function of $\langle N_{\mathrm{acc}} \rangle$ (left) and $\langle N_{\mathrm{part}} \rangle$ as a function of $\langle N_{\mathrm{acc}} \rangle$ (right) in Pb–Pb collisions at $\sqrt{s_{\mathrm{NN}}}$ = 5.02 TeV.

The extracted parameters from the fit (p_0= 0.87 and p_1= 0.68) are used to obtain the corresponding $\langle dN_{\mathrm{ch}}/d\eta \rangle$. The results are then presented in terms of $\langle \mathrm{d}N_{\mathrm{ch}}/\mathrm{d}\eta \rangle$ for Pb-Pb collision. The results for Xe–Xe and pp collisions are presented as a function of $\langle \mathrm{d}N_{\mathrm{ch}}/\mathrm{d}\eta \rangle$, whose values are obtained in a similar manner as Pb–Pb collisions.

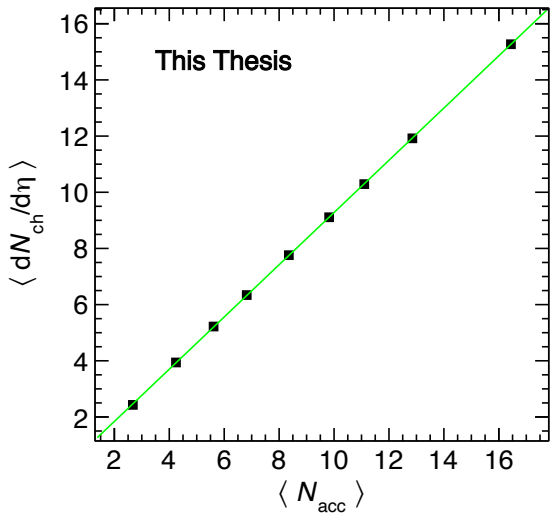

Figure 3.19: variation of $\langle \mathrm{d}N_{\mathrm{ch}}/\mathrm{d}\eta \rangle$ as a function of N_{acc} for pp collisions at $\sqrt{s}$ = 5.02 TeV

Table 3.7: Values of $\langle dN_{ch}/d\eta \rangle$ and $\langle N_{part} \rangle$ for Pb-Pb collisions at $\sqrt{s_{NN}}$ = 5.02 TeV [136] and the obtained $\langle N_{acc} \rangle$ values corresponding to the centrality bin.

Centrality	$\langle dN_{ch}/d\eta \rangle$	$\langle N_{part} \rangle$	$\langle N_{acc} \rangle$
0%-2.5%	2035 ± 52	398 ± 2	2338.25
2.5%-5.0%	1850 ±55	372 ± 3	2103.08
5.0%-7.5%	1666 ± 48	346 ± 4	1901.36
7.5%-10%	1505 ±44	320 ± 4	1724.24
10%-20%	1180± 31	263 ± 4	2103.08
20%-30%	786±20	188 ± 3	1901.36
30%-40%	512± 15	131 ± 2	1724.24
40%-50%	318±12	86.3 ± 1.7	1362.81
50%-60%	183± 8	53.6 ± 1.2	919.046
60%-70%	96.3± 5.8	53.6 ± 0.8	599.855
70%-80%	44.9± 3.4	15.6 ± 0.3	371.085

Table 3.8 shows the $\langle dN_{ch}/d\eta \rangle$ and $\langle N_{acc} \rangle$ values relative to their respective multiplicity percentile for pp collision at $\sqrt{s}$=5.02 TeV. Figure 3.19 shows the variation of $\langle dN_{ch}/d\eta \rangle$ as a function of $\langle N_{acc} \rangle$ for pp collision at $\sqrt{s}$=5.02 TeV.

Table 3.8: Multiplicity estimation using V0M multiplicity estimator in pp collisions at $\sqrt{s}$ = 5.02 TeV [137].

Mult(%)	$\langle dN_{ch}/d\eta \rangle$	$\langle N_{acc} \rangle$
0-5	15.48	16.44
5-10	12.07	12.85
10-15	10.40	11.09
15-20	9.17	9.82
20-30	7.76	8.35
30-40	6.30	6.82
40-50	5.16	5.61
50-70	3.90	4.24
70-100	2.38	2.67

The results in this thesis are also presented as a function of number of participant nucleons. The $\langle N_{part} \rangle$ was also estimated by the similar procedure implemented for $\langle dN_{ch}/d\eta \rangle$.

Chapter 4

Experimental observations of event-by-event fluctuations of $\langle p_{\mathrm{T}} \rangle$ measurement

In this chapter, the results of relative fluctuations of $\langle p_{\mathrm{T}} \rangle$ measurement as a function of charge particle multiplicity density, $\langle \mathrm{d}N_{\mathrm{ch}}/\mathrm{d}\eta \rangle$, are discussed. The strength of the correlator has been represented according to section 3.4.The observations in pp, Xe–Xe and Pb–Pb collisions are presented in Sec. 4.1.1. The system size dependence and the collision energy dependence of the correlator, and its comparison with the models have been studied. Furthermore, Sec. 4.2 discusses the results in pp collisions for different spherocity classes. The spherocity-dependent study is carried out for pp collisions in $\sqrt{s}$ = 5.02 and 13 TeV. Error bars and boxes are used to highlight the statistical and systematic uncertainties of the measurements, respectively in the figures.

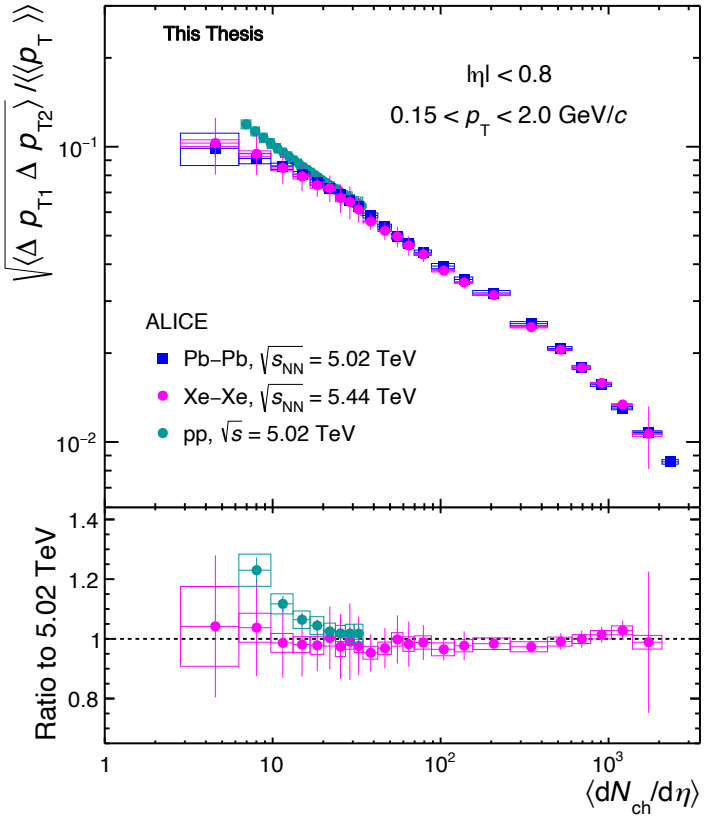

Figure 4.1: Upper panel: The variation of $\sqrt{\langle \Delta p_{\mathrm{T},1} \Delta p_{\mathrm{T},2} \rangle}/\langle\langle p_{\mathrm{T}} \rangle\rangle$ with $\langle \mathrm{d}N_{\mathrm{ch}}/\mathrm{d}\eta \rangle$ in $|\eta| < 0.8$ for pp collisions at $\sqrt{s} = 5.02$ TeV, Xe–Xe collisions at $\sqrt{s_{\mathrm{NN}}} = 5.44$ TeV and Pb–Pb collisions at $\sqrt{s_{\mathrm{NN}}} = 5.02$ TeV; Lower panel: Ratio of $\sqrt{\langle \Delta p_{\mathrm{T},1} \Delta p_{\mathrm{T},2} \rangle}/\langle\langle p_{\mathrm{T}} \rangle\rangle$ in pp and Xe–Xe collisions to that of Pb–Pb collisions.

4.1 $\langle p_{\mathrm{T}} \rangle$ fluctuations in pp, Xe–Xe and Pb–Pb collisions

4.1.1 System size dependence of event-by-event $\langle p_{\mathrm{T}} \rangle$ fluctuations

The top panel of Fig. 4.1 shows the strength of $\sqrt{\langle \Delta p_{\mathrm{T},1} \Delta p_{\mathrm{T},2} \rangle}/\langle\langle p_{\mathrm{T}} \rangle\rangle$ measured as a function of the mean charged particle multiplicity density, determined in the pseudorapidity range $|\eta| < 0.8$ for pp collisions at $\sqrt{s} = 5.02$ TeV, Xe–Xe collisions at $\sqrt{s_{\mathrm{NN}}} = 5.44$ TeV, and Pb–Pb collisions at $\sqrt{s_{\mathrm{NN}}} = 5.02$ TeV. The strength of $\sqrt{\langle \Delta p_{\mathrm{T},1} \Delta p_{\mathrm{T},2} \rangle}/\langle\langle p_{\mathrm{T}} \rangle\rangle$ is evidently non-vanishing and exhibits an approximate power law dependence on the produced charged particle density. The fluctuations of the event-wise $\langle p_{\mathrm{T}} \rangle$ are observed to be non-Poissonian and exhibit a strong

dependence on the charged particle density for all three collision systems. These new results confirm and corroborate prior observations of non-Poissionian fluctuations in A–A collisions and make it possible to carry out a detailed study of the system size and energy dependence of the fluctuations.

The magnitude of the correlator is observed to decrease by more than one order of magnitude as the produced particle multiplicity measured in Xe–Xe and Pb–Pb collisions, increases from peripheral to most central collisions. In the context of proton-proton (pp) collisions, the correlator exhibits a consistent decrease from low to high multiplicity.

One notes, however, that this multiplicity dependence cannot be described by a single power law across the whole range of particle production in Pb–Pb and Xe–Xe collisions. It is observed that, in both Pb–Pb (blue square) and Xe–Xe (magenta circle) collisions, the dependence can be characterized by three power-law regimes with distinct slopes in the ranges, $3 < \langle \mathrm{dN_{ch}}/\mathrm{d}\eta \rangle < 20$, $20 < \langle \mathrm{dN_{ch}}/\mathrm{d}\eta \rangle < 300$ and $300 < \langle \mathrm{dN_{ch}}/\mathrm{d}\eta \rangle$. This suggests that the strength of the correlation is influenced by distinct mechanisms of particle production (or system properties) from the most peripheral to the most central collisions.

The lower panel of Fig. 4.1 displays the evolution of the ratio of the correlator measured in pp and Xe–Xe collisions relative to those observed in Pb–Pb collisions. One observes that the magnitude of the correlators measured in Pb–Pb and Xe–Xe collisions are nearly identical and feature essentially similar $\langle \mathrm{d}N_{\mathrm{ch}}/\mathrm{d}\eta \rangle$ evolution. However, the evolution of the correlator strength measured in pp collisions clearly differs from that observed in the larger systems. Although, at the largest $\langle \mathrm{d}N_{\mathrm{ch}}/\mathrm{d}\eta \rangle$ observed in pp collisions, the correlator strength is identical, within statistical uncertainties, to that observed in Pb–Pb and Xe–Xe collisions at the same density, one finds that for lower values of $\langle \mathrm{d}N_{\mathrm{ch}}/\mathrm{d}\eta \rangle$, the correlation strength progressively deviates from that observed in the larger systems. Overall, one finds that the evolution of $\sqrt{\langle \Delta p_{\mathrm{T},1} \Delta p_{\mathrm{T},2} \rangle}/\langle \langle p_{\mathrm{T}} \rangle \rangle$ with $\langle \mathrm{d}N_{\mathrm{ch}}/\mathrm{d}\eta \rangle$ follows similar trend in Pb–Pb and Xe–Xe collisions, but a rather different trend in pp collisions.

The evolution of $\sqrt{\langle \Delta p_{\mathrm{T},1} \Delta p_{\mathrm{T},2} \rangle}/\langle \langle p_{\mathrm{T}} \rangle \rangle$ with respect to $\langle \mathrm{dN_{ch}}/\mathrm{d}\eta \rangle$ is compared against computational models in Fig. 4.2. Specifically, the comparisons are made for Pb–Pb and Xe–

Xe collisions, utilizing the HIJING model [126] and two different models of AMPT model calculations [138]. In the AMPT calculations, both the default mode and "string melting " modes are used for comparisons with the data.

In the lower panels of Fig. 4.2, one can observe the ratios of the results obtained from the HIJING and AMPT models to the measured data. Notably, the magnitude of $\sqrt{\langle \Delta p_{\mathrm{Ti}} \Delta p_{\mathrm{Tj}} \rangle}/\langle\langle p_{\mathrm{T}} \rangle\rangle$ calculated using HIJING displays a simple power-law behavior, which is described by, $\sqrt{\langle \Delta p_{\mathrm{Ti}} \Delta p_{\mathrm{Tj}} \rangle}/\langle\langle p_{\mathrm{T}} \rangle\rangle \propto \langle \mathrm{dN_{ch}}/\mathrm{d}\eta \rangle^{\alpha}$, with α = -0.504, accompanied by a small uncertainty of 0.007. This relationship holds within an interval of $25 < \langle \mathrm{dN_{ch}}/\mathrm{d}\eta \rangle < 2500$.

The observed power law dependence and the obtained exponent value are in line with the behavior expected for a system composed of a simple superposition of nucleon-nucleon collisions, as modelled by HIJING [126]. However, it is worth noting that while the correlator's evolution measured in both Pb–Pb and Xe–Xe collisions approximately adheres to the power-law fit within the range of $10 < \langle \mathrm{dN_{ch}}/\mathrm{d}\eta \rangle < 50$, a noticeable deviation from this simple trend becomes evident for $\langle \mathrm{dN_{ch}}/\mathrm{d}\eta \rangle > 50$. This departure from the expected behavior is also emphasized by examining the ratio of the correlator in Pb–Pb collisions at $\sqrt{s_{\mathrm{NN}}}$ = 5.02 TeV and Xe–Xe collisions at $\sqrt{s_{\mathrm{NN}}}$ = 5.44 TeV to the power-law fit of $\langle p_{\mathrm{T}} \rangle$ fluctuations from the HIJING model, as depicted in Fig. 4.3.

These observations collectively suggest that the final state particle production in Pb–Pb collisions at $\sqrt{s_{\mathrm{NN}}}$ = 5.02 TeV and Xe–Xe at $\sqrt{s_{\mathrm{NN}}}$ = 5.44 TeV cannot be adequately described by a simple superposition of independent particle-emitting sources. These findings further support earlier findings made by the ALICE collaboration in Pb–Pb collisions at $\sqrt{s_{\mathrm{NN}}}$ = 2.76 TeV [85] and by the STAR collaboration at RHIC energies [76, 80].

Deviations from a superposition of independent particle-emitting sources, in A–A collisions, are evidently known to arise from measurements of nuclear modification factor [139], measurements of anisotropic flow [140], and other measurements of two-particle correlation functions [141, 142]. Consequently, it is reasonable to seek theoretical insights from models such as AMPT, which have demonstrated some success in replicating experimental data from RHIC and LHC.

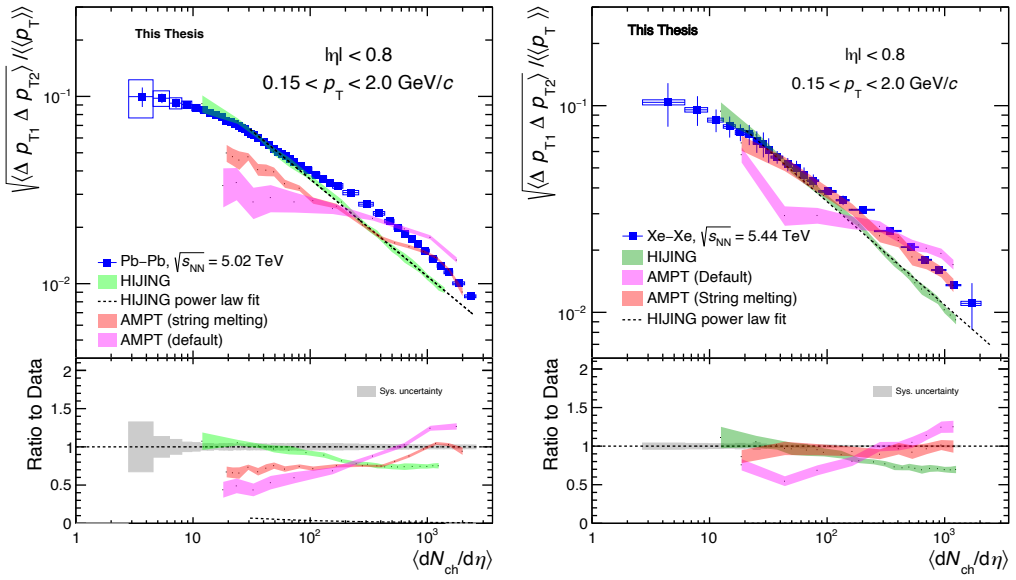

Figure 4.2: Upper panels: Comparisons of the evolution of the $\sqrt{\langle \Delta p_{\mathrm{T},1} \Delta p_{\mathrm{T},2} \rangle}/\langle\langle p_{\mathrm{T}} \rangle\rangle$ with $\langle \mathrm{d}N_{\mathrm{ch}}/\mathrm{d}\eta \rangle$ in Pb–Pb collisions at $\sqrt{s_{\mathrm{NN}}}$ = 5.02 TeV (left) and Xe–Xe collisions at $\sqrt{s_{\mathrm{NN}}}$ = 5.44 TeV (right) with estimations from HIJING and AMPT models. Lower panels: Ratio of the the model calculations to the measured data. Solid symbols represent the measured data reported in this work with statistical (vertical bars) and systematic (boxes) uncertainties. Model calculations are shown with shaded bands denoting their statistical uncertainty.

Figure 4.2 shows the predictions of the two different versions of the AMPT model and it can be observed that the AMPT estimations consistently underestimate the strength of the $\sqrt{\langle \Delta p_{\mathrm{T},1} \Delta p_{\mathrm{T},2} \rangle}/\langle\langle p_{\mathrm{T}} \rangle\rangle$ in peripheral collisions. Although these calculations exhibit an approximate power-law dependence on $\langle \mathrm{dN_{ch}}/\mathrm{d}\eta \rangle$, this behavior significantly diverges from the evolution observed in Pb–Pb and Xe–Xe collisions. Consequently, it appears that both the HIJING and AMPT models lack certain crucial features necessary for accurately describing the evolution of $\sqrt{\langle \Delta p_{\mathrm{T},1} \Delta p_{\mathrm{T},2} \rangle}/\langle\langle p_{\mathrm{T}} \rangle\rangle$ with respect to collision centrality.

Fig. 4.3 displays the evolution of the ratio of measured(and obtained values from models) and estimated values of $\sqrt{\langle \Delta p_{\mathrm{T},1} \Delta p_{\mathrm{T},2} \rangle}/\langle\langle p_{\mathrm{T}} \rangle\rangle$ by a power law fit to the correlator obtained from HIJING with respect to the charged particle multiplicity density, $\langle \mathrm{dN_{ch}}/\mathrm{d}\eta \rangle$ for both Pb–Pb and Xe–Xe collisions. The fit was carried in the range 20< $\langle \mathrm{dN_{ch}}/\mathrm{d}\eta \rangle$ < 2000 with a fixed

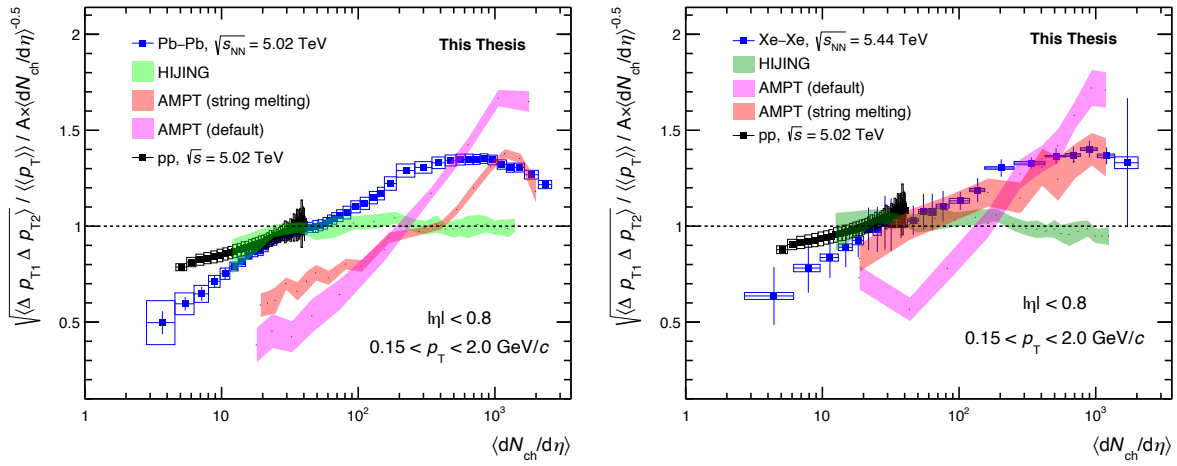

Figure 4.3: Evolution of the ratio $\sqrt{\langle \Delta p_{\mathrm{T},1} \Delta p_{\mathrm{T},2} \rangle} / \langle \langle p_{\mathrm{T}} \rangle \rangle$(measured data and model expectations) to a power law fit to HIJING estimations as a function of $\langle \mathrm{d}N_{\mathrm{ch}}/\mathrm{d}\eta \rangle$ (left) pp and Pb–Pb collisions at $\sqrt{s_{\mathrm{NN}}}$ = 5.02 TeV; (right) pp collisions at $\sqrt{s}$ = 5.02 TeV and Xe–Xe collisions at $\sqrt{s_{\mathrm{NN}}}$ = 5.44 TeV. Solid symbols represent the measured data reported in this work with statistical (vertical bars) and systematic (boxes) uncertainties. Calculations of the ratios obtained with HIJING and AMPT calculations are shown with shaded bands denoting their statistical uncertainty.

value of $\alpha = -0.5$. The shaded green band is approximately centred at unity and shows that the power law fit is a good description of the evolution of the strength of $\sqrt{\langle \Delta p_{\mathrm{T},1} \Delta p_{\mathrm{T},2} \rangle} / \langle \langle p_{\mathrm{T}} \rangle \rangle$ with $\langle \mathrm{dN_{ch}}/\mathrm{d}\eta \rangle$ predicted by HIJING. Indeed, HIJING produces a progressive dilution of the correlator with rising values of $\langle \mathrm{dN_{ch}}/\mathrm{d}\eta \rangle$ as expected. By contrast, one finds that correlations observed in Pb–Pb and Xe–Xe collisions increasingly undershoot the power law fit at small densities while they significantly exceed the fit at charged-particle densities above 100, thereby signalling a considerable departure from a system consisting of a superposition of independent nucleon-nucleon collisions. One additionally finds that both AMPT calculations considerably violate the density scaling. However, pp collisions show scaling behavior at charged-particle multiplicities greater than 10.

Figure 4.4 shows a moderate dependence of $\sqrt{\langle \Delta p_{\mathrm{T},1} \Delta p_{\mathrm{T},2} \rangle} / \langle \langle p_{\mathrm{T}} \rangle \rangle$ on the collision energy for central Pb-Pb collisions when compared between 2.76 and 5.02 TeV. For $\langle \mathrm{dN_{ch}}/\mathrm{d}\eta \rangle <$

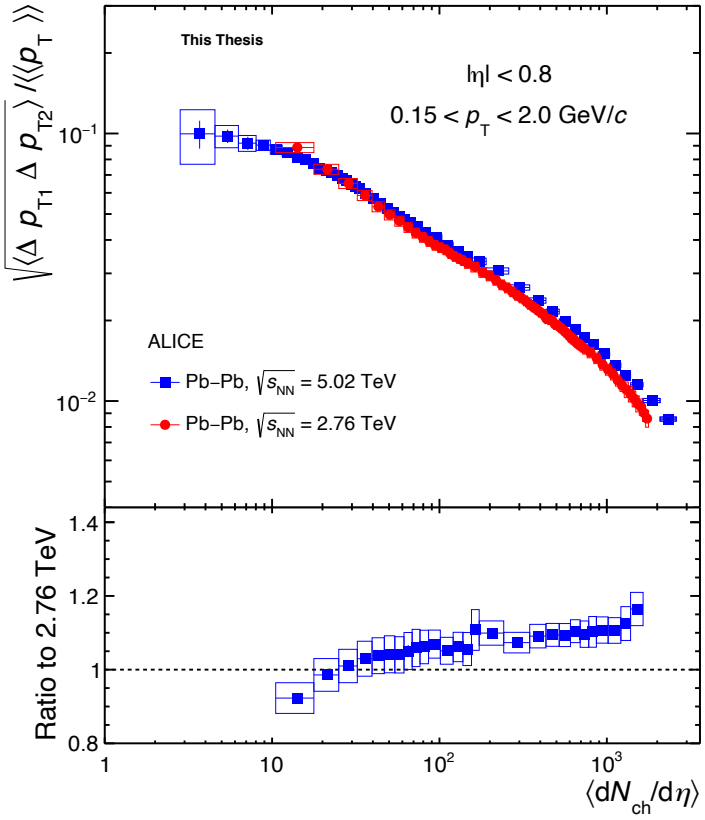

Figure 4.4: The variation of $\sqrt{\langle \Delta p_{\mathrm{T},1} \Delta p_{\mathrm{T},2} \rangle} / \langle\langle p_{\mathrm{T}} \rangle\rangle$ as a function of $\langle \mathrm{d}N_{\mathrm{ch}}/\mathrm{d}\eta \rangle$ for Pb–Pb collisions at $\sqrt{s_{\mathrm{NN}}}$ = 2.76 and 5.02 TeV.

200, the two-particle correlator measured in both the energies are found to be consistent within uncertainties while for higher $\langle \mathrm{dN_{ch}}/\mathrm{d}\eta \rangle$, the correlator measured at $\sqrt{s_{\mathrm{NN}}}$ = 5.02 TeV shows about 20% increase compared to the measurement at 2.76 TeV. However, the dependence on collision energy disappears when the correlator is studied as a function of the mean number of participants, $\langle N_{\mathrm{part}} \rangle$ as shown in the left panel of Fig. 4.5. The bottom panel shows the ratio of the measurements at 5.02 and 2.76 TeV and it is found to be consistent with unity. This suggests that for a given initial-state overlap geometry, the correlator strength is independent of collision energy. The right panel of Fig. 4.5 shows a comparison with Xe–Xe collisions and it can be observed that the values are similar for $\langle N_{\mathrm{part}} \rangle > 25$ when compared to Pb–Pb and Xe–Xe collisions. Therefore, it can be inferred that there is no dependence on system size concerning collision energy for $\langle N_{\mathrm{part}} \rangle > 25$ when the measurement is carried out as a function of the $\langle N_{\mathrm{part}} \rangle$.

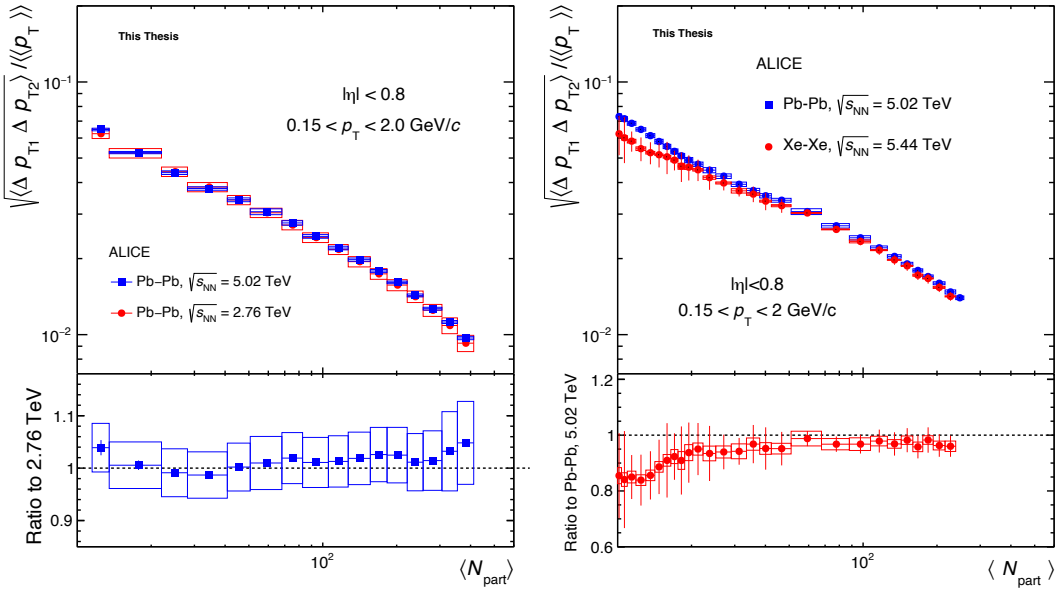

Figure 4.5: Left: The variation of $\sqrt{\langle \Delta p_{T,1} \Delta p_{T,2} \rangle}/\langle\langle p_T \rangle\rangle$ as a function of $\langle N_{part} \rangle$ (mean number of participants) in Pb–Pb collisions at $\sqrt{s_{NN}}$ = 2.76 and 5.02 TeV, right: The variation of $\sqrt{\langle \Delta p_{T,1} \Delta p_{T,2} \rangle}/\langle\langle p_T \rangle\rangle$ as a function of $\langle N_{part} \rangle$ in Xe–Xe collisions at $\sqrt{s_{NN}}$ = 5.44 TeV and Pb–Pb collisions at $\sqrt{s_{NN}}$ = 5.02 TeV.

This might indicate that the strength of correlator is influenced by final state effects at different energies.

4.2 Event shape and multiplicity dependence of $\sqrt{\langle \Delta p_{T,1} \Delta p_{T,2} \rangle}/\langle\langle p_T \rangle\rangle$ in pp collisions

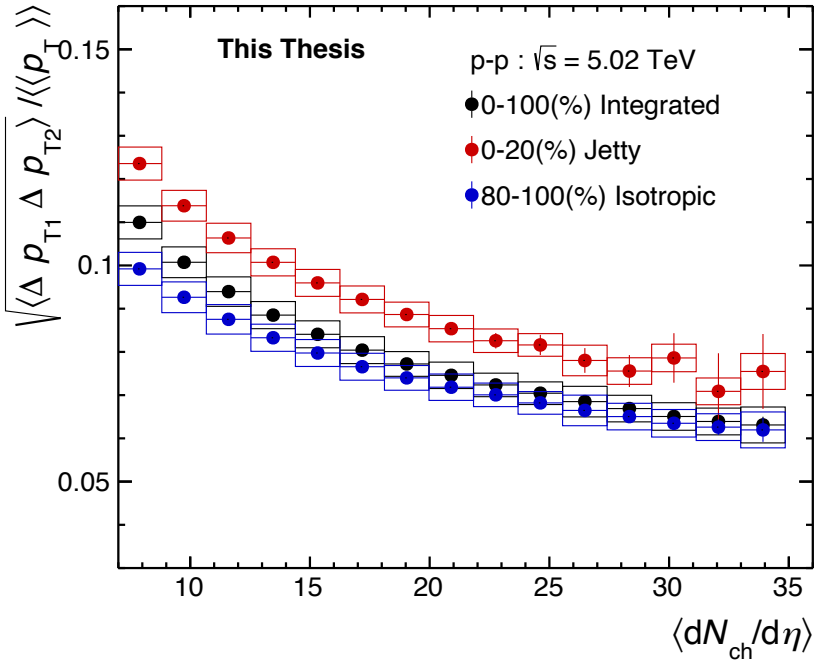

Figure 4.6: Comparison of the evolution of $\sqrt{\langle \Delta p_{T,1} \Delta p_{T,2} \rangle}/\langle\langle p_T \rangle\rangle$ with $\langle dN_{ch}/d\eta \rangle$ in pp collisions at $\sqrt{s}$ = 5.02 TeV for three spherocity classes.

Figures 4.6 and 4.7 present measurements of the evolution of the strength of the correlator $\sqrt{\langle \Delta p_{T,1} \Delta p_{T,2} \rangle}/\langle\langle p_T \rangle\rangle$, with $\langle dN_{ch}/d\eta \rangle$ in pp collisions at $\sqrt{s}$ = 5.02 and 13 TeV for different spherocity classes, respectively. Jetty events exhibit larger $\langle p_T \rangle$ fluctuations than isotropic events for both the energies. The presence of jets systematically enhances the magnitude of the correlator by 20%. As jet particles emitted in a "narrow" cone are strongly correlated on average with other particles, the correlator strength is enhanced significantly by the presence of jets in the events.

It is known that jets (high p_T particles) are quenched (suppressed) in central A–A collisions as discussed in Chapter 1 of the thesis. Thus, fewer particles from jets are expected to be detected as compared to the system without jet quenching. Since jets are suppressed in heavy

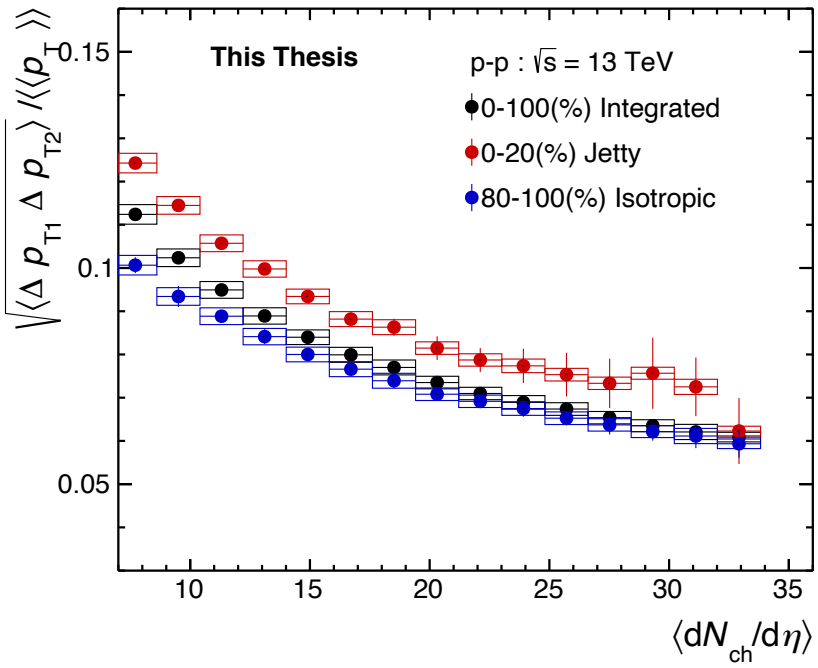

Figure 4.7: Comparison of the evolution of $\sqrt{\langle \Delta p_{T,1} \Delta p_{T,2} \rangle}/\langle\langle p_T \rangle\rangle$ with $\langle dN_{ch}/d\eta \rangle$ in pp collisions at $\sqrt{s}$ = 13 TeV for three spherocity classes.

ion collisions, the correlator, $\sqrt{\langle \Delta p_{T,1} \Delta p_{T,2} \rangle}/\langle\langle p_T \rangle\rangle$, is expected to be reduced relative to power law behaviour.

On the contrary, an increase in the correlator strength for the jetty events relative to the spherocity integrated pp collisions suggest that the results seen in A–A collisions are not driven directly by the suppression of jets. Thus the presence of jets in central A–A collisions are not expected to have a significant contribution to the strength of the correlator.

Figure 4.8 displays the comparison of the evolution of the strength of the correlator $\sqrt{\langle \Delta p_{T,1} \Delta p_{T,2} \rangle}/\langle\langle p_T \rangle\rangle$ with the charged particle density in pp collisions at $\sqrt{s}$ = 5.02 and 13 TeV for jetty, spherocity-integrated and isotropic events and the lower panels show the ratios of the $\sqrt{\langle \Delta p_{T,1} \Delta p_{T,2} \rangle}/\langle\langle p_T \rangle\rangle$ in pp collisions at $\sqrt{s}$ = 13 TeV to $\sqrt{s}$ = 5.02 TeV. The figure shows that the magnitude of $\sqrt{\langle \Delta p_{T,1} \Delta p_{T,2} \rangle}/\langle\langle p_T \rangle\rangle$ in pp collisions at $\sqrt{s}$ = 5.02 TeV is found to be consistent within uncertainties at $\sqrt{s}$ = 13 TeV in both jetty and isotropic events as well as spherocity-integrated events. From the lower panel it can be seen that the values of the correlator obtained in pp collisions at $\sqrt{s}$ =13 TeV for integrated and jetty events are

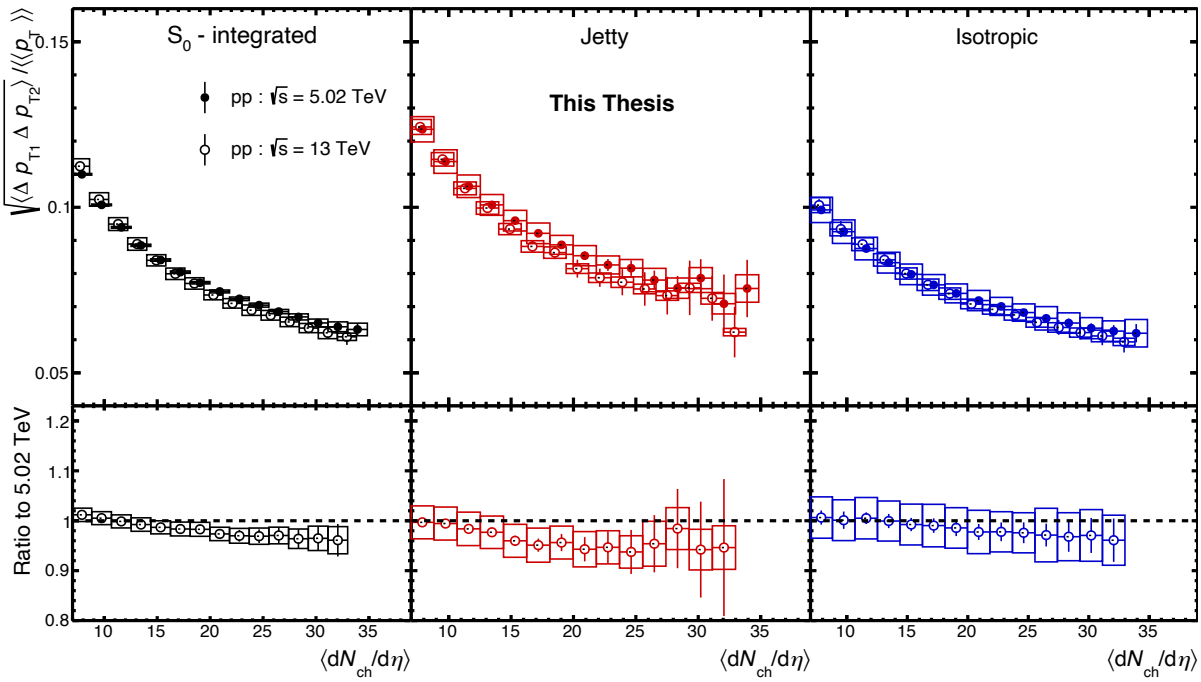

Figure 4.8: Upper panels: Comparison of the evolution of $\sqrt{\langle \Delta p_{T,1} \Delta p_{T,2} \rangle}/\langle\langle p_T \rangle\rangle$ with $\langle dN_{ch}/d\eta \rangle$ in pp collisions at $\sqrt{s}$ = 5.02 and 13 TeV for jetty (left), spherocity-integrated (middle) and isotropic (right) events; Lower panels: Ratio of the $\sqrt{\langle \Delta p_{T,1} \Delta p_{T,2} \rangle}/\langle\langle p_T \rangle\rangle$ in pp collisions at $\sqrt{s}$ = 13 TeV to $\sqrt{s}$ = 5.02 TeV

higher than the values obtained from $\sqrt{s}$ = 5.02 TeV for $\langle dN_{ch}/d\eta \rangle < 15$ and < 10 respectively for integrated and hetty events within uncertainty. However the $\sqrt{\langle \Delta p_{T,1} \Delta p_{T,2} \rangle}/\langle\langle p_T \rangle\rangle$ in isotropic range, agree with each other for both the energies. The $\sqrt{\langle \Delta p_{T,1} \Delta p_{T,2} \rangle}/\langle\langle p_T \rangle\rangle$ shows slightly opposite behaviours as one moves from low to high multiplicity in case of integrated and jetty events. To understand whether the slight energy dependence is due to the values of $\langle p_T \rangle$ at different energies, variation of $\langle \Delta p_{T,1} \Delta p_{T,2} \rangle$ is studied as a function of mean charged particle pseudorapidity density. This is shown in Fig. 4.9. The ratio of $\sqrt{\langle \Delta p_{T,1} \Delta p_{T,2} \rangle}/\langle\langle p_T \rangle\rangle$ as a function of $\langle dN_{ch}/d\eta \rangle$ for pp collisions at $\sqrt{s}$ = 5.02 TeV and 13 TeV shows similar trend as Fig. 4.8, hinting towards the presence of event-wise $\langle p_T \rangle$ fluctuation.

The measured $\sqrt{\langle \Delta p_{T,1} \Delta p_{T,2} \rangle}/\langle\langle p_T \rangle\rangle$ for different spherocity classes have been compared with model predictions from PYTHIA 6 [143], PYTHIA 8 [135], and EPOS-LHC [144] which is shown in Fig. 4.10. The hadronization of quarks in the PYTHIA model is simulated using

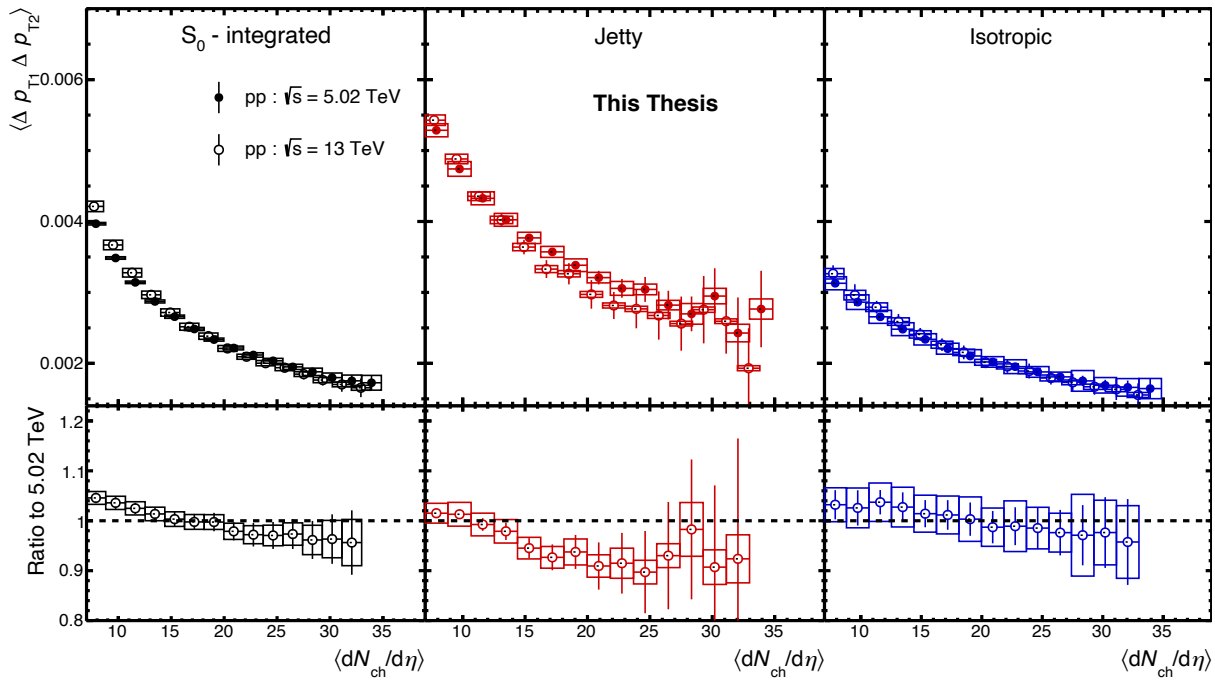

Figure 4.9: Upper panels: Comparison of the evolution of $\langle \Delta p_{T,1} \Delta p_{T,2} \rangle$ with $\langle dN_{ch}/d\eta \rangle$ in pp collisions at $\sqrt{s}$ = 5.02 and 13 TeV for jetty (left), spherocity-integrated (middle) and isotropic (right) events; Lower panels: Ratio of the $\langle \Delta p_{T,1} \Delta p_{T,2} \rangle$ in pp collisions at $\sqrt{s}$ = 13 TeV to $\sqrt{s}$ = 5.02 TeV

the Lund string fragmentation model. Several tunes of PYTHIA have been developed through extensive comparison of Monte Carlo distributions with the minimum-bias measurements from different experiments. PYTHIA 6 Perugia tune includes the revised set of parameters of flavor and fragmentation. This improves the overall description of the Tevatron data and improves the reliability of the extrapolations to the LHC measurements [145]. The minimum bias and underlying event data are taken into account from the LHC in Perugia 2011 tune. PYTHIA 8 Monash tune is tuned to the LHC data and uses an updated set of parameters of hadronization compared to the previous tunes [135]. On the contrary, in the EPOS-LHC model, built on the Parton-Based Gribov Regge Theory, a part of the collision system with high parton densities becomes a "core" region that evolves hydrodynamically and it is surrounded by a more dilute "corona" for which fragmentation occurs in the vacuum. The model is tuned to the LHC data via the colour exchange mechanism of string excitation [144]. PYTHIA 6 significantly underestimates

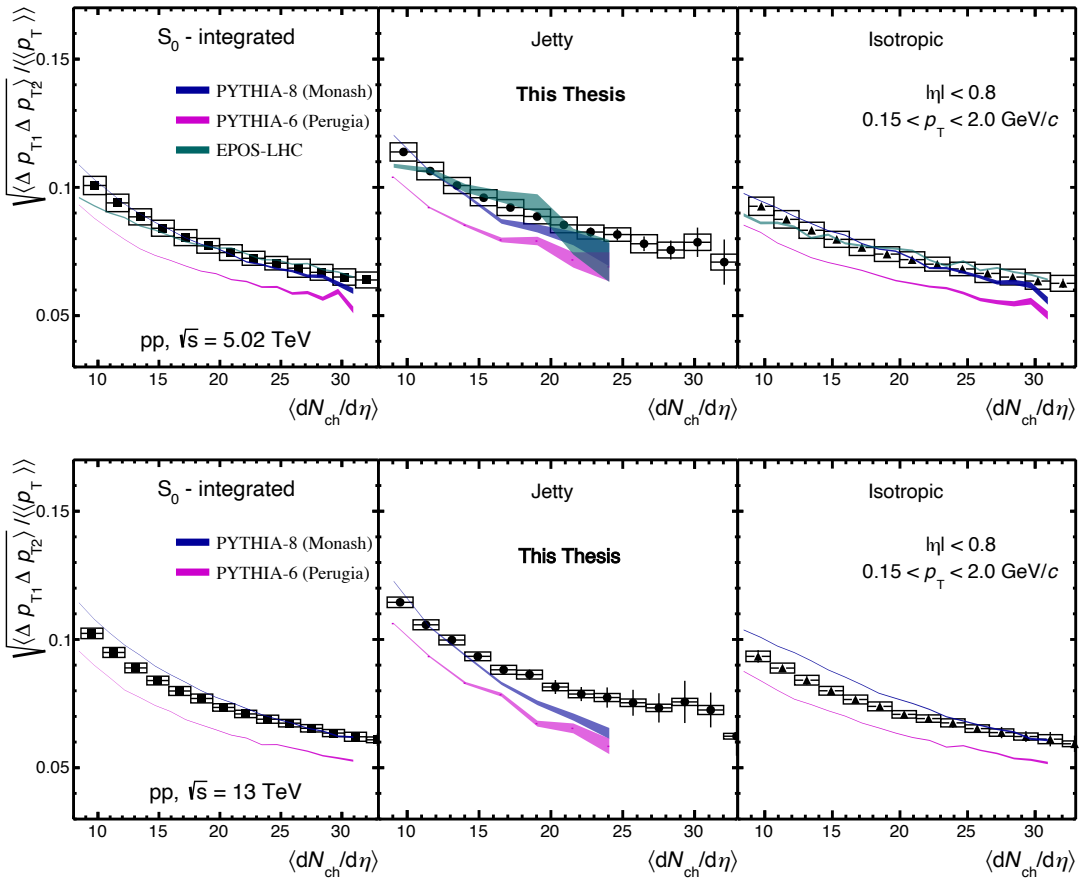

Figure 4.10: Comparison of the evolution of $\sqrt{\langle \Delta p_{T,1} \Delta p_{T,2} \rangle}/\langle\langle p_T \rangle\rangle$ with $\langle dN_{ch}/d\eta \rangle$ in pp collisions at $\sqrt{s}$ = 5.02 TeV(upper panels) and $\sqrt{s}$ = 13 TeV (lower panels) with model predictions for jetty (left), spherocity-integrated (middle), and isotropic (right) events.

the magnitude of $\sqrt{\langle \Delta p_{T,1} \Delta p_{T,2} \rangle}/\langle\langle p_T \rangle\rangle$ in general. PYTHIA 8 and EPOS-LHC describe the data rather well in both jetty and isotropic events.

Chapter 5

Summary and Outlook

In this thesis, the analysis of the data obtained from ultra-relativistic collisions of hadrons and heavy ions using ALICE during the Run-2 phase of the Large Hadron Collider (LHC) at CERN was performed. The analysis focuses on the study of event-by-event mean transverse-momentum fluctuations in proton–proton (pp), xenon-xenon (Xe–Xe), and lead–lead (Pb–Pb) collisions. The centre-of-mass energies used in this analysis were 5.02 TeV for pp and Pb-Pb collisions and 5.44 TeV for Xe-Xe collisions.

ALICE has been specifically designed to explore the dynamics of the early Universe through the study of the state of matter known as Quark Gluon Plasma (QGP), the phase of hot and dense strongly interacting matter produced in heavy-ion collisions at ultra-relativistic energies. Fluctuations of various observables have been extensively studied as they provide important indications about the formation of the Quark-Gluon Plasma (QGP). The collisions between heavy ions, such as Pb, produce a large number of particles, even in a single event. Such large statistics in a single collision could be used to study the fluctuations of different observables like mean transverse momenta, $\langle p_{\mathrm{T}} \rangle$, particle multiplicities, and particle ratios on an event-by-event basis.

The study of temperature and conserved quantum numbers such as baryon number, electric charge, and strangeness are usually performed for various analyses. Fluctuations in the average transverse momentum act as a proxy to the fluctuation in the temperature of the system. The mean transverse momentum fluctuations are also related to dynamical processes in the collisions

like collective behaviour, resonance decays and jets. At LHC energies, the transition to a QGP is anticipated to be a crossover for low values of the baryon chemical potential (μ_B). Consequently, substantial variation in observed fluctuations, due to a phase transition, is not expected.

Nonetheless, $\langle p_{\mathrm{T}} \rangle$ fluctuations serve as a tool to explore the degrees of freedom in the initial state of the collisions. To measure the non-statistical average p_{T} fluctuations, the analysis was focused on the two-particle transverse-momentum correlator. This observable is designed to nullify scenarios exhibiting purely statistical fluctuations. Any non-zero signal detected signifies particle correlations in momentum space, contributing to dynamic average p_{T} fluctuations.

The data analysis in this study was bifurcated into two segments. The initial part of the analysis focused on event-by-event $\langle p_{\mathrm{T}} \rangle$ fluctuations of charged particles produced in Pb–Pb, Xe–Xe, and pp collisions. The second part was specifically dedicated to the examination of pp collisions categorized into various spherocity classes. Both the analyses were carried out for particles falling within a transverse-momentum range of 0.15 GeV/c $< p_{\mathrm{T}} <$ 2 GeV/c. The chosen pseudorapidity acceptance of $|\eta| < 0.8$ is crucial for ensuring a uniform acceptance and efficient detection of tracks within the ALICE Time Projection Chamber, a pivotal system for this investigation.

In the first part of the analysis, the system and energy scan of event-by-event $\langle p_{\mathrm{T}} \rangle$ fluctuations was reported based on the correlator $\sqrt{\Delta p_{\mathrm{T},1} \Delta p_{\mathrm{T},2}}/\langle\langle p_{\mathrm{T}} \rangle\rangle$measured as a function of the charged particle pseudorapidity density. The strength of $\sqrt{\Delta p_{\mathrm{T},1} \Delta p_{\mathrm{T},2}}/\langle\langle p_{\mathrm{T}} \rangle\rangle$ was non-vanishing and exhibited an approximate power law dependence on the produced charged particle density. These new results confirm and corroborate prior observations of non-poissionian fluctuations in AA collisions. In the system size scan, the magnitude of the correlator was observed to decrease by more than one order of magnitude with respect to the produced particle multiplicity density measured in pp, Xe–Xe, and Pb–Pb collisions from low to high multiplicity.

The evolution of the correlator measured in both Pb–Pb and Xe–Xe was found to be in good agreement with the expectations of the power law fit to the HIJING Monte-carlo event generator, in the range $10 < \langle \mathrm{dN_{ch}}/\mathrm{d}\eta \rangle < 50$. However, the data points clearly deviated from this simple trend for $\langle \mathrm{dN_{ch}}/\mathrm{d}\eta \rangle > 50$.

The deviation from the anticipated behaviour, based on the superposition of independent particle-emitting sources in A–A collisions, has been observed through multiple measurements such as the nuclear modification factor [139], anisotropic flow [140], and other two-particle correlation function measurements [141, 142]. Hence, a theoretical model like AMPT, which has shown relative success in describing data from RHIC to LHC energies was used to compare with the data. However, it was noted that both versions of AMPT considered, significantly underestimated the strength of the correlator in most peripheral collisions. While both calculations exhibited an approximate power law dependency on $\langle dN_{ch}/d\eta \rangle$, these trends notably diverge from the observed evolution of $\sqrt{\Delta p_{T,1} \Delta p_{T,2}}/\langle\langle p_T \rangle\rangle$ measured in Pb-Pb and Xe-Xe collisions. Consequently, it can be concluded, that both HIJING and AMPT lack certain crucial characteristics that influence the strength of $\sqrt{\Delta p_{T,1} \Delta p_{T,2}}/\langle\langle p_T \rangle\rangle$ concerning collision centrality.

The energy scan of the two-particle correlator indicated a moderate reliance of $\sqrt{\Delta p_{T,1} \Delta p_{T,2}}/\langle\langle p_T \rangle\rangle$ on the collision energy for central Pb-Pb collisions when comparing energies of 2.76 and 5.02 TeV. For $\langle dN_{ch}/d\eta \rangle < 200$, the two-particle correlator remains consistent within uncertainties. However, for higher values of $\langle dN_{ch}/d\eta \rangle$, the measured correlators at $\sqrt{s_{NN}} = 5.02$ TeV exhibited an increase of roughly 20% than those observed at 2.76 TeV. Nevertheless, the dependence on collision energy vanished when represented as a function of $\langle N_{part} \rangle$. This observation suggested, that for a given initial-state overlap geometry, the strength of the correlator remains independent of collision energy. For $\langle N_{part} \rangle > 25$, the Pb-Pb and Xe-Xe collisions showed similar behavior.

While the observed deviation is likely attributed to radial flow, it's intriguing to explore the possibility of enhanced correlations arising from fluctuations associated with jet production. Specifically, the focus was on investigating event-by-event fluctuation in the number and composition of jets. There is an interest in understanding whether fluctuations in the number or configuration of jets compared to "baseline" regime (those without jets) might amplify fluctuations, potentially altering the correlator's magnitude. Hence, the curiosity to delve into how the correlator's magnitude changes was investigated, based on pp collisions, spanning from jetty to isotropic events. That brought about the second part of the analysis. Events characterized by jets

demonstrated more pronounced mean transverse momentum fluctuations compared to isotropic events. In high-multiplicity collisions, the existence of jets increased the correlator's strength by approximately 20%. This enhancement occurs primarily because particles emitted within a "narrow" cone by jets display a higher average correlation among themselves than other particles. Consequently, the presence of jets substantially increased the correlator's strength within these events. An increase in the correlator strength for the jetty events relative to the spherocity integrated pp collisions suggested that the results seen in A–A collisions are not driven directly by the suppression of jets. Thus the presence of jets in central A–A collisions are not expected to have a significant contribution to the strength of the correlator.

Event-by-event observables can be further characterized as a function of the underlying event activity and, in particular, as a function of the relative transverse activity, R_{T}, which is defined as [133],

$$R_{\mathrm{T}} = \frac{N_{\mathrm{ch}}^{\mathrm{TS}}}{\langle N_{\mathrm{ch}}^{\mathrm{TS}} \rangle}, \tag{5.1}$$

where $N_{\mathrm{ch}}^{\mathrm{TS}}$ is the charged-particle multiplicity in the region transverse to the hard fragmentation region. Events with $R_{\mathrm{T}} \to 0$ are characterized by events with small activity and they are expected to be dominated by jet fragmentation. Events with a low R_{T} can be compared to $e^{+}e^{-}$ collisions, where particle production occurs in the vacuum, and the evolution as a function of R_{T} would allow one to pin down the dependence on the multiple partonic collisions occurring in the more complicated environment of heavy-ion collisions. To ensure that at least one hard scattering took place in the event, selected events are required to have a leading trigger particle above a certain p_{T} value. The event can be classified into three different azimuthal regions, relative to the trigger particle, i.e., Transverse, Away, and Toward regions.

Particle production on the near side is dominated by jet fragmentation and the away-side region mainly consists of the back-scattered jets. Particle production in the Underlying Event (UE) is mostly due to Multiple Parton Interactions, beam remnants, and residual initial and final state radiation. Selecting leading particles with $p_{\mathrm{T}} > 5$ GeV/c ensures that the charged particle density does not increase anymore in the transverse region, this effect is known since the CDF experiment as the "jet-pedestal" effect, as this multiplicity uniformly sits below the

jets detected in the Toward and Away regions. Furthermore, recent analyses performed in ALICE, showed that the transverse region can be further classified into two regions, one with the lowest and the other with the largest particle activity. The transverse region with the lowest multiplicity is the one more directly connected with the number of Multiple Parton Interactions.

Another observable highly correlated to the number of MPIs in pp and p-Pb collisions is the energy carried forward by leading baryons, detected in ALICE using the Zero Degree Calorimeters (ZDC). The energy detected by the ZDC in pp collisions has been measured to be anti-correlated with N_{MPI} and the multiplicity measured at midrapidity. It would be remarkably interesting to investigate event-by-event fluctuations of $\langle p_{\mathrm{T}} \rangle$ measured at midrapidity in various classes of very forward energy obtained in ZDC. Such measurements, performed with a large pseudorapidity gap, would allow the study of observables that are causally disconnected and then the origin of any correlations could be attributed to initial state effects. The outcome of such a study attempted for the first time at LHC energies, would provide new insights into particle production mechanisms.

Appendix

Kinematic variables in heavy-ion collisions

The mathematical framework of special relativity, known as the Lorentz transformations, is crucial for explaining how objects and systems behave when travelling at relativistic speeds, especially in the context of high-energy particle physics. By maintaining their values across all inertial reference frames, invariant variables under Lorentz transformations are independent of the motion of the observer. The comparison of results acquired using different frames of reference is made simpler by this property. It is hence convenient to use the kinematic variables which are invariant or take simple form under the Lorentz transformation from one frame to another frame of reference.

Natural units

Natural units are a set of units used in physics that are based on basic physical constants and are intended to simplify equations and computations, notably in the fields of high-energy particle physics, cosmology, and quantum mechanics. Natural units are sometimes referred to as Planck units or atomic units. In order to remove them from equations and make them dimensionless, natural units set several basic constants, such as the speed of light (c) and Planck's constant (h), equal to 1. When working with extreme energies, when the values of these constants might take on extremely large or extremely tiny values, this simplification is especially helpful. Hence, all physical quantities in high-energy physics are often stated in natural units, *i.e.*, $\hbar = c = k_B = 1$. The conversion $\hbar c = 0.1975$ GeV fm is used to convert all SI units into natural ones. As a result, the dimensions of length and time are given in GeV^{-1}. The fundamental principle

of utilising natural units in this length scale is supported by the strong interaction lifetime of 10^{-23} sec., which is of the order of 1 fermi, and the proton mass being of the order of 1 GeV.

The kinematic variables which are frequently used in heavy-ion collisions are listed below and they are discussed briefly.

Center-of-mass energy

Center-of-mass energy is the square of the sum of four-momentum of the two incoming particles in a two-body collision process. It is Lorentz invariant and it is expressed as:

$$s = (p_1 + p_2)^2 = (E_1 + E_2)^2 - (\vec{p}_1 + \vec{p}_2)^2 = (E_1 + E_2)^2, \tag{5.2}$$

s is the Mandelstam variable. Here, p_1 and p_2 are the four momenta of the colliding particles and E_1, E_2, $\vec{p}_1$ and $\vec{p}_2$ are the energy and momentum of the colliding particles respectively. If the mass of two colliding particles is the same and they are in the centre of the mass frame, $E_1 = E_2$ and $\vec{p}_1 = -\vec{p}_2$. Thus the center-of-mass energy becomes $\sqrt{s} = E_1 + E_2 = 2E$.

Rapidity

Rapidity is a kinematic variable which has the advantage over velocity due to its additive property under a Lorentz boost. It is defined as:

$$y = \frac{1}{2} ln\Big(\frac{E + p_z}{E - p_z}\Big) = \frac{1}{2} ln\Big(\frac{1 + \beta}{1 - \beta}\Big). \tag{5.3}$$

Here p_z is the longitudinal momentum and β is the longitudinal velocity along the z-axis. In the non-relativistic limits, rapidity is equivalent to velocity.

Pseudo-rapidity

In experiments like RHIC and LHC, the mass of the particles cannot be measured directly in an experiment, which makes it impossible to measure energy (E) simultaneously with the momentum (p). Thus, pseudo-rapidity is preferred over rapidity which is given by:

$$\eta = \frac{1}{2} ln\Big(\frac{p + p_z}{p - p_z}\Big) = -ln(tan\theta/2). \tag{5.4}$$

Here, $\theta = tan^{-1}(p/p_z)$ is the angle of a particle emitted to the beam axis. The pseudo-rapidity is a Lorentz invariant quantity. As, it only requires θ, it is convenient to use η in experiments as its use does not warrant particle identification. In relativistic limits, pseudo-rapidity is equivalent to rapidity.

Azimuthal angle

In relativistic heavy-ion collisions, the coordinate system is represented by $(p_{\mathrm{T}}, \eta, \phi)$. The azimuthal angle ($\phi$) is defined as:

$$\phi = tan^{-1}\Big(\frac{p_y}{p_x}\Big). \tag{5.5}$$

This is the angle between the total momentum vector and one of the axis (x-axis) in the transverse (x-y) plane of the particle.

Invariant yield

The invariant yield, a Lorentz invariant quantity, is given by $\frac{Ed^3\sigma}{dp^3}$, where σ, E and p are the cross-section, energy and momentum of the particle, respectively. The invariant yield can be expanded as,

$$\begin{aligned} \frac{Ed^3\sigma}{dp^3} &= \frac{Ed^3\sigma}{p_T dp_T dp_L d\phi} \\ &= \frac{d^3\sigma}{p_T dp_T dy d\phi}, \end{aligned} \tag{5.6}$$

where, $dy = dp_L/E$. In terms of experimentally measurable quantities, invariant yield can be expressed as

$$\begin{aligned} \frac{Ed^3\sigma}{dp^3} &= \frac{1}{m_T}\frac{d^3N}{dm_T d\phi dy} \\ &= \frac{1}{2\pi\, m_T}\frac{d^2N}{dm_T dy} \\ &= \frac{1}{2\pi\, p_T}\frac{d^2N}{dp_T dy}. \end{aligned} \tag{5.7}$$

As, it can be expressed as a function of $p_{\mathrm{T}}(m_{\mathrm{T}})$, the invariant yield is usually called as the $p_{\mathrm{T}}(m_{\mathrm{T}})$-spectra of a particle. This, in addition, encodes various dynamics of particle production,

which include: temperature, radial flow, and the domains of hard and soft physics in particle production. Most of the results in this thesis begin with the p_{T}-spectra.

References

[1] E. Hubble, 1929, "A relation between distance and radial velocity among extra-galactic nebulae," *Proc. Nat. Acad. Sci.* **15**, 168–173.

[2] P. A. R. Ade *et al.* (Planck), 2016, "Planck 2015 results. XIII. Cosmological parameters," *Astron. Astrophys.* **594**, A13.

[3] F. Zwicky, 1933, "Die Rotverschiebung von extragalaktischen Nebeln," *Helv. Phys. Acta* **6**, 110–127.

[4] P. A. R. Ade *et al.* (Planck), 2014, "Planck 2013 results. XVI. Cosmological parameters," *Astron. Astrophys.* **571**, A16.

[5] M. Srednicki, R. Watkins and K. A. Olive, 1988, "Calculations of Relic Densities in the Early Universe," *Nucl. Phys. B* **310**, 693.

[6] G. Bertone, D. Hooper and J. Silk, 2005, "Particle dark matter: Evidence, candidates and constraints," *Phys. Rept.* **405**, 279–390.

[7] J. L. Feng, 2010, "Dark Matter Candidates from Particle Physics and Methods of Detection," *Ann. Rev. Astron. Astrophys.* **48**, 495–545.

[8] , 2008, "LHC Machine," *JINST* **3**, S08001.

[9] S. P. Martin, 1998, "A Supersymmetry primer," *Adv. Ser. Direct. High Energy Phys.* **18**, 1–98.

[10] L. Clavelli and P. Ramond, 1971, "Group Theoretical Construction of Dual Amplitudes," *Phys. Rev. D* **3**, 988.

[11] Y. A. Golfand and E. P. Likhtman, 1971, "Extension of the Algebra of Poincare Group Generators and Violation of p Invariance," *JETP Lett.* **13**, 323–326.

[12] D. J. Griffiths, 2008, *Introduction to elementary particles; 2nd rev. version*, Physics textbook (Wiley, New York, NY).

[13] S. L. Glashow, 1961, "Partial Symmetries of Weak Interactions," *Nucl. Phys.* **22**, 579–588.

[14] A. Salam and J. C. Ward, 1964, "Electromagnetic and weak interactions," *Phys. Lett.* **13**, 168–171.

[15] S. Weinberg, 1967, "A Model of Leptons," *Phys. Rev. Lett.* **19**, 1264–1266.

[16] "The Standard Model — https://home.cern/science/physics/standard-model,"

[17] C.-Y. Wong, 1994, *Introduction to High-Energy Heavy-Ion Collisions* (WORLD SCIENTIFIC).

[18] C. S. F. Z. B. Povh, K. Rith and T. u. K. W. Rodejohann, *Eine Einführung in die physikalischen Konzepte* (Springer (Berlin Heidelberg, Germany), 9th ed., 2014. In German).

[19] D. H. Perkins, 2000, *Introduction to High Energy Physics*, 4th ed. (Cambridge University Press).

[20] H. D. Politzer, 1973, "Reliable Perturbative Results for Strong Interactions?." *Phys. Rev. Lett.* **30**, 1346–1349.

[21] "The Nobel Prize in Physics 2004 — https://www.nobelprize.org/prizes/physics/2004/summary/,"

[22] M. Arslandok, 2017, "Event-by-Event Identified Particle Ratio Fluctuations in Pb–Pb Collisions with ALICE," presented 04 Dec 2017.

[23] C. Ratti, 2018, "Lattice QCD and heavy ion collisions: a review of recent progress," *Rept. Prog. Phys.* **81**, 084301.

[24] Y. Aoki, G. Endrodi, Z. Fodor, S. D. Katz and K. K. Szabo, 2006, "The Order of the quantum chromodynamics transition predicted by the standard model of particle physics," *Nature* **443**, 675–678.

[25] M. A. Stephanov, K. Rajagopal and E. V. Shuryak, 1999, "Event-by-event fluctuations in heavy ion collisions and the QCD critical point," *Phys. Rev. D* **60**, 114028.

[26] M. A. Stephanov, K. Rajagopal and E. V. Shuryak, 1998, "Signatures of the tricritical point in QCD," *Phys. Rev. Lett.* **81**, 4816–4819.

[27] F. Karsch, 2002, "Lattice results on QCD thermodynamics," *Nucl. Phys. A* **698**, 199–208.

[28] R. V. Gavai and S. Gupta, 2005, "The Critical end point of QCD," *Phys. Rev. D* **71**, 114014.

[29] R. Snellings, 2014, "Collective Expansion at the LHC: selected ALICE anisotropic flow measurements," *J. Phys. G* **41**, 124007.

[30] F. Bellini, 2013, "Measurement of K(892)*0 resonance production in Pb-Pb collisions with the ALICE experiment at the LHC,"

[31] M. L. Miller, K. Reygers, S. J. Sanders and P. Steinberg, 2007, "Glauber modeling in high energy nuclear collisions," *Ann. Rev. Nucl. Part. Sci.* **57**, 205–243.

[32] "Evolution of collisions and qgp — https://particlesandfriends.wordpress.com/2016/10/14/evolution-of-collisions-and-qgp/,"

[33] P. Koch, B. Muller and J. Rafelski, 1986, "Strangeness in Relativistic Heavy Ion Collisions," *Phys. Rept.* **142**, 167–262.

[34] B. B. Abelev *et al.* (ALICE), 2014, "Multi-strange baryon production at mid-rapidity in Pb-Pb collisions at $\sqrt{s_{NN}}$ = 2.76 TeV," *Phys. Lett. B* **728**, 216–227.

[35] G. Agakishiev *et al.* (STAR), 2012, "Strangeness Enhancement in Cu+Cu and Au+Au Collisions at $\sqrt{s_{NN}}$ = 200 GeV," *Phys. Rev. Lett.* **108**, 072301.

[36] F. Antinori *et al.* (NA57), 2003, "Hyperon yields in Pb Pb collisions from NA57 experiment," *Nucl. Phys. A* **715**, 140–150.

[37] J. Adam *et al.* (ALICE), 2017, "Enhanced production of multi-strange hadrons in high-multiplicity proton-proton collisions," *Nature Phys.* **13**, 535–539.

[38] S. Voloshin and Y. Zhang, 1996 may, "Flow study in relativistic nuclear collisions by fourier expansion of azimuthal particle distributions," *Zeitschrift for Physik C Particles and Fields* **70**, 665–671.

[39] A. M. Poskanzer and S. A. Voloshin, 1998 Sep, "Methods for analyzing anisotropic flow in relativistic nuclear collisions," *Phys. Rev. C* **58**, 1671–1678.

[40] B. B. Abelev *et al.* (ALICE Collaboration), 2015, "Elliptic flow of identified hadrons in Pb-Pb collisions at $\sqrt{s_{\rm NN}}$ = 2.76 TeV," *JHEP* **06**, 190.

[41] R. Pasechnik and M. Šumbera, 2017, "Phenomenological Review on Quark–Gluon Plasma: Concepts vs. Observations," *Universe* **3**, 7.

[42] S. S. Adler *et al.* (PHENIX), 2003, "Suppressed π^0 production at large transverse momentum in central Au+ Au collisions at $\sqrt{S_{NN}}$ = 200 GeV," *Phys. Rev. Lett.* **91**, 072301.

[43] B. B. Back *et al.* (PHOBOS), 2003, "Centrality dependence of charged hadron transverse momentum spectra in d + Au collisions at S(NN)**1/2 = 200 GeV," *Phys. Rev. Lett.* **91**, 072302.

[44] T. Matsui and H. Satz, 1986, "J/ψ Suppression by Quark-Gluon Plasma Formation," *Phys. Lett. B* **178**, 416–422.

[45] R. Arnaldi *et al.* (NA60), 2007, "J/ psi suppression in In-In collisions at 158-GeV/nucleon," *Nucl. Phys. A* **783**, 261–268.

[46] A. Adare *et al.* (PHENIX), 2007, "J/ψ Production vs Centrality, Transverse Momentum, and Rapidity in Au+Au Collisions at $\sqrt{s_{NN}}$ = 200 GeV," *Phys. Rev. Lett.* **98**, 232301.

[47] A. Adare *et al.* (PHENIX), 2011, "J/ψ suppression at forward rapidity in Au+Au collisions at $\sqrt{s_{NN}}$ = 200 GeV," *Phys. Rev. C* **84**, 054912.

[48] J. Adam *et al.* (ALICE), 2016, "Direct photon production in Pb-Pb collisions at $\sqrt{s_{NN}}$ = 2.76 TeV," *Phys. Lett. B* **754**, 235–248.

[49] E. V. Shuryak, 1978, "Quark-Gluon Plasma and Hadronic Production of Leptons, Photons and Psions," *Phys. Lett. B* **78**, 150.

[50] E. L. Feinberg, 1976, "Direct Production of Photons and Dileptons in Thermodynamical Models of Multiple Hadron Production," *Nuovo Cim. A* **34**, 391.

[51] G. Domokos and J. I. Goldman, 1981, "Quark Matter Diagnostics," *Phys. Rev. D* **23**, 203.

[52] P. Stankus, 2005, "Direct photon production in relativistic heavy-ion collisions," *Ann. Rev. Nucl. Part. Sci.* **55**, 517–554.

[53] O. Linnyk, V. Konchakovski, T. Steinert, W. Cassing and E. L. Bratkovskaya, 2015, "Hadronic and partonic sources of direct photons in relativistic heavy-ion collisions," *Phys. Rev. C* **92**, 054914.

[54] R. Chatterjee, H. Holopainen, T. Renk and K. J. Eskola, 2012, "Collision centrality and τ_0 dependence of the emission of thermal photons from fluctuating initial state in ideal hydrodynamic calculation," *Phys. Rev. C* **85**, 064910.

[55] H. van Hees, M. He and R. Rapp, 2015, "Pseudo-critical enhancement of thermal photons in relativistic heavy-ion collisions?." *Nucl. Phys. A* **933**, 256–271.

[56] J.-F. Paquet, C. Shen, G. S. Denicol, M. Luzum, B. Schenke, S. Jeon and C. Gale, 2016, "Production of photons in relativistic heavy-ion collisions," *Phys. Rev. C* **93**, 044906.

[57] U. W. Heinz, 2004 7, "Concepts of heavy ion physics," in *2nd CERN-CLAF School of High Energy Physics*, pp. 165–238.

[58] C. A. Pruneau, 2017, " Data Analysis Techniques for Physical Scientists,"

[59] S. Jeon and V. Koch, 2004, "Event by event fluctuations," in *Quark-gluon plasma 3*, edited by Hwa, R. C. and Wang, X. N., pp. 430–490.

[60] V. Koch, 2010, "Hadronic Fluctuations and Correlations," in *Relativistic Heavy Ion Physics*, edited by Stock, R., pp. 626–652.

[61] W. Broniowski, B. Hiller, W. Florkowski and P. Bozek, 2006, "Event-by-event p(T) fluctuations and multiparticle clusters in relativistic heavy-ion collisions," *Phys. Lett. B* **635**, 290–294.

[62] P. Bożek and W. Broniowski, 2017, "Transverse momentum fluctuations in ultrarelativistic Pb + Pb and p + Pb collisions with "wounded" quarks," *Phys. Rev. C* **96**, 014904.

[63] S. A. Voloshin, V. Koch and H. G. Ritter, 1999, "Event-by-event fluctuations in collective quantities," *Phys. Rev.* **C60**, 024901.

[64] S. A. Voloshin, 2002 6, "Mean p(t) fluctuations from two particle and four particle correlations,"

[65] S. A. Voloshin, 2006, "Transverse radial expansion in nuclear collisions and two particle correlations," *Phys. Lett. B* **632**, 490–494.

[66] G. Giacalone, F. G. Gardim, J. Noronha-Hostler and J.-Y. Ollitrault, 2021, "Skewness of mean transverse momentum fluctuations in heavy-ion collisions," *Phys. Rev. C* **103**, 024910.

[67] H. Heiselberg, 2001, "Event-by-event physics in relativistic heavy ion collisions," *Phys. Rept.* **351**, 161–194.

[68] P. Braun-Munzinger, K. Redlich and J. Stachel, 2003 4, "Particle production in heavy ion collisions," , 491–599.

[69] H. Appelshäuser *et al.* (NA49), 1999, "Event-by-event fluctuations of average transverse momentum in central Pb + Pb collisions at 158-GeV per nucleon," *Phys. Lett. B* **459**, 679–686.

[70] D. Adamova *et al.* (CERES), 2003, "Event by event fluctuations of the mean transverse momentum in 40, 80 and 158 A GeV / c Pb - Au collisions," *Nucl. Phys. A* **727**, 97–119.

[71] T. Anticic *et al.* (NA49), 2004, "Transverse momentum fluctuations in nuclear collisions at 158-A-GeV," *Phys. Rev. C* **70**, 034902.

[72] D. Adamova *et al.* (CERES), 2008, "Scale-dependence of transverse momentum correlations in Pb-Au collisions at 158A-GeV/c," *Nucl. Phys. A* **811**, 179–196.

[73] T. Anticic *et al.* (NA49), 2009, "Energy dependence of transverse momentum fluctuations in Pb+Pb collisions at the CERN Super Proton Synchrotron (SPS) at 20A to 158A GeV," *Phys. Rev. C* **79**, 044904.

[74] K. Adcox *et al.* (PHENIX), 2002, "Event-by-event fluctuations in mean p(T) and mean e(T) in s(NN)**(1/2) = 130-GeV Au+Au collisions," *Phys. Rev. C* **66**, 024901.

[75] S. S. Adler *et al.* (PHENIX), 2004, "Measurement of nonrandom event by event fluctuations of average transverse momentum in s(NN)**(1/2) = 200-GeV Au+Au and p+p collisions," *Phys. Rev. Lett.* **93**, 092301.

[76] J. Adams *et al.* (STAR), 2005, "Event by event < p(t) > fluctuations in Au - Au collisions at s(NN)**(1/2) = 130-GeV," *Phys. Rev. C* **71**, 064906.

[77] M. Sharma (STAR), 2009, "Estimation of shear viscosity based on transverse momentum correlations," *Nucl. Phys. A* **830**, 813C–816C.

[78] J. Adams *et al.* (STAR), 2006, "Transverse-momentum p(t) correlations on (eta, phi) from mean-p(t) fluctuations in Au-Au collisions at s(NN)**1/2 = 200-GeV," *J. Phys. G* **32**, L37–L48.

[79] J. Adams *et al.* (STAR), 2007, "The Energy dependence of p_t angular correlations inferred from mean-p(t) fluctuation scale dependence in heavy ion collisions at the SPS and RHIC," *J. Phys. G* **34**, 451–466.

[80] J. Adams *et al.* (STAR), 2005, "Incident energy dependence of pt correlations at RHIC," *Phys. Rev. C* **72**, 044902.

[81] E. G. Ferreiro, F. del Moral and C. Pajares, 2004, "Transverse momentum fluctuations and percolation of strings," *Phys. Rev. C* **69**, 034901.

[82] M. Abdel-Aziz and S. Gavin, 2006, "Probing quark gluon liquid using transverse momentum fluctuations," *Nucl. Phys. A* **774**, 623–626.

[83] S. Gavin and G. Moschelli, 2012, "Flow Fluctuations from Early-Time Correlations in Nuclear Collisions," *Phys. Rev. C* **86**, 034902.

[84] B. Alver and G. Roland, 2010, "Collision geometry fluctuations and triangular flow in heavy-ion collisions," *Phys. Rev.* **C81**, 054905.

[85] B. B. Abelev *et al.* (ALICE), 2014, "Event-by-event mean p_{T} fluctuations in pp and Pb-Pb collisions at the LHC," *Eur. Phys. J. C* **74**, 3077.

[86] W.-T. Deng, X.-N. Wang and R. Xu, 2011, "Gluon shadowing and hadron production in heavy-ion collisions at LHC," *Phys. Lett. B* **701**, 133–136.

[87] S. Gavin, 2004, "Traces of thermalization from transverse momentum fluctuations in nuclear collisions," *Phys. Rev. Lett.* **92**, 162301.

[88] J. Adam *et al.* (STAR), 2019, "Collision-energy dependence of p_t correlations in Au + Au collisions at energies available at the BNL Relativistic Heavy Ion Collider," *Phys. Rev. C* **99**, 044918.

[89] B. B. Abelev *et al.* (ALICE), 2014, "Multiplicity Dependence of Pion, Kaon, Proton and Lambda Production in p-Pb Collisions at $\sqrt{s_{NN}}$ = 5.02 TeV," *Phys. Lett. B* **728**, 25–38.

[90] A. Banfi, G. P. Salam and G. Zanderighi, 2010, "Phenomenology of event shapes at hadron colliders," *JHEP* **06**, 038.

[91] B. B. Abelev *et al.* (ALICE), 2013, "Multiplicity dependence of the average transverse momentum in pp, p-Pb, and Pb-Pb collisions at the LHC," *Phys. Lett. B* **727**, 371–380.

[92] "The Large Hadron Collider — home.cern,"

[93] Raghunath Sahoo, 2023, "ALICE Experiment at the CERN Large Hadron Collider,"

[94] CERN-Brochure-2017-002-Eng, 2017, "LHC Guide,"

[95] "A Large Ion Collider Experiment,"

[96] B. B. Abelev *et al.* (ALICE), 2014, "Performance of the ALICE Experiment at the CERN LHC," *Int. J. Mod. Phys. A* **29**, 1430044.

[97] "ALICE Inner Tracking System (ITS),"

[98] G. Dellacasa, L. Ramello, E. Scalas, M. Sitta, N. Ahmad, S. Ahmad, T. Ahmad, W. Bari, M. Irfan, M. S. Zafar, G. Mavromanolakis, A. D. Panagiotou, K. Kalfas, R. Caliandro, D. Cozza, G. De Cataldo, D. Di Bari, D. Elia, R. A. Fini, B. Fini, B. Ghidini, V. Lenti, E. Nappi, F. Navach, F. Posa, F. Corsi, D. De Venuto, R. Dinapoli, A. Grimaldi, G. Lisco, C. Marzocca, E. Monno, X. Li, S. Lu, Z. Lü, S. Ben-Hao, J. Yuan, J. Zhou, S. Zhou, X. Zhu, K. Fanebust, H. Helstrup, A. Klovning, J. A. Lien, O. A. Maeland, O. H. Odland, D. Röhrich, R. Rongved, K. Ullaland, A. S. Vestbø, S. N. Behera, A. K. Dubey, D. P. Mahapatra, B. Mohanty, S. C. Phatak, I. J. Bloodworth, D. Evans, G. T. Jones, P. Jovanovic, J. B. Kinson, A. Kirk, O. Villalobos Baillie, M. F. Vortruba, F. Anselmo, P. Antonioli, G. Bari, M. Basile, L. Bellagamba, D. Boscherini, A. Bruni, G. Bruni, G. Cara Romeo, E. Cerron-Zeballos, F. Cindolo, N. Coppola, M. Corradi, S. De Pasquale, D. Falchieri, A. Gabrielli, E. Gandolfi, P. Giusti, D. Hatzifotiadou, N. Y. Kim, G. Laurenti, M. L. Luvisetto, A. Margotti, M. Masetti, R. Nania, F. Palmonari, A. Pesci, F. Pierella, A. Polini, G. Sartorelli, A. A. Semak, G. Valenti, M. C. S. Williams, A. Zichichi, J. Bracinik, V. Cerny and J. Ftácnik (ALICE), 2000, *ALICE time projection chamber: Technical Design Report*, Technical design report. ALICE (CERN, Geneva).

[99] , 2000, *ALICE Time-Of-Flight system (TOF): Technical Design Report*, Technical design report. ALICE (CERN, Geneva).

[100] A. Andronic (ALICE TRD), 2004, "Electron identification performance with ALICE TRD prototypes," *Nucl. Instrum. Meth. A* **522**, 40–44.

[101] F. Barile, 2014, "Light (hyper-)nuclei production at the lhc measured with alice,"

[102] K. Aamodt *et al.* (ALICE), 2008, "The ALICE experiment at the CERN LHC," *JINST* **3**, S08002.

[103] S. Acharya *et al.* (ALICE), 2023, "Performance of the ALICE Electromagnetic Calorimeter," *JINST* **18**, P08007.

[104] "ALICE Collaboration figure repository,"

[105] P. G. Kuijer, 2009, "Commissioning and Prospects for Early Physics with ALICE," *Nucl. Phys. A* **830**, 81C–88C.

[106] A. Deisting (ALICE), 2018, "Status of the R&D activities for the upgrade of the ALICE TPC," *EPJ Web Conf.* **174**, 01006.

[107] A. Kalweit, 2012, "Production of light flavor hadrons and anti-nuclei at the LHC,"

[108] K. Aamodt *et al.* (ALICE Collaboration), 2008, "The ALICE experiment at the CERN LHC," *JINST* **3**, S08002.

[109] Y. Kharlov, L. Benhabib and R. Wan (ALICE), 2008, "Physics with photons in ALICE," *PoS* **2008LHC**, 089.

[110] A. Fernández *et al.* (ACORDE), 2007, "ACORDE a Cosmic Ray Detector for ALICE," *Nucl. Instrum. Meth. A* **572**, 102–103.

[111] E. V. Shuryak, 1978, "Quark-Gluon Plasma and Hadronic Production of Leptons, Photons and Psions," *Phys. Lett. B* **78**, 150.

[112] E. Abbas *et al.* (ALICE), 2013, "Performance of the ALICE VZERO system," *JINST* **8**, P10016.

[113] M. Gallio, W. Klempt, L. Leistam, J. De Groot and J. Schükraft (ALICE), 1999, *ALICE Zero-Degree Calorimeter (ZDC): Technical Design Report*, Technical design report. ALICE (CERN, Geneva).

[114] B. B. Abelev *et al.* (ALICE), 2014, "Performance of the ALICE Experiment at the CERN LHC," *Int. J. Mod. Phys. A* **29**, 1430044.

[115] B. Abelev *et al.* (ALICE), 2013, "Centrality determination of Pb-Pb collisions at $\sqrt{s_{NN}}$ = 2.76 TeV with ALICE," *Phys. Rev. C* **88**, 044909.

[116] R. Fruhwirth, 1987, "Application of Kalman filtering to track and vertex fitting," *Nucl. Instrum. Meth. A* **262**, 444–450.

[117] F. Ragusa and L. Rolandi, 2007, "Tracking at LHC," *New J. Phys.* **9**, 336.

[118] W. Carena, P. Van de Vyvre, F. Carena, S. Chapeland, V. Chibante Barroso, F. Costa, E. Denes, R. Divia, U. Fuchs, G. Simonetti, C. Soos, A. Telesca and B. von Haller, 2005, "ALICE DAQ and ECS User's Guide," *ALICE-INT-2005-015, CERN-ALICE-INT-2005-015*

[119] R. Brun, P. Buncic, F. Carminati, A. Morsch, F. Rademakers and K. Safarik, 2003, "Computing in ALICE," *Nucl. Instrum. Meth. A* **502**, 339–346.

[120] L. Forthomme, 2022, "CepGen – A generic central exclusive processes event generator for hadron-hadron collisions," *Comput. Phys. Commun.* **271**, 108225.

[121] CERN-Brochure-2017-002-Eng, 2019, "ROOT Data Analyis Framework.."

[122] S. Agostinelli *et al.* (GEANT4), 2003, "GEANT4–a simulation toolkit," *Nucl. Instrum. Meth. A* **506**, 250–303.

[123] R. Brun and F. Rademakers, 1997, "ROOT: An object oriented data analysis framework," *Nucl. Instrum. Meth. A* **389**, 81–86.

[124] CERN Web, 2019, "CERN ROOT Data Analyis Framework,"

[125] P. Cortese, F. Carminati, C. W. Fabjan, L. Riccati and H. de Groot (ALICE), 2005, *ALICE computing: Technical Design Report*, Technical design report. ALICE (CERN, Geneva).

[126] X.-N. Wang and M. Gyulassy, 1991, "HIJING: A Monte Carlo model for multiple jet production in p p, p A and A A collisions," *Phys. Rev. D* **44**, 3501–3516.

[127] CERN Web, 2017, "DPG ALICE,"

[128] S. T. Heckel, 2019, "Mean transverse-momentum fluctuations from soft particles produced in pp, p−Pb and Pb−Pb collisions at the LHC," presented 08 Jul 2019.

[129] CERN Web, 2017, "DPG ALICE,"

[130] github, 2017, "alisw/AliPhysics,"

[131] A. Khuntia, S. Tripathy, A. Bisht and R. Sahoo, 2021, "Event shape engineering and multiplicity dependent study of identified particle production in proton + proton collisions at $\sqrt{s}$ = 13 TeV using PYTHIA8," *J. Phys. G* **48**, 035102.

[132] R. Sahoo, 2020, "Do Proton+Proton Collisions at the LHC Energies Produce Droplets of Quark-Gluon Plasma?." *Springer Proc. Phys.* **248**, 357–364.

[133] S. Tripathy (ALICE), 2021, "Topological studies of light-flavor hadron production in high multiplicity pp collisions with ALICE at the LHC," *PoS* **ICHEP2020**, 512.

[134] R. Brun, F. Bruyant, F. Carminati, S. Giani, M. Maire, A. McPherson, G. Patrick and L. Urban, 1993, *GEANT: Detector Description and Simulation Tool; Oct 1994*, CERN Program Library (CERN, Geneva).

[135] P. Skands, S. Carrazza and J. Rojo, 2014, "Tuning PYTHIA 8.1: the Monash 2013 Tune," *Eur. Phys. J. C* **74**, 3024.

[136] J. Adam *et al.* (ALICE), 2016, "Centrality Dependence of the Charged-Particle Multiplicity Density at Midrapidity in Pb-Pb Collisions at $\sqrt{s_{\rm NN}}$ = 5.02 TeV," *Phys. Rev. Lett.* **116**, 222302.

[137] S. Acharya *et al.* (ALICE), 2021, "Pseudorapidity distributions of charged particles as a function of mid- and forward rapidity multiplicities in pp collisions at $\sqrt{s}$ = 5.02, 7 and 13 TeV," *Eur. Phys. J. C* **81**, 630.

[138] B. Zhang, C. M. Ko, B.-A. Li and Z.-w. Lin, 2000, "A multiphase transport model for nuclear collisions at RHIC," *Phys. Rev. C* **61**, 067901.

[139] S. Acharya *et al.* (ALICE), 2018, "Transverse momentum spectra and nuclear modification factors of charged particles in pp, p-Pb and Pb-Pb collisions at the LHC," *JHEP* **11**, 013.

[140] K. Aamodt *et al.* (ALICE), 2010, "Elliptic flow of charged particles in Pb-Pb collisions at 2.76 TeV," *Phys. Rev. Lett.* **105**, 252302.

[141] J. Adam *et al.* (ALICE), 2017, "Flow dominance and factorization of transverse momentum correlations in Pb-Pb collisions at the LHC," *Phys. Rev. Lett.* **118**, 162302.

[142] S. Acharya *et al.* (ALICE), 2020, "Longitudinal and azimuthal evolution of two-particle transverse momentum correlations in Pb-Pb collisions at $\sqrt{s_{\mathrm{NN}}}$ = 2.76 TeV," *Phys. Lett. B* **804**, 135375.

[143] T. Sjostrand, S. Mrenna and P. Z. Skands, 2006, "PYTHIA 6.4 Physics and Manual," *JHEP* **05**, 026.

[144] T. Pierog, I. Karpenko, J. M. Katzy, E. Yatsenko and K. Werner, 2015, "EPOS LHC: Test of collective hadronization with data measured at the CERN Large Hadron Collider," *Phys. Rev. C* **92**, 034906.

[145] P. Z. Skands, 2010, "Tuning Monte Carlo Generators: The Perugia Tunes," *Phys. Rev. D* **82**, 074018.

Acknowledgements

The completion of my thesis work has been a collaborative effort involving numerous individuals, without whom this accomplishment wouldn't have been possible. Their support and presence throughout this journey have been invaluable to me. While I have endeavoured to acknowledge everyone's contribution during my Ph.D. days, please accept my apologies if I inadvertently missed someone deserving to be on this list.

First and foremost, I extend my deepest gratitude to my parents. My mother, Puspalata Tripathy, embodies patience and expertise, from whom I've imbibed continuously. This Ph.D. journey was her dream too, and her encouragement has been my steadfast motivation. My father, Raghunath Prasad Tripathy, has been a pillar of unwavering support, a constant in my highs and lows, reassuring me with his words, "do not fear when your father is here". I can't thank my fun-loving sister, Bhumika and brother-in-law, Bibhudatta enough; their presence nearby during my years at IIT Bombay made every moment vibrant and unforgettably enjoyable. My nephews, Debansh and Hridish, were my rays of sunshine, keeping me grounded and motivated throughout this scholarly pursuit. I would also like to thank my father-in-law, Dhiren Kumar Tripathy, my mother-in-law Urmila Panigrahi and my sister-in-law, Dr. Shibani Tripathy for creating the safest space to finish my PhD with ease. Their presence was a big support. I express sincere gratitude to my close family members and cousins for contributing to the enrichment of my holidays, which, in turn, enhanced my research capabilities. I owe a debt of gratitude to Padma Shri Kumkum Mohanty, my role model, for illuminating the right path in life and inspiring my endeavours.

My heartfelt thanks go to my Ph.D. supervisor, Prof. Sadhana Dash. Her guidance, from conceptualization to pushing me beyond my limits, has been instrumental. This thesis would not

have been fruitful without her presence. She has not only mentored me professionally but also provided unwavering mental support. She epitomizes the qualities of an exemplary supervisor, fostering the best in her students, allowing them to pursue their free will with utmost respect. Professor Dash embodies the spirit of women's empowerment, and I have learned invaluable lessons from her.

I offer my gratitude to Prof. Basanta Kumar Nandi for his encouragement, support, and invaluable insights into particle physics, which have been a source of immense inspiration. Our discussions enriched my understanding and clarified my thoughts on various topics. I would also like to thank him for being supportive in every endeavour throughout my PhD. I express my deepest appreciation to Prof. Pragya Das and Prof. Archana Pai for their annual evaluations and valuable suggestions.

I am indebted to my close collaborator, Prof. Claude Pruneau, whose brilliant ideas and constant assistance were instrumental throughout my Ph.D. His contribution is an indispensable part of my thesis completion. A special thanks to Prof. Tapan Nayak for his crucial mentorship during the analysis phase. His unwavering help and support in every undertaking are truly priceless.

I feel privileged to take part in one of the experiments (ALICE) at the Large Hadron Collider, the current most powerful and the largest particle accelerator in the world. To be a part of such a gigantic experiment and huge collaboration is undeniably a dream come true. I am thankful to Dr. Marco Van Leeuwen (Spokesperson, ALICE) and Dr. Luciano Musa (former spokesperson, ALICE), Dr. Bedangadas Mohanty (Deputy spokesperson and former ALICE-India spokesperson) and Dr. Zubayer Ahammed (ALICE-India spokesperson) for their support in several matters despite their packed schedules. I would also like to specially thank Dr. Andrea Dainese (former physics coordinator, ALICE) and Dr. Alexander Kalweit (physics coordinator, ALICE) for their thorough review and constructive suggestions for my data analysis work. My heartfelt gratitude extends to Dr. Sumit Basu, Dr. Mesut Arslandok, Dr. Ante Bilandzic, Dr. Katarina Krizkova Gajdosova, Dr. Laura Fabietti, Dr. Iwona Anna Sputowska for their unwavering assistance throughout the analysis, providing essential resources for its completion.

Marian I Ivanov, my service task supervisor, deserves heartfelt thanks for his dedication. His guidance in shell scripting, C++, Python, Jupyter Notebook, and ALICE detector technicalities was pivotal. I am also very thankful to Prof. Raghunath Sahoo, Prof. Subhasish Chattopadhyay, and Prof. Saikat Biswas for being an inspiration to do good work in high-energy physics.

Prof. Surya Narayan Nayak, Nageswara Rao, Prof. Rita Paikaray, Prof. Indira Mishra, and Prof. Rabindranath Mishra, for their crucial guidance and mentorship which has shaped my career in academia. I extend my gratitude to Professor Sudipta Mukherjee for serving as my supervisor during my internship at the Institute of Physics, Bhubaneswar, during my M.Sc. program.

My labmates, Dr. Pragati Sahoo, Dr. Ranjit Kumar Nayak, Dr. Bharati Naik, Dr. Ankita Goswami, Dr. Himani Bhatt, Dr. Baidyanath Sahoo, Dr. Akash Pandey, Dr. Pritam Chakraborty, Subhadeep Roy, Deependra Sharma, Sonali Padhan, Dr. Shubhalaxmi Rath, Tanu, Yash, and Rahul, deserve heartfelt thanks for their encouragement and insightful discussions. Lots of thanks to Monish, Kashi, Pritam again, Sucharita, Urvashi Bothra, Manisha, Supriti, Gopa, Bhawna, Bikash, Bhawna Sahani, Swati Anand, Sanju, Rahul, Subhranshu, Vishnu and Ankit for making this journey worthwhile and enriching it with your presence.

In acknowledgement of my enduring friends, my time-tested allies, Ani, Monica, Sushree, Sidharth, Sandeep, Ghanshyam and my little brother Ankit Kanungoo, I express my sincere gratitude for steadfastly standing by me in every phase of my journey.

I want to express special appreciation to my labmate and closest friend, Dibakar Bauri, and my friend forever, Sagarika Tripathy, for standing by me through my ups and downs. Their friendship has been truly invaluable.

My super special friends from IIT Bombay, Ila Thakur, Swati Singh, and Bhawna Tomar, have made this PhD journey seamless, and their support means the world to me. The endless chatter and pep talks played a crucial role in making the PhD journey less overwhelming for me.

I want to extend my deep gratitude to the entire team at IIT Bombay, especially the physics department, for their invaluable assistance with all my official formalities. I'm also incredibly

grateful for the financial backing from both IIT Bombay and the DST-sponsored ALICE India project. This support was instrumental in enabling me to participate in national and international meetings and conferences, as well as facilitating my visits to CERN for shift work and data collection as part of my research journey.

Lastly, I wish to extend my thanks to my husband, Sushanta Tripathy, for his unwavering love and continual support in all my pursuits. His presence is truly the most precious gift in my life.

In concluding this acknowledgement section, I simply want to express my profound gratitude to the divine for the wonderful people and opportunities that have come my way. I feel truly fortunate and blessed.

Tulika Tripathy

IIT Bombay

7 March 2024